MEASUREMENT OF ANALYTE CONCENTRATIONS AND GRADIENTS NEAR 2D CELL CULTURES AND ANALOGS USING ELECTROCHEMICAL MICROELECTRODE ARRAYS: FAST TRANSIENTS AND PHYSIOLOGICAL APPLICATIONS

A Dissertation

Submitted to the Faculty

of

Purdue University

by

Jose Ferney Rivera Miranda

In Partial Fulfillment of the

Requirements for the Degree

of

Doctor of Philosophy

August 2019

Purdue University

West Lafayette, Indiana

THE PURDUE UNIVERSITY GRADUATE SCHOOL
STATEMENT OF DISSERTATION APPROVAL

Dr. David B. Janes, Chair

School of Electrical and Computer Engineering

Dr. Jenna L. Rickus

School of Agricultural and Biological Engineering

Dr. Muhammad A. Alam

School of Electrical and Computer Engineering

Dr. Arvind Raman

School of Mechanical Engineering

Approved by:

Dr. Dimitrios Peroulis

Head of the School Graduate Program

To my Parents Nancy and Nelson, my Family and Maria Fernanda.

ACKNOWLEDGMENTS

Nothing in this thesis would have been possible without the help, support, and love provided by many people. To all of you I'm indebted: my Parents Nancy and Nelson, my Family, my Life Partner Maria Fernanda; my Friends Yessenia Rivera, Claudia Patricia Renteria, Jorge Eduardo Guerrero, Guillermo Andres Jaramillo, Ana Carolina Murcia, Martin Alonso Mosquera, Laura Marcela Arango, Francy Helena Avila, Justin Richter, Julian Eduardo Castillo, Krishna Singhal, Carlos Hernan Borca, Laura Isabel Giraldo, Arpan Kundu, Sanjay Debnath, Shaimaa Azzam, Rajath Kantharaj, Dr. Ritu Gupta, Dr. Guoping Xiong; Prof. David B. Janes, Prof. Jenna L. Rickus, Prof. Muhammad A. Alam, Prof. Arvind Raman, Prof. Elizabeth J. Tran, Prof. Bradley J. Lucier, Prof. Dennis H. Evans, Prof. Sophie Lelievre, Prof. Bumsoo Han, Prof. Supriyo Datta, Prof. Mark Lundstrom, Prof. Ephraim Fischbach, Prof. Rahim Rahimi, Prof. Ali Shakouri; Colleagues Siddarth V. Sridharan, Dr. Zheng (Cindy) Xing, Doosan Back, Sajia Sadeque, Jiseok Kwon, Asaduzzaman Mohammad, Mayerli Andrea Parra, Dr. Rajtarun Madangopal, Dr. Manuel Ochoa, James K. Nolan, Stephen A. Miloro, Clay Bowes, Leyla Kahyaoglu, Sarah Libring, Hannah Kriscovich; Purdue and Birck Staff Matt Golden, Michelle Wagner, Lacey Siefers, Eduardo Tovar, Nancy Black, Mary Jo Totten, Sheryl Willison, Lorraine Fox, Ira Young, Joon Park, Brenda Meador, Elisheba Van Winkle, Ron Reger, Nithin Raghunathan, Willian Arnett, Michael Bayless, kyle Corwin, Dan Hosler, Stephen Jurss, Tim Kwok, Dave Lubelski, Tim Miller, Bill Rowe, Guy Telesnicki, Kenny Schwartz, Jeremiah Shepard, Jaime Turner, Mark Voorhis, Justin Wirth. I am also very thankful with the funding agencies NSF Nanobiosensing Program Grant #1403582, Colciencias Call #529, and the Colombia-Purdue Institute for Advanced Scientific Research.

TABLE OF CONTENTS

Page

Page

Page

Page

LIST OF TABLES

LIST OF FIGURES

Figure Page

Figure Page

Figure Page

Figure Page

Figure Page

Figure Page

Figure Page

Figure Page

Figure Page

Figure Page

Figure Page

Figure Page

ABSTRACT

Rivera Miranda, Jose Ferney Ph.D., Purdue University, August 2019. Measurement of Analyte Concentrations and Gradients Near 2D Cell Cultures and Analogs Using Electrochemical Microelectrode Arrays: Fast Transients and Physiological Applications. Major Professor: David B. Janes Professor.

This PhD research relates to the design, fabrication, characterization, and optimization of on-chip electrochemical microelectrode arrays (MEAs) for measurement of transient concentrations and gradients, focusing on fast transients and physiological applications. In particular, this work presents the determination of kinetic mechanisms taking place at an active interface (either physiological or non-physiological) in contact with a liquid phase using the MEA device to simultaneously estimate the concentration and gradient of the analyte of interest at the surface of the active interface. The design approach of the MEA device and the corresponding measurement methodology to acquire reliable concentration information is discussed. The ability of the MEA device to measure fast (i.e., in sub-second time scale) transient gradients is demonstrated experimentally using a controllable diffusion-reaction system which mimics the consumption of hydrogen peroxide by a 2D cell culture. The proposed MEA device and measurement methodology meet effectively most of the requirements for physiological applications and as a demonstration of this, two physiological applications are presented. In one application, the MEA device was tailored to measure the hydrogen peroxide uptake rate of human astrocytes and glioblastoma multiforme cells in 2D cell culture as a function of hydrogen peroxide concentration at the cell surface; the results allowed to quantitatively determine the uptake kinetics mechanisms which are well-described by linear and Michaelis-Menten expressions, in agreement with the literature. In the other application, further customization of the MEA device was realized to study the glucose uptake kinetics of human bronchial epithelial and small cell

lung cancer cells, these latter with and without DDX5 gene knockdown; the results allowed to distinguish mechanistic differences in the glucose uptake kinetics among the three cell lines. These results were complemented with measurements of glycolytic and respiration rates to obtain a bigger picture of the glucose metabolism of the three cell lines. Finally, additional applications, both physiological and non-physiological, are proposed for the developed MEA device.

1. INTRODUCTION

1.1 Motivation

Cells exchange molecules with the surrounding medium thus creating and simultaneously being subject to fluctuations in the concentrations of chemical species at the intra- and extracellular levels. These fluctuations in concentration are dictated by the nature of the interactions among species (i.e., the nature of the chemical reactions), the velocity at which the interactions occur (i.e., the kinetics of the reactions), the geometry of the system (i.e., size and shape of the compartments where the reactions occur), the mass transport of the interacting species (i.e., transport by migration, diffusion or convection, and dimensionality thereof), and the spatiotemporal distribution of the species involved in the reactions (i.e., the concentration field and dynamic changes thereof). For any given system of interest, the concentration field is the observable variable. Extraction of timely and relevant kinetic information from the concentration fields being set up by biological systems is an ongoing challenge that, if addressed, will enable the transition from phenomenological descriptions to a solid understanding of the fundamental mechanisms underlying biological processes [1].

One approach to acquire kinetic information from biological systems consists in studying the influx and efflux of the analytes of interest just outside the cell membrane (i.e., in the extracellular space adjacent to the cell surface) using established optical and electrochemical analytical techniques. These two techniques have become the most predominant due to their availability, selectivity, spatial resolution, and temporal resolution, as compared to other techniques that can be more selective (or even specific) but less convenient, e.g., techniques based on radioactive tracers. The basic principle to determine diffusive fluxes given the concentration field of an analyte of interest consists in measuring the concentration at two positions (as a minimum)

within the extent of the concentration field, then calculating the concentration gradient as Δ(concentration)/Δ(position), and finally calculating the product between this concentration gradient and the diffusion coefficient of the analyte of interest. This procedure corresponds to the Fick's Law, which lies at the heart of the work presented in this dissertation and will be invoked many times.

Electrochemical techniques such as scanning electrochemical microscopy (SECM) [2–6] and vibrating probe self-referencing technique (SRT) [7–13] have demonstrated the ability to respond to transient changes in the local concentration regardless of the reversibility or irreversibility of the electrode reactions. In contrast, many optical probes used in biological applications are irreversible and therefore measure cumulative bulk effects rather than real-time changes in local concentration. For this reason, the electrochemical techniques have gained great popularity, particularly in applications requiring high temporal resolution for monitoring fast transient changes in concentration. SECM and SRT techniques have proven effective at mapping the concentration profile perpendicular and in close proximity to biointerfaces in a variety of geometrical configurations, including isolated single cells and 2D/3D cell cultures [9, 12, 14], which is advantageous for the purpose of determining the fluxes going into or coming out of cells. However, mapping a concentration profile with a single probe requires moving the probe tip throughout multiple points within the extent of the concentration field, thus establishing a trade-off between spatial and temporal resolution. Adhered to this limitation, SRT maximizes the temporal resolution by moving periodically the probe tip only between two positions such that the concentration gradient at a given spot can be determined. This strategy has proven effective to measure a variety of biophysical fluxes (i.e., gradients) exhibiting transient changes occurring over more than 2 seconds, since the probe tip is vibrated at a maximum frequency of 0.2–0.5 Hz (in amperometric measurements) to avoid perturbation of the gradient of interest by induced stirring.

The question remains as to how to measure transient changes in concentration gradient occurring in the sub-second scale, e.g., the time scale of neuronal commu-

nication is in the order of less than 10 ms [15] [16]. In general, SECM and SRT are still limited by the overall measurement time required to obtain multi-point concentration measurements over the relevant spatial scales without perturbing the medium around the probe tip [2,9–14,17,18] and therefore, the goal of this thesis is to present the experimental development of an electrochemical device and a method to measure transient changes in concentration gradient caused by 2D biointerfaces and occurring in the sub-second scale, specifically in the order of 150 ms.

1.2 Fast transient gradients in biological systems

Neurotransmission is cited here as a biological model of fast transient gradients generated by molecular release and uptake processes [15, 16, 19]. Typically, vesicles with diameter of ∼150 nm contain a small number of neurotransmitter molecules (∼230,000) and are initially located inside a neuron. When the neuron receives suitable electrical stimuli, the vesicles fuse with the cell membrane and release their contents into the extracellular space. The released neurotransmitter molecules propagate by diffusion toward receptors located at other neurons which, in turn, trigger other signaling events.

1.3 Relevant scales of fast transient gradients in biological problems

Considering the problem of neurotransmission, if the vesicle is assumed to be a sphere with diameter of ∼150 nm, then ∼230,000 molecules inside the vesicle would correspond to a concentration of ∼200 mM. This concentration is relatively high compared to, for instance, the normal concentration of glucose in blood (4-8 mM) [20]. However, once these molecules are released into the extracellular space, diffusion drives their spatial distribution over time resulting in fast changes in local concentration. Depending on the distance from the release point, the changes in local concentration are 4-7 orders of magnitude smaller than the concentration inside the vesicle. For a single vesicle release, concentrations in the order of μM can be expected within

distances of 1 μm from the release location and during time periods less than 10 ms. However, neurotransmission processes may also involve release from multiple vesicles from a single cell, thus increasing the expected range of concentrations to tens of μM within distances of tens of μm from the release location and during time periods of $\sim$100 ms [15].

In typical in-vitro experiments clusters of neurons are stimulated by adding small drops of highly-concentrated K^+ solution [13]. In this case, multiple neurons are stimulated collectively, and therefore the transient gradients exhibit temporal and spatial scales in excess of 0.5 s and 100 μm, respectively. The release/uptake of neurotransmitters is not exclusive to neurons. Other cells like astrocytes also participate in release/uptake processes but the temporal scale of the generated transient gradients are typically in the range of tens of seconds [21]. Slower but still intriguing and interesting transient gradients have also been observed. For example, oscillatory glucose uptake with periodicity of $\sim$3 min was observed for pancreatic beta cells [11]; this periodic glucose uptake is thought to be involved in a metabolic control loop.

1.4 Requirements for measurement of fast transient gradients

The requirements can be split into two parts: the requirements for each individual sensor and the requirements for the set of sensors comprising the array. In the specific case of this thesis the sensors are microelectrodes which for simplicity will be referred to as electrodes, simply. Therefore, regarding the individual electrodes, the sensitivity should be enough as to operate in the concentration scales of biological systems (typically a small scale) and yet distinguish the signals from any pair of closely spaced electrodes, despite the signal noise; the selectivity should be conferred by any physical or chemical system capable of providing selective and transducible interactions with the analyte of interest; the dynamic response time should be several times shorter than the time scale of the faster transient of interest; the sensitivity should be stable

for the duration of the experiment of interest; and last but not least, the electrodes should measure local concentrations rather than average bulk concentrations.

Regarding the set of electrodes that constitute the MEA, the requirements are more of geometrical nature. If the electrodes in the MEA provide reliable measurements of local concentrations, then the key to measure a transient gradient is to simultaneously acquire concentration information at various spatial points within the spatial scale of the gradient and with sufficient sampling time. The reason for this is because the size, surface concentration and kinetics of the source (or sink) dictate the spatial and temporal scales of the gradients of interest, and therefore sensor parameters like electrode size, inter-electrode separation, and electrode kinetics must be tuned accordingly on a per case basis. In general, the inter-electrode separation must be $\sim 5\times$ the electrode size to obtain well defined measurements of local concentrations; the electrode size must be at least $10\times$ smaller than the size of the source (or sink) to avoid perturbation of the gradient of interest; and the kinetics of the sensors must be orders of magnitude faster than the kinetics of the source (or sink) to capture fast changes in local concentration. If a source generates the gradient of interest, then the surface concentration at the source must be larger than the limit of detection of the sensors. Otherwise, if a sink generates the gradient of interest, the background concentration must be larger than the limit of detection of the sensors.

1.5 Sensors for measurement of fast transient gradients

Optical and electrochemical arrays are two approaches that have the potential to measure fast transient concentrations and gradients with the appropriate spatial and temporal resolution for studies of cellular communication [15]. In both cases, the size of individual sensors in the array must be in sub-micrometer scale if the goal is to measure fast transient gradients caused by release from multiple vesicles around a single cell. Optical arrays based on functionalized carbon nanotubes have been demonstrated exhibiting spatial resolution of $\sim$20,000 sensors per cell, thus satisfying

by far the sensor size requirement, and temporal resolution of 100 ms [16]. Here it is important to note that the temporal resolution is greatly determined by the response time of the sensors, which is in turn determined by the binding/unbinding kinetics between the analyte and the sensors. In contrast, electrochemical arrays operated in amperometric mode offer much better temporal resolution (in microsecond range) which is in practice determined by filtering, signal-to-noise ratio and sampling rate rather than by the response time of the sensors [22, 23]. To date, electrochemical arrays provide spatial resolutions in the order of micrometers, and the design and fabrication of individually addressable nanoelectrode arrays is expected to be routine in the future [15].

1.6 Objectives of the thesis

This PhD research is part of a larger project whose goal is to create a platform technology for the simultaneous spatiotemporal measurement of multiple biomolecule gradients in basic in-vitro studies. Therefore, the objectives below define the contribution of the work presented here to the achievement of the grand goal.

1.6.1 General objective

To create and demonstrate an electrochemical microelectrode array (MEA) device to quantitatively measure fast transient changes in concentrations and gradients near physiological and non-physiological active interfaces.

1.6.2 Specific objectives

1. To define the technical specifications of an MEA device to measure fast transient changes in concentrations and gradients.

2. To design, fabricate, characterize and optimize an MEA device to measure fast transient changes in concentrations and gradients.

3. To demonstrate the applicability of the developed MEA device in physiological studies.

2. PRINCIPLE, DESIGN AND FABRICATION OF ELECTROCHEMICAL MEAs

This chapter is devoted to the discussion of the operating principle of amperometric sensors, both isolated and within an MEA, the guidelines to design MEAs for measurement of transient gradients, and the fabrication of the MEAs.

2.1 Working principle of amperometric sensors: brief overview

The following is just a brief overview of the operating principle of amperometric sensors, based on the electrochemistry textbook by Bard and Faulkner [24]. The goal of this section is to provide the mechanistic base that relates current, applied potential, and concentration of the involved species, both at the surface of the electrode and at the bulk of the solution. For a thorough account of the theoretical fundamentals of amperometric and other sensors, the reader is referred to the original sources such as Bard and Faulkner [24] and Zoski [25], among others.

In simple words, amperometric sensors are electrodes which are biased at constant voltage in order to drive electrical currents which are proportional to the concentration of the chemical species reacting at the electrode surface; therefore, the analytical signal is an electrical current and the transduction principle is of electrochemical nature.

In more detail, amperometric sensors are embodiments of the specific type of electrochemical technique called chronoamperometry in which a constant electrical potential is applied to a system (called electrochemical cell) typically composed of three electrodes (called working, auxiliary and reference electrodes), which are immersed in a solution, in order to drive the flow of an electrical current through the solution connecting the auxiliary and working electrodes and then through an ex-

ternal circuit which connects back to the electrochemical cell, thus closing the loop. The external circuit is typically a potentiostat whose main functions are to keep the applied potential (i.e., between working and reference) constant and to measure the current originated from the electrochemical reactions occurring at the surface of the working electrode. Electrochemical reactions are those where charge transfer occur across the interface between chemical phases, typically between electronic and ionic conductors, and can be classified according to the direction of the charge transfer into oxidation and reduction reactions. Oxidation is when the species/phase of interest give electrons to other species/phase, whereas reduction is the opposite, i.e., when the species/phase of interest receives electrons from other species/phase. Since these reactions go in opposite directions, the measured current is the difference between the forward and backward directions of the charge transfer, as indicated by (2.1)

$$i = nFA\left[k_f C_O(0,t) - k_b C_R(0,t)\right] \tag{2.1}$$

$$i_f = nFAk_f C_O(0,t) \tag{2.2}$$

$$i_b = nFAk_b C_R(0,t) \tag{2.3}$$

where the forward and backward directions of charge transfer are given by (2.2) and (2.3), respectively. In these expressions n is the number of electrons being transferred during the reaction, F is the Faraday constant, A is the electrode surface area, k_f is the forward reaction constant, k_b is the backward reaction constant, $C_O(0,t)$ is the concentration of oxidized species at the electrode surface (i.e., at $x = 0$), and $C_R(0,t)$ is the concentration of reduced species at the electrode surface. The measured current is therefore a function of time if $C_O(0,t)$ and/or $C_R(0,t)$ are functions of time, which is the situation more often than not. According the Butler-Volmer formalism, which describes well the majority of electrochemical systems, k_f and k_b are thermodynamically related to the electrode potential, E, as given by (2.4) and

(2.5). It is very important to note that E is the potential developed spontaneously at the interface between the two chemical phases with respect to the potential of the reference electrode, which by definition is constant regardless of any processes occurring in the electrochemical cell. Since thermodynamic laws must be satisfied, the potential E always experiences a transient change toward the equilibrium value when the electrochemical cell is assembled for the first time or after a perturbation.

$$k_f = k^0 e^{-\alpha f\left(E-E^{0'}\right)} \tag{2.4}$$

$$k_b = k^0 e^{(1-\alpha) f\left(E-E^{0'}\right)} \tag{2.5}$$

where k^0 is the standard reaction rate constant (an intrinsic property of the interface between the two chemical phases), α is a constant parameter describing the symmetry of the thermodynamic reaction coordinate, $f = F/RT$, R is the molar gas constant, T is the temperature, and $E^{0'}$ is the formal potential (also an intrinsic property of the interface between the two chemical phases). $E^{0'}$ is defined as the equilibrium potential of the electrode of interest (i.e., the working electrode) when $C_O(0,t) = C_R(0,t)$. When $C_O(0,t) \neq C_R(0,t)$, the equilibrium potential of the working electrode, E_{eq}, is given by the Nernst equation (2.6)

$$E_{eq} = E^{0'} + \frac{RT}{F} \ln \frac{C_O(0,t)}{C_R(0,t)} = E^{0'} + \frac{RT}{F} \ln \frac{C_O^*}{C_R^*} \tag{2.6}$$

where C_O^* and C_R^* are the concentrations of oxidized and reduced species at the bulk of the solution. The equalities $C_O(0,t) = C_O^*$ and $C_R(0,t) = C_R^*$ are justified by the condition of equilibrium, meaning that the net current crossing the electrode surface is zero and therefore the concentration of oxidized and reduced species at the electrode surface must be the same as the respective concentrations at the bulk solution. At the equilibrium condition the forward current must be balanced by backward current, i.e., $i_f = i_b$, and the magnitude of either of these currents at equilibrium is called the exchange current, i_0, as given by (2.7)

$$i_0 \equiv |i_f| \text{ or } |i_b| \quad \text{at equilibrium condition} \tag{2.7}$$

Using (2.2), (2.3) and (2.6) and after some algebraic rearrangement, the exchange current i_0 can be expressed as given by (2.8). The exchange current is an intrinsic property of the interface originated between the two chemical phases.

$$i_0 = FAk^0 {C_O^*}^{(1-\alpha)} {C_R^*}^{\alpha} \tag{2.8}$$

Now, all the elements are in place to obtain an expression to describe the net current as a function of the applied potential, E_{appl}. Using (2.1), (2.4) and (2.5), the net current can be written as

$$i = nFAk^0 \left[C_O(0,t) e^{-\alpha f\left(E-E^{0'}\right)} - C_R(0,t) e^{(1-\alpha) f\left(E-E^{0'}\right)} \right] \tag{2.9}$$

Dividing (2.9) by (2.8), the expression (2.10) is obtained

$$\frac{i}{i_0} = \frac{C_O(0,t)}{C_O^*} e^{-\alpha f\left(E-E^{0'}\right)} \left(\frac{C_O^*}{C_R^*}\right)^{\alpha} - \frac{C_R(0,t)}{C_R^*} e^{(1-\alpha) f\left(E-E^{0'}\right)} \left(\frac{C_O^*}{C_R^*}\right)^{-(1-\alpha)} \tag{2.10}$$

Raising the Nernst equation (Eq. 2.6) to the $-\alpha$ and $-(1-\alpha)$ powers, then inserting those results into (2.10), and then renaming the potential E as E_{int} yields the expression (2.11), which describes the net current as a function of the potential of interest E_{int}.

$$i = i_0 \left[\frac{C_O(0,t)}{C_O^*} e^{-\alpha f(E_{int}-E_{eq})} - \frac{C_R(0,t)}{C_R^*} e^{(1-\alpha) f(E_{int}-E_{eq})} \right] \tag{2.11}$$

Remind that E_{eq} develops spontaneously after assembling the cell, hence the purpose of E_{appl} is to shift the electrode potential from its equilibrium value to the value of interest, as given by (2.12)

$$E_{int} = E_{eq} + E_{appl} \tag{2.12}$$

Therefore, inserting (2.12) into (2.11) yields the desired expression describing the net current as a function of E_{appl}.

$$i = i_0 \left[\frac{C_O(0,t)}{C_O^*} e^{-\alpha f\left(E_{appl}\right)} - \frac{C_R(0,t)}{C_R^*} e^{(1-\alpha) f\left(E_{appl}\right)} \right] \tag{2.13}$$

2.1.1 The specific case of H_2O_2 at platinum electrode in phosphate buffer saline solution

As mentioned before, the electrode potential (i.e., E_{int}) in amperometric sensors is kept constant using a potentiostatic circuit. As an example, consider the electrooxidation reaction of H_2O_2 (Eq. 2.14) at a platinum surface which is kept at a potential of interest $E_{int} > E_{eq}$ and immersed in phosphate buffer saline (PBS) at pH 7.4 (physiological pH). Fig. 2.1 shows this situation schematically. In this reaction the reduced species is H_2O_2 and the oxidized species is O_2. Note that the arrow in (2.14) goes in one direction only, meaning that the reaction is more prone to spontaneously occur from H_2O_2 to O_2 rather than in the opposite direction, i.e., the reaction is irreversible [26, 27]. Due to this irreversibility and other spontaneous processes that are intrinsic to the system H_2O_2/Pt/PBS (pH 7.4) [28], the Pt electrode exhibits an ill-defined E_{eq} which changes slowly over time within the range of 150–250 mV, according to experimental observations by the author. Therefore, if the potentiostat is set to keep E_{int} at a constant value of 500 mV, then the potentiostat applies E_{appl} in the range of 350–250 mV. This example is of great relevance since almost all the signals in this work are due to the electrooxidation of H_2O_2 at platinum.

$$\mathrm{H_2O_2} \xrightarrow{\mathrm{Pt}} \mathrm{O_2} + 2\,\mathrm{H^+} + 2\,\mathrm{e^-} \tag{2.14}$$

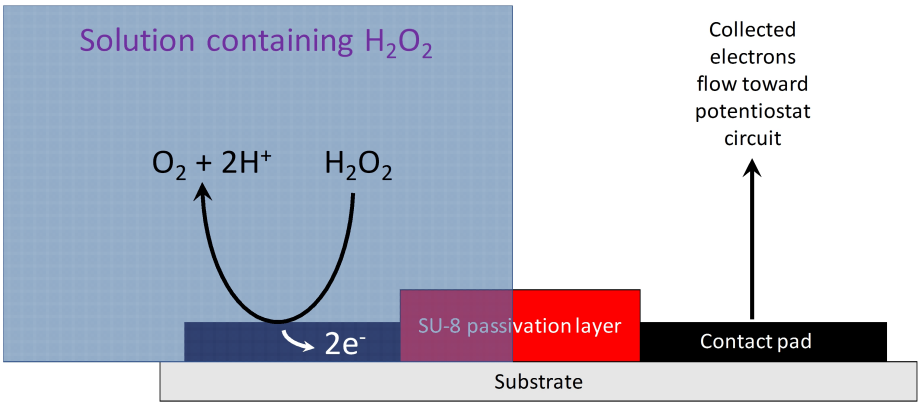

Fig. 2.1. Schematic diagram of a platinum film (black) covered by an insulating layer of SU-8 photoresist (red) on top of a substrate (gray). This device is partially immersed in a solution (blue) containing H_2O_2. The part of the platinum film immersed in the solution corresponds to the working electrode whereas the other part is connected to a potentiostat (not shown). When a potential is applied between the working electrode and the reference electrode (not shown), the oxidation reaction $H_2O_2 \longrightarrow O_2 + 2\,H^+ + 2\,e^-$ takes place at the surface of the working electrode. The byproducts of this reaction, namely O_2 and $2\,H^+$, diffuse away toward the bulk solution and the $2\,e^-$ flow toward the contact pad where are then collected by the potentiostat. The kinetics of this reaction depends on how far E_{int} is set relative to E_{eq}.

2.2 Design considerations for MEAs

2.2.1 Architecture of the sensor: electrode material and functionalization

Since the long term goal of this thesis is to develop devices for the measurement of transient concentration gradients of metabolites like glucose and lactate, the sensor architecture must provide selectivity to the analyte of interest. Oxidase enzymes such as glucose oxidase, lactate oxidase, and glutamate oxidase are commonly used to provide selectivity to glucose, lactate, and glutamate, respectively. The selectivity originates from the chemistry of the reaction between the enzyme and its substrate. The reaction between glucose oxidase (GOx) and glucose is given in (2.15)

$$\text{glucose} + O_2 \xrightarrow{\text{GOx}} \text{gluconolactone} + H_2O_2 \tag{2.15}$$

The principle to selectively measure concentrations of glucose consists in quantifying the H_2O_2 that results from the reaction (2.15). Since H_2O_2 is an electroactive molecule, meaning that it is easily oxidized or reduced at a metal surface, the quantification of H_2O_2 proceeds electrochemically via the reaction (2.14). Therefore, the problem reduces to the sensitive and reliable measurement of H_2O_2. In this regard, the electrode material must be a catalyst for the oxidation of H_2O_2, biocompatible, amenable to microfabrication, and resistant to biofouling (if possible).

Platinum has been used over decades as the gold standard for the construction of enzyme-based amperometric sensors due to its electrocatalytic properties to oxidize H_2O_2 [28], biocompatibility [23], and compatibility with microfabrication technology. Due to the high catalytic rate for H_2O_2 oxidation, platinum yields high sensitivity compared to other materials, e.g., carbon electrodes. Furthermore, the sensitivity of polycristalline Pt can be easily increased by an order of magnitude by deposition of platinum black (PtB), which was the strategy adopted in this work. However, the high sensitivity is at the expense of a relatively long time for stabilization of the signal and poor repeatability of the measurements [26,27], as compared to carbon electrodes. Regarding the possibility of biofouling, platinum is much more prone to biofouling in comparison to carbon electrodes [23]. All these issues arise from the intrinsic properties of the interface between the chemical phases of platinum and H_2O_2/PBS, which are discussed in detail in the literature [26–32]. Despite these inconveniences, platinum was selected to be the electrode material because the measurement of transient concentration gradients in small concentration scales, typical of physiological applications, requires high sensitivity in order to distinguish the readouts from closely spaced electrodes.

To render the electrodes selective to glucose, the conventional strategy based on immobilization of glucose oxidase (GOx) on the electrode using a polymeric matrix was employed. This strategy is very robust as has been used over decades for aca-

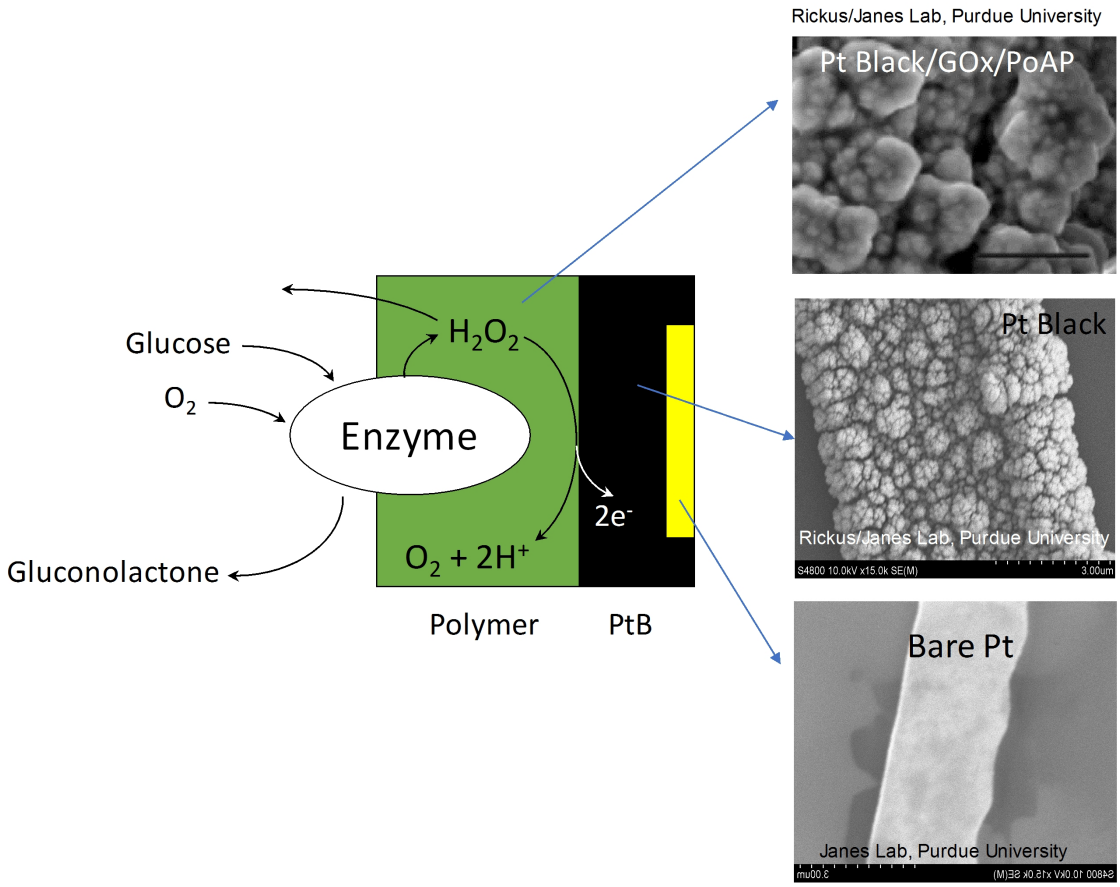

Fig. 2.2. Schematic diagram illustrating the sensor architecture. Evaporated platinum (yellow) defines the footprint surface area of the electrode. Platinum black (PtB) (black) is deposited on the platinum surface to increase the sensitivity to H_2O_2 by an order of magnitude. The enzyme glucose oxidase (GOx) is embedded in a polymer matrix (green) which is deposited on the PtB surface. SEM images on the right show how the smooth surface of the evaporated Pt is then transformed into a very rough surface which is ultimately covered by the polymer matrix encapsulating the GOx. SEM images were acquired in collaboration between Rickus's and Janes' Research Groups.

demic, industrial and commercial purposes. The specific details of the GOx functionalization are described in Section 5.2. Figure 2.2 illustrates the sensor architecture.

2.2.2 Architecture of the microelectrode array: 1D versus 2D

The literature indicates that majority of the research on MEAs has been devoted to high density 2D MEAs [33–49]. The goal has been for a long time to deploy as many electrodes as possible in a small 2D area (some MEAs have even more than 2048 electrodes) and integrate the MEA with on-chip potentiostat circuitry to measure either potentiometric or amperometric signals. These 2D MEAs have been used for 2D imaging of ex-vivo tissue, spatial tracking of action potential waves from nervous cells, and multi-point detection of cellular exocytotic release, but very few attempts (if any) have been made to reliably measure transient concentration gradients in biological settings. In fact, many reports show just raw current data, in the form of heat maps, or rise times rather than absolute concentration values from which the gradient can be inferred.

Since the objective of this thesis is to obtain experimental evidence on the reliable measurement of transient concentration gradients, it is therefore reasonable to question whether there is any advantage in having too many electrodes arranged in 2D compared to having just a few electrodes arranged in 1D. The answer to this question turned out to be that 1D MEAs are better than 2D MEAs when operated amperometrically with the purpose of measuring concentration gradients reliably. This answer is supported by a series of finite element simulations performed in Comsol Multiphysics software.

Simulation of a transient gradient induced by a large sink electrode

The first step is to simulate the dynamics of the concentration field induced by an arbitrary gradient generator. Since the goal is to compare the simulations against experiments, a large platinum electrode was chosen to act as the gradient generator, and therefore the gradient is generated due to analyte consumption by an electrochemical reaction occurring at the electrode surface, as described by Eq. (2.1). The gradient generator has a diameter of 1.6 mm and will be referred to as the large sink

electrode (LSE), in order to distinguish it from the sensing electrodes. A photograph of the LSE, the details of the simulation domain and the boundary conditions are shown in Fig. 2.3.

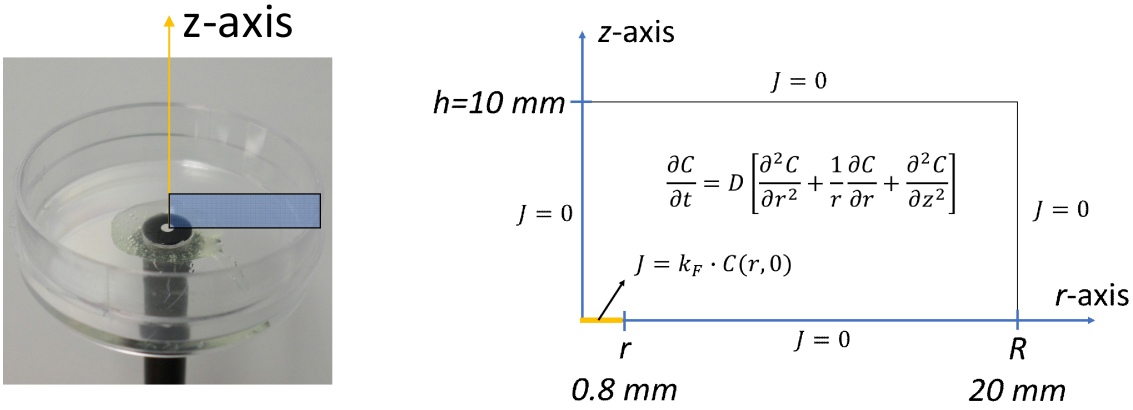

Fig. 2.3. Photograph of the large sink electrode (LSE), and schematic diagram illustrating the simulation domain and boundary conditions. The photograph shows a large platinum electrode (1.6 mm diameter) inserted at the bottom of a Petri dish such that the electrode plane and the bottom plane of the Petri dish are aligned. The blue rectangle highlighted in the photograph correspond to the axis-symmetric simulation domain whose details and boundary conditions are specified in the schematic diagram, where C is the concentration, D is the diffusion coefficient of the analyte, and k_f is the heterogeneous reaction rate constant of the reaction at the LSE surface. The simulation domain is therefore defined by the geometry of the Petri dish, which is described in cylindrical coordinates as the volume enclosed by $0 < r < 20$ mm and $0 < z < 10$ mm . The LSE surface is the area enclosed by $0 < r < 0.8$ mm at $z = 0$. The reaction at the LSE surface is described as a surface flux $J = k_f \cdot C(r, 0)$. All remaining boundary segments have zero-flux conditions, i.e., $J = 0$. The initial uniform concentration, C_0 is set to 20 μM, k_f is set to 10^{-3} m s^{-1} and D is set to 1.71×10^{-9} m^2 s^{-1} (corresponding to the diffusion coefficient of H_2O_2). The current is described only in terms of k_f since the electrooxidation of H_2O_2 is irreversible, meaning that $k_b \sim 0$.

Given that in the practice the sensing electrodes require at least 300 seconds to condition the amperometric signal before a reliable measurement can be done, the simulation is run from 0 to 300 s with the LSE having $k_f = 0$ such that nothing occurs to the concentration field. At $t = 300$ s the k_f is set to 10^{-3} m s^{-1} and the simulation is run until 600 s. Snapshots of the simulated concentration field along the z axis at various time points are shown in Fig. 2.4. Fig. 2.4 shows that the concentration at the LSE surface decreases from 20 to 2.5 μM during the first second of the reaction, thus indicating that a fast transient change in concentration would be experienced by a sensing device, if positioned very close to the LSE surface. Also, during the first second of the reaction the extent of the depletion region reaches 200 μm (the depletion region is the region adjacent to the LSE wherein the concentration is different from the bulk concentration). The reaction continues consuming analyte until $t = 600$ s, time at which the extent of the depletion region has grown more than 800 μm and the analyte concentration at the LSE surface is less than 0.5 μM.

The results presented in Fig. 2.4 clearly illustrates the trade-off between space and time that must be faced during the measurement of fast transient gradients (i.e., transients occurring in sub-second time scales). To track the evolution of the transient during the first second of the reaction, several local concentrations must be measured simultaneously within 200 μm from the LSE and with a sampling period $<<$ 1 second. The fact that the spatial scale of interest is only 200 μm from the LSE has obvious implications on the electrode size and inter-electrode separation: the larger the electrodes, the less electrodes can be deployed within 200 μm, and therefore the lower the spatial resolution of the gradient measurement. In contrast, if there is no necessity to track the evolution of the transient gradient during the first 20 s of the reaction, then it is sufficient to simultaneously measure several local concentrations within 600 μm from the LSE and with a sampling period $>$ 1 second. The situations mentioned above are concerned only with the measurement of the transient gradients regardless of how they are originated. The challenge is even larger if the purpose of measuring the transient gradient is to gain mechanistic knowledge

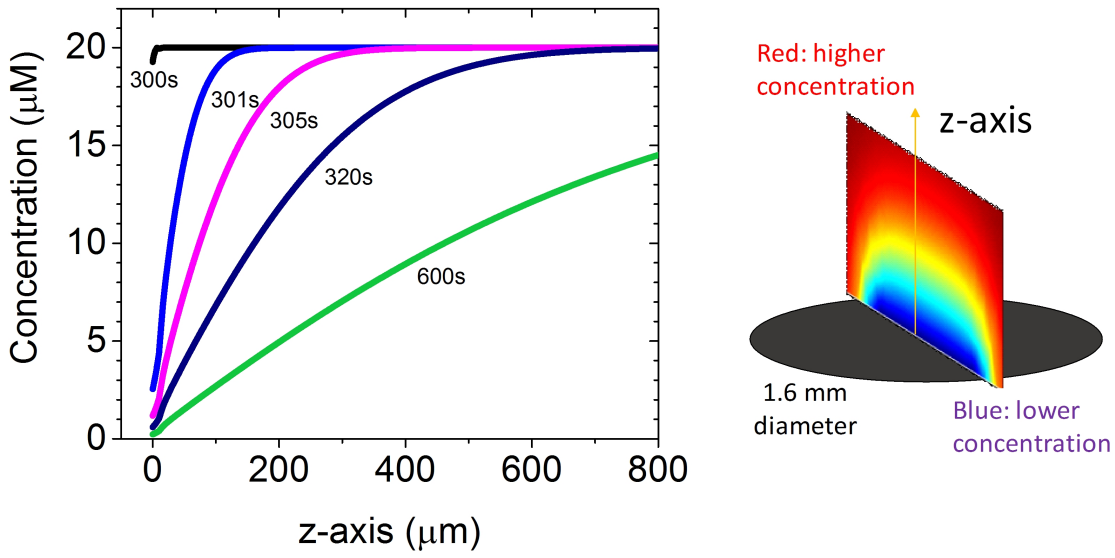

Fig. 2.4. The simulated concentration field, plotted along the z axis at various time points, for the large sink electrode (LSE) consuming analyte at a rate given by $k_f = 10^{-3}$ m s^{-1}. The simulated analyte is H_2O_2 ($D = 1.71 \times 10^{-9}$ m^2 s^{-1}). The schematic on the right illustrates the concentration field along a plane cut aligned with the z axis and perpendicular to the LSE plane.

about the kinetics of the process originating the gradient. In that case it is obvious that the gradient should be tracked from the very beginning and with higher temporal and spatial resolutions.

Simulation of the measurement of transient concentrations

The simulation above provides guidelines on how to deploy electrodes near the LSE (i.e., the gradient generator) in order to capture the transients in concentration that ultimately enable the determination of the transient concentration gradient. The quality of the gradient measurement thus relies on the accuracy of the measurements of transient concentrations. Assuming that sensing electrodes are positioned within

800 μm from the LSE, the questions is: do the sensing electrodes measure the transient concentrations reliably?

To answer this question, the simulation considered two cases which are depicted in Fig. 2.5. Case 1 is a single sensing electrode and Case 2 is a 2D array of sensing electrodes (i.e., a 2D MEA). In both cases the sensing electrodes are squares of 10 μm $\times$ 10 μm lying on a silicon substrate. The parameters of the simulations were carried over from the simulation of the gradient generated by the LSE. These parameters are initial bulk concentration, $C_0 = 20$ μM, diffusion coefficient of the analyte, $D = 1.71 \times 10^{-9}$ m^2 s^{-1}, and reaction rate of the LSE, $k_f = 10^{-3}$ m s^{-1}. The reaction rates at the surface of the sensing electrodes were set to $k_f = 10^{-5}$ or 10^{-3} m s^{-1} depending on whether the sensing electrodes are bare Pt or bare Pt modified with Pt black, respectively.

The simulation was run from 0 to 600 s, time during which the k_f of the sensing electrodes was set to a value, either 10^{-5} or 10^{-3} m s^{-1}. The k_f of the LSE was set to zero from 0 to 300 s, such that the only perturbation to the concentration field was the one caused by the sensing electrodes, and then at $t = 300$ s the k_f of the LSE was set to 10^{-3} m s^{-1} in order to create the transient concentration gradient of interest, as shown in Fig. 2.4. Figure 2.6 shows for both cases the simulated amperometric signals during the conditioning interval between 0 to 300 seconds, i.e., before activating the LSE to generate the gradient of interest.

Fig. 2.6(a) shows that the amperometric signal of the single sensing electrode stabilizes within 10 s after applying the potential bias, regardless of the reaction rate at which the sensing electrode is operated. In contrast, it takes about 300 s to obtain reasonably stable signals from the electrodes in a 2D MEA if the electrodes are operated at high reaction rate (Fig. 2.6(b)); however, the time to stabilize the signals is shorter if the electrodes are operated at low reaction rate (Fig. 2.6(c)). As expected, the effect of operating the sensing electrodes at high or low reaction rates is that the amplitude of the signals are correspondingly higher or lower, which for analytical

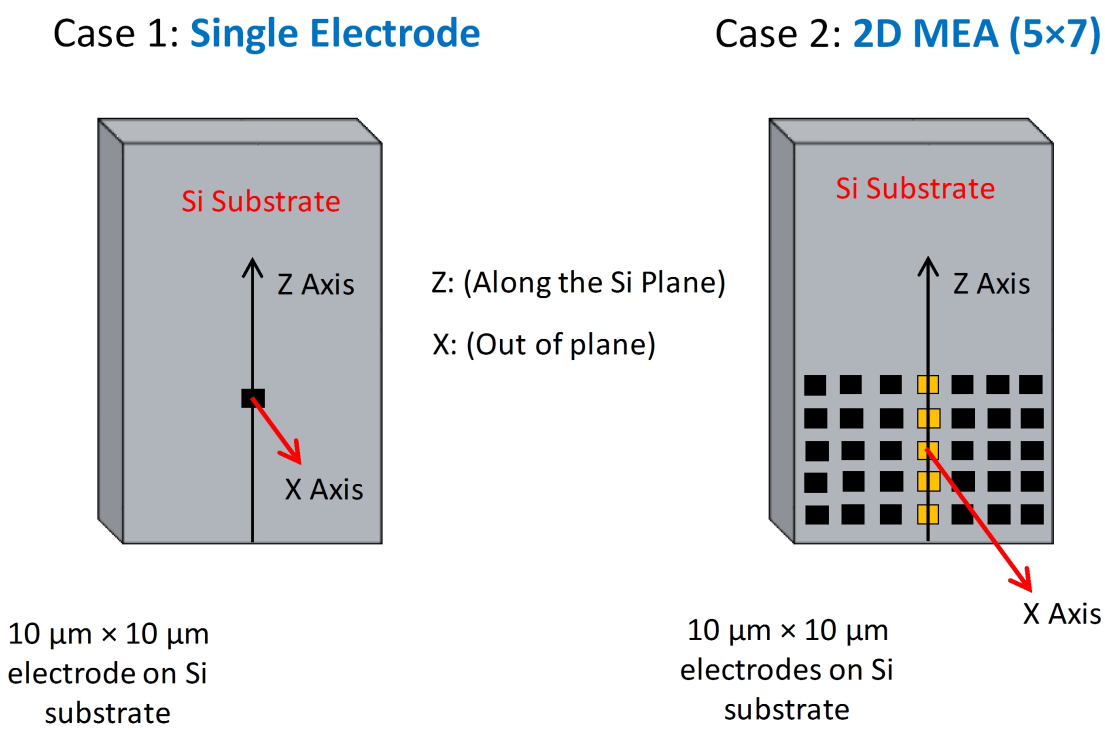

Fig. 2.5. Schematic diagrams of the sensing devices for the measurement of transient concentrations. Case 1 is a single sensing electrode on a silicon substrate. Case 2 is a 2D array of sensing electrodes on a silicon substrate (i.e., a 2D MEA). In both cases the electrodes are squares of 10 μm $\times$ 10 μm and the silicon plane is aligned with the z axis.

purposes translates into higher or lower sensitivities, respectively. Therefore, to obtain high sensitivity the sensing electrodes must be operated at high reaction rate.

However, some issues arise when multiple, closely-spaced sensing electrodes are operated simultaneously at high reaction rates, which is the situation of the simulated 2D MEA. A comparison of the high k_f signals at $t = 300$ s indicates that the single sensing electrode provides $\sim 2\times$ as much current as the sensing electrodes in the 2D MEA; therefore, the first expected issue is that the sensitivity of the sensing electrodes in a 2D MEA will be lower compared to that of a single electrode. This is interesting because in both cases the bulk concentration is the same but the amperometric signals

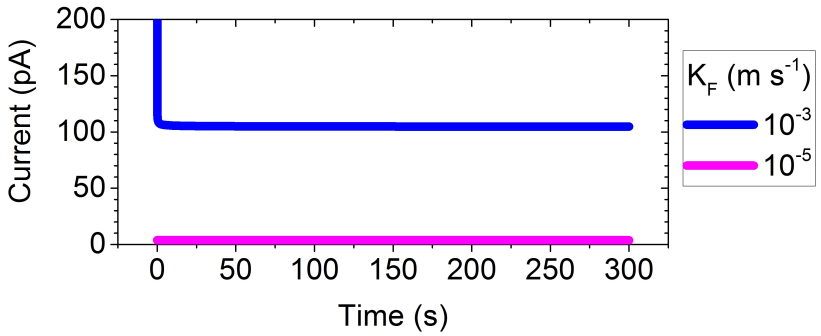

(a) Case 1: single sensing electrode.

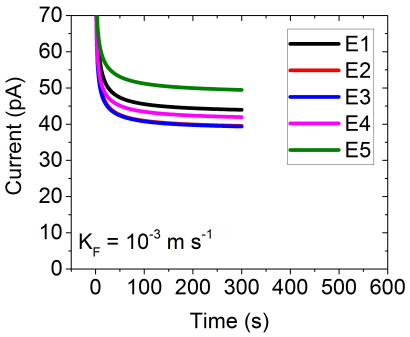

(b) Case 2: 2D MEA at high k_f

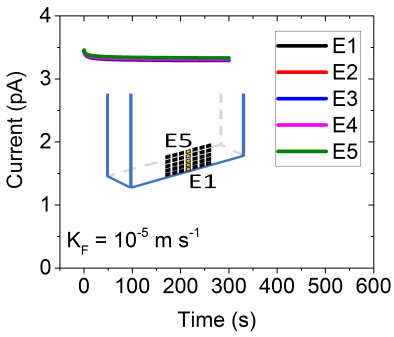

(c) Case 2: 2D MEA at low k_f

Fig. 2.6. The simulated amperometric signals for the two considered cases. (a) Case 1: single sensing electrode at two different k_f values corresponding to low (10^{-5} m s^{-1}) and high (10^{-3} m s^{-1}) reaction rates. (b) Case 2: 2D MEA with sensing electrodes operating at high k_f. (c) Case 2: 2D MEA with sensing electrodes operating at low k_f. The inset in (c) illustrates the labeling convention for the electrodes wherein E1 and E5 are the nearest and furthest electrodes with respect to the edge of the silicon substrate. The signals in (b) and (c) correspond to the column of electrodes highlighted in yellow in the inset included in (c).

are different, thus suggesting that sensing electrodes in an MEA collectively influence the signals among themselves. This effect is not an electrical cross-talk because all the electrodes are assumed to operate at the same potential of interest (E_{int}) and hence no current is expected to flow between pair of electrodes due to differences in their potentials. The second expected issue is that the sensitivities of the sensing

electrodes in a 2D MEA will differ among each other, just as illustrated in Fig. 2.6(b). This effect is correlated to the position of the sensing electrodes with respect to the zero-flux boundaries of the domain since the very presence of these boundaries effectively decrease the analyte transport rate toward the sensing electrodes, compared to the analyte transport rate that would occur if the boundaries were absent. In the presented simulations the zero-flux boundaries that are influencing the analyte transport are the bottom surface of the well, since the sensing electrodes are positioned within 800 μm from the LSE (which lies aligned to the bottom surface of the well), and the silicon substrate on which the sensing electrodes lie. In contrast to the described behavior, the difference in the sensitivities in a 2D MEA will decrease if the sensing electrodes are operated at low k_f, as indicated in Fig. 2.6(c); however, this "improvement" is at the expense of a drastic decrease in the sensitivity since at high k_f the signals are in the range of 40–55 pA whereas at low k_f the signals are in the range of 3.3–3.5 pA.

The above observations suggest that individual calibration factors should be acquired for each electrode in a 2D MEA with all the sensing electrodes operating simultaneously, in order to obtain the highest possible accuracy. Adopting this strategy for both cases, Case 1 and Case 2, the following sensitivities were defined:

$$S = \frac{i(t = 300 \text{ s})}{20\mu\text{M}} \tag{2.16}$$

$$S_{m,n} = \frac{i_{m,n}(t = 300 \text{ s})}{20\mu\text{M}} \tag{2.17}$$

where S is the sensitivity of the single sensing electrode, $S_{m,n}$ is the sensitivity of the sensing electrode in row m and column n in the 2D MEA, and $i(t = 300 \text{ s})$ is the magnitude of the amperometric signal at the time $t = 300$ seconds.

The simulation proceeds from $t = 300$ s onward by activating the reaction at the LSE (i.e., by setting $k_f = 10^{-3}$ m s^{-1} at the LSE surface) and then solving numerically the evolution of the amperometric signals in response to the transient gradient generated by the LSE. The obtained signals were converted into concentration values

using the calibration factors given by (2.16), for Case 1, and (2.17), for Case 2. The results of these simulated measurements of transient concentrations are shown in Fig. 2.7 for both of the considered cases.

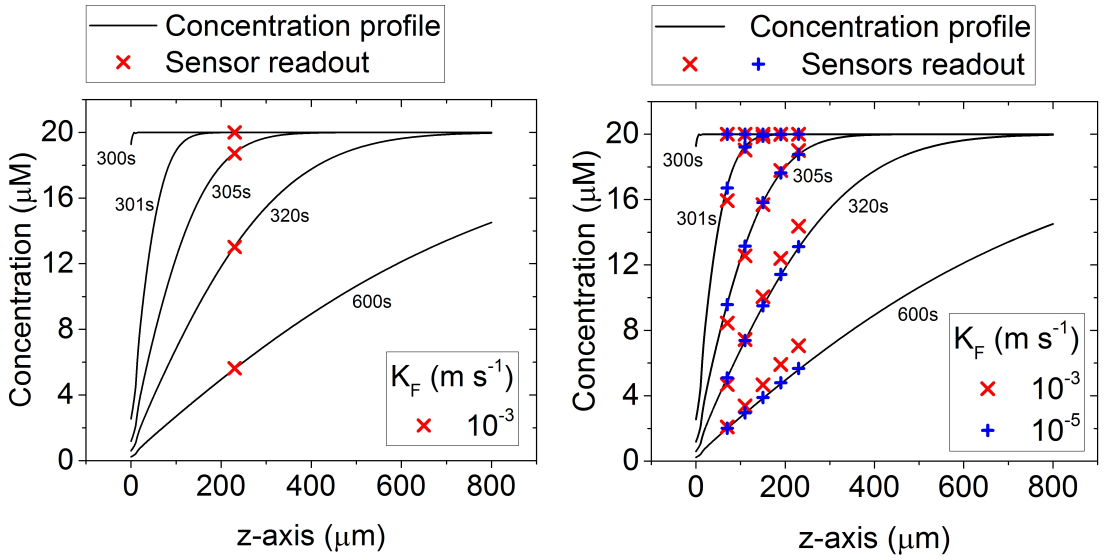

(a) Case 1: single sensing electrode.

(b) Case 2: 2D MEA

Fig. 2.7. The simulated measurement of transient concentrations at selected time points and for the two considered cases. (a) Case 1: single sensing electrode positioned at 210 μm from the LSE and operated at high k_f measures the transient concentration accurately. (b) Case 2: 2D MEA with sensing electrodes positioned within 90–210 μm from the LSE and operated at high (red symbols) and low (blue symbols) k_f. While the sensing electrodes at low k_f measure the transient concentrations accurately over the whole time window of the transient (from 300 to 600 s), the same electrodes at high k_f report reasonable values only within the first 5 seconds of the transient.

Fig. 2.7(a) indicates that a single sensing electrode can track accurately the transient concentration when operated at high k_f, which is the desirable situation given that high k_f means high sensitivity; however, multiple sensing electrodes operated at high k_f (Fig. 2.7(b)) will report inaccurate concentration values at some point during the measurement of the transient concentration of interest. Fig. 2.8 shows the concentration profiles at $t = 600$ s with and without the influence of the sensing

electrodes, for both of the considered cases. Fig. 2.8(a) shows that a single sensing electrode operated at high k_f causes a significant but localized perturbation to the concentration profile of interest. The localized nature of this perturbation is size relative, i.e., this effect is "local" just because the size of the gradient generator is $\sim 160\times$ larger than the size of the single sensing electrode; therefore, it is expected that this effect turns out to be less "local" when multiple sensing electrodes are operating simultaneously since the footprint area occupied by all the sensing electrodes begins to be comparable to the size of the gradient generator. This is precisely the case shown in Fig. 2.8(b) in which multiple sensing electrodes operated at high k_f cause a significant perturbation to the concentration profile of interest and therefore the very act of measuring the transient concentrations is changing the transient concentrations themselves. In contrast, if the same array of electrodes is operated a low k_f, the perturbation to the concentration profile of interest is barely visible, as shown in Fig. 2.8(c).

According to the above simulations the answer to the initial question "do the sensing electrodes measure the transient concentrations reliably?" is: yes, the sensing electrodes do measure the transient concentrations reliably as long as the perturbation to the concentration profile of interest, due to the sensing electrodes, is minuscule.

Selection of 1D over 2D to be the MEA architecture

The set of simulations presented here illustrates clearly the trade-off between the sensitivity of the sensing electrodes (which was tuned by modifying k_f) and the number of sensing electrodes. Therefore, the problem of reliable measurement of transient concentrations reduces itself to the problem of maximizing the sensitivity and the number of sensing electrodes while minimizing the perturbation to the concentration profile of interest. In this regard, a 1D array of sensing electrodes seems to be a good compromise and for this reason it was selected to be the architecture of the MEA. It is important to note that this conclusion holds only for arrays of

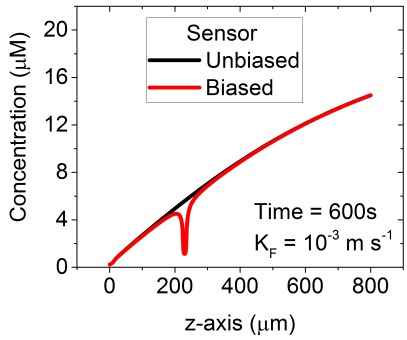

(a) Case 1: single sensing electrode.

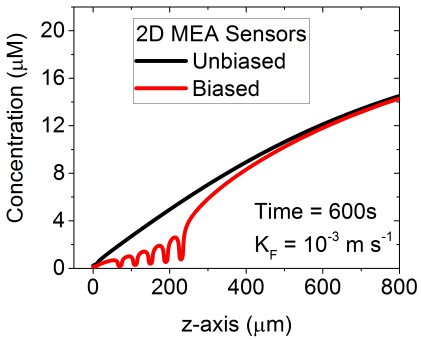

(b) Case 2: 2D MEA at high k_f.

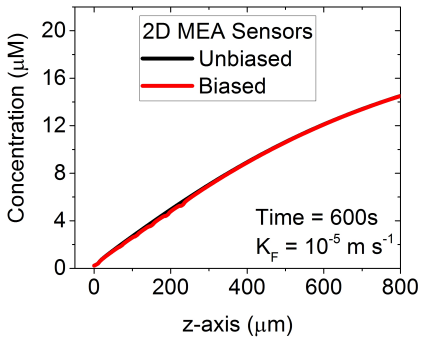

(c) Case 2: 2D MEA at low k_f.

Fig. 2.8. The concentration profiles at $t = 600$ s with and without the influence of the sensing electrodes for the two considered cases. (a) Case 1: single sensing electrode positioned at 210 μm from the LSE and operated at high k_f. (b) Case 2: 2D MEA with sensing electrodes positioned within 90–210 μm from the LSE and operated at high k_f. (c) Case 2: 2D MEA with sensing electrodes positioned within 90–210 μm from the LSE and operated at low k_f.

sensing electrodes operated amperometrically. Separate analyses must be conducted if the sensing electrodes are to be operated using other electrochemical techniques, e.g., potentiometry, voltammetry, electrochemical impedance, etc. Analysis of these additional possibilities is out of the scope of this thesis.

2.2.3 Geometry of the microelectrode array and implications thereof

1D MEAs have two geometrical parameters, electrode size and inter-electrode separation, which must be customized to fit the requirements imposed by different transient gradients of interest. However, modification of the electrode size and the inter-electrode separation has implications that must be accounted for on a per case basis. This section elaborate on those implications.

Implications of the electrode size in a microelectrode array

The amperometric signal, $i_{\mathrm{H_2O_2}}$, of a sensing electrode due to the electrooxidation of H_2O_2 is essentially described by Eq. (2.2) which, for the sake of a better understanding, is replicated here with some nomenclature modifications:

$$i_{\mathrm{H_2O_2}} = nFAk_f C_{\mathrm{H_2O_2}}(0,t) \tag{2.18}$$

Eq. (2.18) indicates that the amperometric signal can be maximized by increasing either the electrode surface area, A, or the reaction rate, k_f. The effects of modifying k_f while keeping A constant were studied in the simulations presented in the previous section. Now the discussion is regarding the implications of modifying A while keeping k_f constant. The following aspects of the sensing electrode are affected by a change in A:

1. The magnitude of the amperometric signal as indicated by Eq. (2.18).

2. The charge transfer resistance, R_{ct}, of the sensing electrode, as indicated by Eq. (2.19), since i_0 is directly proportional to A (see Eq. (2.8)).

$$R_{ct} = \frac{RT}{nFi_0} \tag{2.19}$$

3. The double layer capacitance, C_{dl}, as indicated by the basic relation for the capacitance of a parallel plate capacitor (Eq. (2.20)).

$$C = \varepsilon \frac{A}{d} \tag{2.20}$$

4. The electrode impedance, Z, as indicated by Eq. (2.21), where Z_{dl} is the impedance of the double layer capacitance.

$$Z = R_{ct} \parallel Z_{dl} = R_{ct} \parallel \frac{1}{j\omega C_{dl}} \propto \frac{1}{A} \tag{2.21}$$

5. The noise of the electrode since the RMS value of the Johnson noise, v_n, is given by Eq. (2.22), where k_b is the Boltzmann constant, T is the temperature, R is the resistance, and Δf is the frequency band of the noise. In the case of the sensing electrode, $R = R_{ct}$, and $R_{ct} \propto 1/A$ as indicated by Eq. (2.19).

$$v_n = \sqrt{4k_bTR\,(\Delta f)} \tag{2.22}$$

6. The amount of enzyme that can be immobilized on the surface of the sensing electrode.

7. The iR_u potential drop, which is the drop in potential caused by the passage of current (i.e., $i_{\mathrm{H_2O_2}}$) through the resistance of the portion of solution that is uncompensated (hence called R_u). R_u arises from the fact that the reference electrode cannot occupy the same geometrical space as the sensing electrode and therefore there will always exist a certain amount of uncompensated resistance in the electrochemical cell. R_u is approximately given by Eq. (2.23) where κ is the conductivity of the solution and r_{se} is the radius of the sensing electrode (assuming that the sensing electrode can be approximated by a disk of radius r_{se}).

$$R_u \approx \frac{1}{4\pi\kappa r_{se}} \tag{2.23}$$

8. The cell time constant, τ, which is the time it takes to charge the double layer capacitance. τ is given by Eq. (2.24) where R_u is the uncompensated resistance, C_{dl} is the double layer capacitance, κ is the conductivity of the solution, and r_{se} is the radius of the sensing electrode (assuming that the sensing electrode can be approximated by a disk of radius r_{se}).

$$\tau = R_uC_{dl} \approx \frac{1}{4\pi\kappa r_{se}}C_{dl} \propto r_{se} \tag{2.24}$$

The conclusion is that any change in A comes along with changes in other aspects of the sensing electrode and therefore good judgment is warranted when specifying the electrode size for a specific purpose.

Implications of the inter-electrode separation in a microelectrode array

The implications of increasing the inter-electrode separation are straightforward. Since the transient gradient of interest sets the spatial scale over which the concentrations must be measured, an increase in the inter-electrode separation reduces the number of data points within a given spatial scale, thus translating into a reduced spatial resolution of the gradient of interest, as depicted in Fig. 2.9.

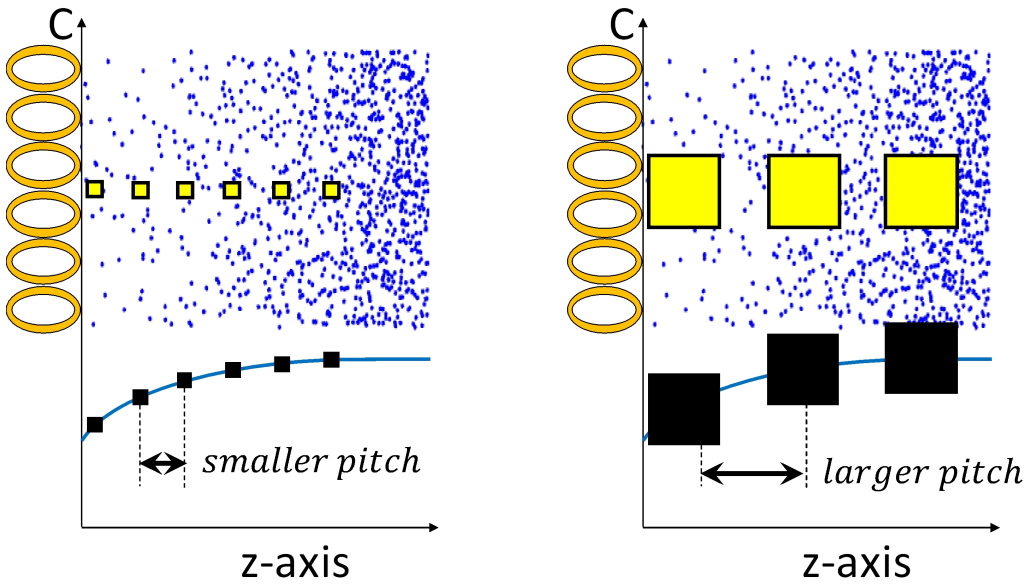

Fig. 2.9. The implication of increasing the inter-electrode separation in an MEA. Since the spatial scale is dictated by the transient gradient of interest, any increase in the inter-electrode separation will reduce the spatial resolution of the gradient of interest.

Electrode sizes and inter-electrode separations used in this work

The experimental diffusion-reaction system (i.e., the artificial analog) used in this thesis enables to set up transient gradients with spatial scales in sub-millimeter scale, in response to sub-second excitation pulses. For this type of gradients, the electrodes were fabricated with size 3 μm $\times$ 3 μm, separated by 15 μm, and electrodes with size 5 μm $\times$ 5 μm, separated by 30 μm. Since the fabrication yield for the 3 μm $\times$ 3 μm electrodes was very low compared to the yield for 5 μm $\times$ 5 μm, the measurements were performed with the 5 μm $\times$ 5 μm electrodes.

In the physiological applications presented here the transient gradients of interest occurred over larger temporal and spatial scales but with much smaller changes in concentration, thus requiring the design of larger, more widely spaced sensing electrodes. Therefore, for the physiological measurements the electrodes were squares of 10 μm $\times$ 10 μm with inter-electrode separation of 140 μm, in the case of astrocytes and glioblastoma multiforme cell lines, or 280 μm, in the case of human bronchial epithelial and small cell lung cancer cell lines.

2.3 Fabrication of the microelectrode array

Figure 2.10 shows cross sections and top views of the fabrication process. Briefly, a silicon substrate was passivated by low pressure chemical vapor deposition (LPCVD) of 300 nm silicon nitride. The electrode material, titanium/platinum (10nm/100nm), was deposited by electron-beam evaporation, photo-lithographically patterned, and processed by lift-off. Photolithographically patterned SU-8 photoresist (5 μm thick) was used to selectively passivate the lead traces and to define a large-area well containing the MEA. The silicon wafer was diced, and each die was wire-bonded to a printed circuit board (PCB). The wire bonds were covered with either apiezon wax or epoxy resin to prevent exposure to the solution. Figure 2.11 shows a photograph of a representative MEA after the fabrication process.

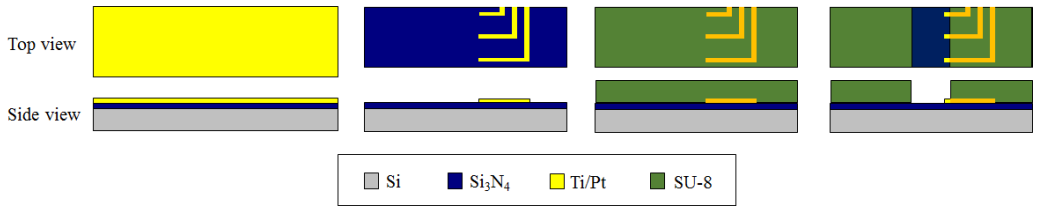

Fig. 2.10. Cross sections and top views of the fabrication process.

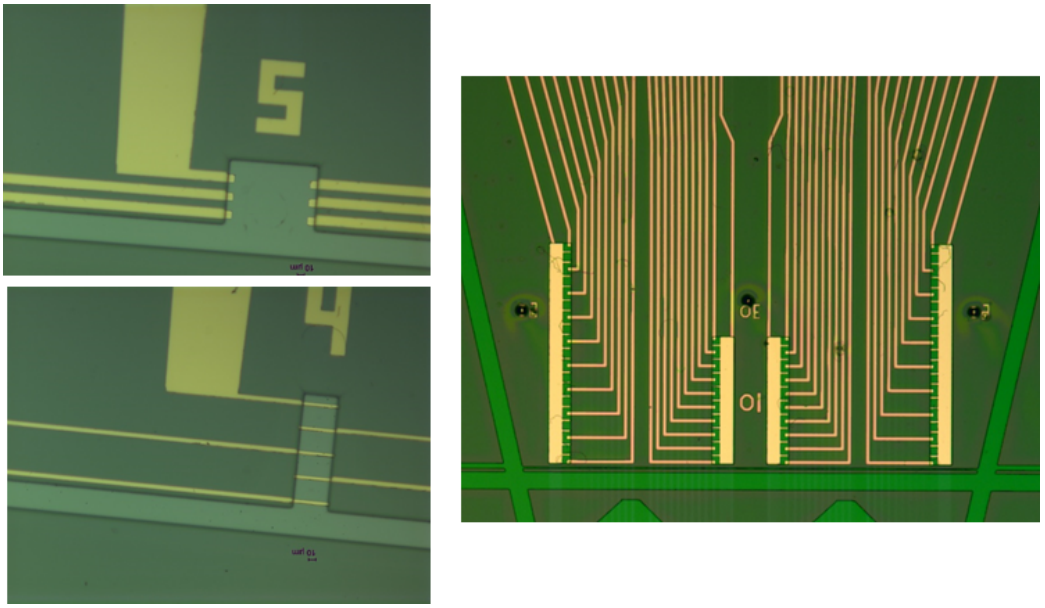

Fig. 2.11. Photographs of various representative MEA designs. Top left: First-generation MEA containing two columns of three electrodes with size of 10 μm $\times$ 10 μm. Bottom left: First-generation MEA containing five band electrodes with size of 50 μm $\times$ 5 μm. Right: Second-generation MEA containing four columns of ten electrodes with sizes of 10 μm $\times$ 10 μm and 20 μm $\times$ 20 μm.

2.4 Common problems of amperometric sensors and strategies to achieve the technical specifications

The definition of the MEA architecture, electrode size and inter-electrode separation is just part of the solution. The other part of the solution consists in understanding the deviations from the non-idealities and then devising strategies to obtain high quality experimental signals despite the existence of the non-idealities. During all

the work developed for this thesis, the most intriguing and detrimental non-ideality was the instability of the amperometric signals. In fact, the instability and the non-reproducibility of the amperometric signals have been identified as ubiquitous issues of amperometric sensors [27]. Since the signals arise in response to the analyte concentration, it is therefore equivalent and more illustrative to discuss the issue of signal instability in terms of variability of the sensitivity.

The variability of the sensitivity manifests itself in four types:

1. Sensitivity variations during an experiment. The literature refers to this as signal drift.

2. Sensitivity variations from experiment to experiment.

3. Sensitivity variations from electrode to electrode in an MEA.

4. Sensitivity variations from MEA to MEA.

The four types of sensitivity variability are routinely observed in the literature of amperometric sensors. For instance, sensitivity variation during an experiment is inherent to both single-electrode [26, 27, 50, 51] and MEA approaches [43, 45]; sensitivity variation from experiment to experiment is typically within 10-20% [37, 38, 52]; and sensitivity variation from electrode to electrode is also typically within 10-20% [33, 36, 37, 39, 42–44].

2.4.1 Sensitivity variation during an experiment

The basic test to observe the effects of sensitivity variability during an experiment is described in Fig. 2.12 and is supported by the simulations shown in Fig. 2.6(a). After the conditioning interval, the expected result from the described test is the observation of a stable signal. Depending on the volume and the analyte concentration, the signal should be stable during a sizable period of time since the concentration in the vessel is constant and uniform. However, the experimental results are drastically

different. For instance, Fig. 2.13 shows that the signals in response to 1 mM H_2O_2 did not become stable during a time interval of 2000 s. The same was true for glucose measurements, as shown in Fig. 2.14. In fact, electrodes functionalized with glucose oxidase (to render them selective to glucose) may exhibit signals that drift upwards, as shown in Fig. 2.15.

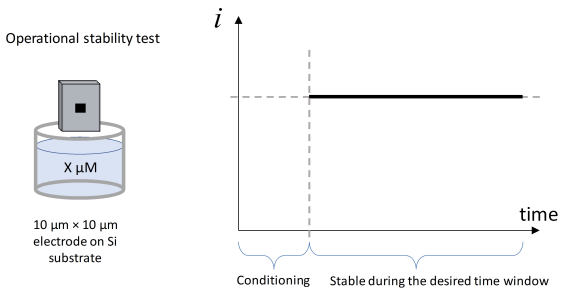

Fig. 2.12. Schematic diagram illustrating the basic stability test for an amperometric sensing electrode. The sensing electrode (assumed to be 10 μm $\times$ 10 μm) is immersed in a solution with inert electrolyte and analyte concentration of X μM and then biased amperometrically. After a conditioning interval, which varies on a per case basis, the signal should be stable for a sizable time length since the concentration in the vessel is constant and uniformly distributed throughout the volume.

2.4.2 Sensitivity variations from experiment to experiment

Sensitivity variation from experiment to experiment was frequently observed and the patterns of variation were difficult to rationalize. For instance, Figures 2.16 and 2.17 shows the sensitivity variations from experiment to experiment in typical calibration experiments to H_2O_2 and glucose, respectively.

2.4.3 Sensitivity variations from electrode to electrode in an MEA

As suggested from the simulations performed in Section 2.2, multiple electrodes operated at high reaction rates will exhibit variations in the sensitivity from electrode

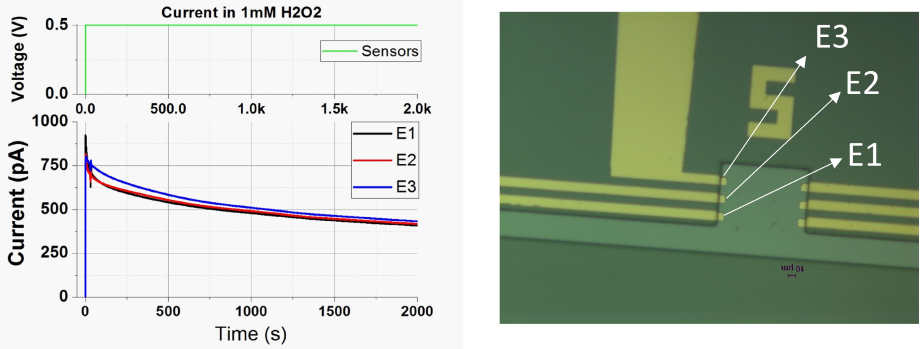

Fig. 2.13. The amperometric responses of three seemingly identical, 10 μm $\times$ 10 μm sensing electrodes. A potential of 0.5 V vs. Reference is applied simultaneously to the three sensing electrodes in the MEA. A photograph of the three electrodes is shown on the right hand side. The amperometric signals from the three electrodes (denoted as E1, E2 and E3) are obtained in unstirred solution. The solution is 1 mM H_2O_2 in 0.01 M PBS (pH 7.4). In contrast to the expected result, the amperometric signals did not achieve the steady state, meaning that they drifted during the time window of the experiment.

to electrode even if the electrodes are perfectly identical. This effect was observed experimentally, as shown in Fig. 2.18, except that in the experiments the effect seems to be exacerbated with respect to the simulations.

2.4.4 Consequences of the sensitivity variability

The sensitivity variability prevents the accurate measurement of transient gradients using the conventional calibration method for amperometric MEAs. In the conventional calibration method, all the electrodes are assumed to have the same sensitivity which is determined as the average value of sensitivity calculated over all the electrodes in the MEA. Therefore, if the changes in the transient concentrations of interest are smaller than the uncertainty (as obtained from the calculation of the average sensitivity over all the electrodes in the MEA), the accuracy of the measurements will not be sufficient as to determine the transient gradients.

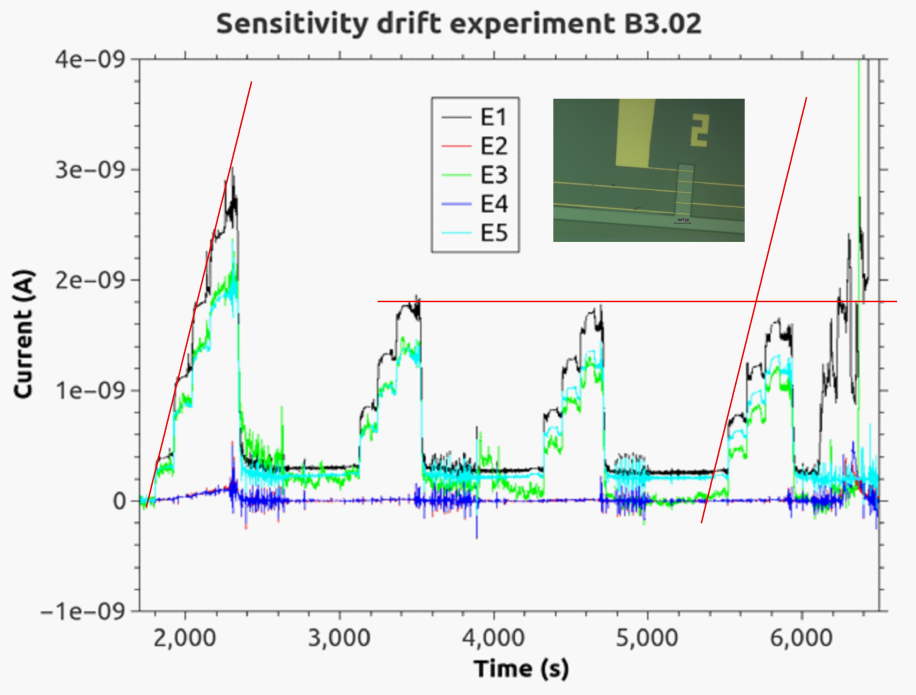

Fig. 2.14. The amperometric responses of five 50 μm $\times$ 5 μm sensing electrodes in a 1D MEA. Three electrodes (E1, E3, and E5) are functionalized with glucose oxidase (GOx) to respond selectively to glucose. The other electrodes (E2 and E4) are just bare platinum electrodes which are intended to detect any H_2O_2 escaping from E1, E3 or E5. The inset shows a photograph of the five electrodes in the MEA. The stepwise increments in the signals correspond to four-step increments in the glucose concentration in order to create a calibration curve. After the four concentration step, the solution is diluted down to the concentration corresponding to the first glucose concentration step, and then three more glucose concentration steps are performed to obtain a second calibration curve. This procedure is repeated two more times to have in total four calibration curves in 6000 s. The bare Pt electrodes exhibit a poor response to glucose; however, these electrodes show signals that slightly increase with time thus indicating that some amount of H_2O_2 is indeed escaping from the GOx-functionalized electrodes.

The variability from electrode to electrode is commonly reported in the literature and is calculated as the standard deviation of the mean value of sensitivity from all the electrodes in the MEA. Similarly, the variability from experiment to experiment

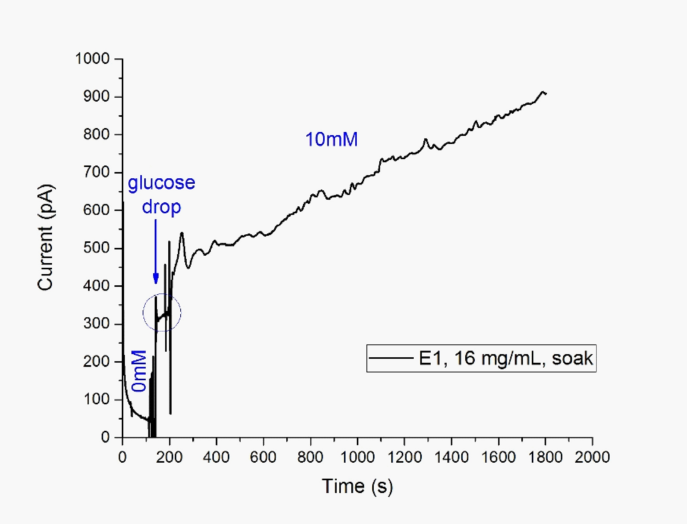

Fig. 2.15. The amperometric response of a 10 μm $\times$ 10 μm sensing electrode. The electrode is functionalized with glucose oxidase (GOx, 16 mg/ml) to respond selectively to glucose. The signal is conditioned in zero glucose for the initial 300 s; then a drop of glucose solution is added to bring the glucose concentration up to 10 mM; then the solution is stirred with a magnetic bar during 60 s (the encircled interval) in order to homogenize the glucose concentration; and finally the experiment is allowed to run in static solution conditions until the end of the experiment at 2000 s. The signal increases with time despite the glucose concentration is constant at 10 mM.

is reported as the standard deviation of the mean value of sensitivity from the total number of replicated experiments (typically n = 3 or greater). The data collected during the development of this thesis indicate that the average sensitivity over all the electrodes in a given MEA $\pm$ standard deviation was 1.65 $\pm$ 0.36 nA mM^{-1}, yielding a variability from electrode to electrode of 21.8%, and the variability from experiment to experiment was 2.5%, as obtained from triplicate experiments.

The implications of having these variations in the sensitivity can be better explained with the following example: for an experiment performed at 1 mM of initial analyte concentration, a 21.8% of variability from electrode to electrode indicates that the measurements between any pair of adjacent sensing electrodes will not be able to distinguish changes in local concentrations smaller than 218 μM. Since changes

in concentration that small are typical in physiological settings, the MEA measurements would be pointless. Therefore, some corrective action must be taken against the sensitivity variability.

2.4.5 Strategies to address the sensitivity variability

Gaining a better understanding about the sensing system is always the best way to proceed. The first aspect that must be addressed is the repeatability of the fabrication process, which can be achieved by strictly adhering to a fabrication protocol. Assuming that the fabrication process is highly repeatable, the second aspect to address is the amount of charge injected during platinum black electrodeposition. As suggested by simulations and experimental evidence, the effect of position of the sensing electrodes with respect to the zero-flux boundaries is practically unavoidable, since different sensing electrodes will necessarily be positioned at different points with respect to something else (e.g., a passivation layer, the vessel walls, etc.); therefore, if the protocol to deposit platinum black is to apply the same number of electrodeposition cycles to all the electrodes, then some electrodes will receive more platinum black than others due to the hindering effects caused by the nearby zero-flux boundaries. An example of this observation is shown in Fig. 2.19. To address this issue it will be necessary to control for the amount of injected charge such that some electrodes receive more deposition cycles to compensate for the hindrances in the mass transport.

The third aspect to address is the detaching of the loosely bound enzyme. Fig. 2.20 shows that after soaking the MEA for 2000 s in 10 mM glucose (black curve), the two subsequent experiments (red and blue curves) show a decrease in the sensitivity but, most importantly, these two experiments provide consistently the same signal amplitude, thus indicating that the experiments are repeatable from one to the other. Additionally, the signal is stable for an interval of 3600 s, which is longer than anything observed before. However, after the 3600s the signal starts to increase thus ruining

all what has been accomplished, since unstable signals (either drifting downward or upward) are not reliable for measurement of tiny changes in transient concentrations.

The fourth aspect to address is the prevention of enzyme binding to the SU-8 passivation layer. The dangling bonds in the surface of the SU-8 are prone to spontaneously form covalent bonds with the amine groups of the enzyme [53], and when this occurs the amperometric signals tend to increase with the time since the enzyme bonded to the SU-8 releases H_2O_2 molecules that ultimately reach the surface of the sensing electrodes. This explains why the blue signal in Fig. 2.20 eventually starts increasing with time after about 3600 s of stability. Following the recipe provided by Thomas et. al. [53], the remarkably stable signals shown in Fig. 2.21 were obtained. The recipe consists in soaking the MEA in a PBS solution containing 12 mg/ml of tris(hydroxymethyl)aminomethane (TRIS) and 1 mg/ml glycine for at least 24 hours at room temperature. These two molecules are primary amines that form covalent bonds with the dangling bonds in the SU-8 surface, such that the glucose oxidase do not find any available site to bond at the moment of the glucose oxidase functionalization.

So far the signals are stable enough for an interval of two hours, as demonstrated experimentally in Fig. 2.21. This is indeed a success. However, the reuse of the same MEA in various consecutive experiments shows that the issue of sensitivity variation from experiment to experiment still remains, as shown in Fig. 2.22. Therefore, something else must be done in order to acquire reliable signals every time the MEA is used, as will be discussed in Chapter 3.

2.5 Conclusions

1. Depending on their kinetic and geometrical characteristics, the gradients of interest set the temporal and spatial scales over which they must be captured. In this Section, a gradient generator in the form of a disk with 1.6 mm in diameter was studied by simulations over a time window of 300 s. The gradient generator

acts to create a time-dependent gradient as it consumes the analyte nearby, hence it is called "large sink electrode" (LSE), and mimics the situation where cells consume analyte in a 2D culture. It was observed that the quickest and largest change in concentration occurs at the surface of the gradient generator and within 1 second of having activated the onset of the gradient. During this time scale of 1 s, the concentration field grew accordingly but was practically contained within 200 μm from the surface of the LSE. However, after this quick transient change, the rate of change in concentration steadily slows down with time and the concentration field spreads out, reaching distances further than 800 μm in a time scale from 1–300 seconds. Therefore, a trade-off between time and space is imposed for the measurement of the transient gradient. On the one hand, if the purpose is to track the early dynamics of the gradient, then multiple simultaneous concentration measurements must be done within 200 μm from the gradient generator and with a sub-second sampling period. On the other hand, if the early dynamics can be obviated, then it will be sufficient with having multiple simultaneous concentration measurements within 800 μm from the gradient generator and with a sampling period that can be > 1 second. Furthermore, if the purpose is to gain mechanistic knowledge about the kinetics of the process generating the gradient of interest, then the transient gradient must be measured over the whole temporal and spatial scales, thus rendering this task challenging.

2. The problem of measuring the transient gradient is reduced to the problem of maximizing the number of sensing electrodes and the sensitivities thereof while causing the least perturbation to the gradient of interest. In this regard, it was found by means of simulations that a 2D array of sensing electrodes operated at high reaction rates will cause a large perturbation to the gradient of interest, significant enough to render the concentration measurements inaccurate. Therefore, a 1D array of sensing electrodes is proposed here as a good compro-

mise between sensitivity, number of sensing electrodes, and perturbation to the gradient of interest.

2.6 Acknowledgements

The author acknowledges the valuable insights, comments and guidance provided by Prof. David B. Janes, Prof. Jenna L. Rickus, and Prof. Muhammad A. Alam.

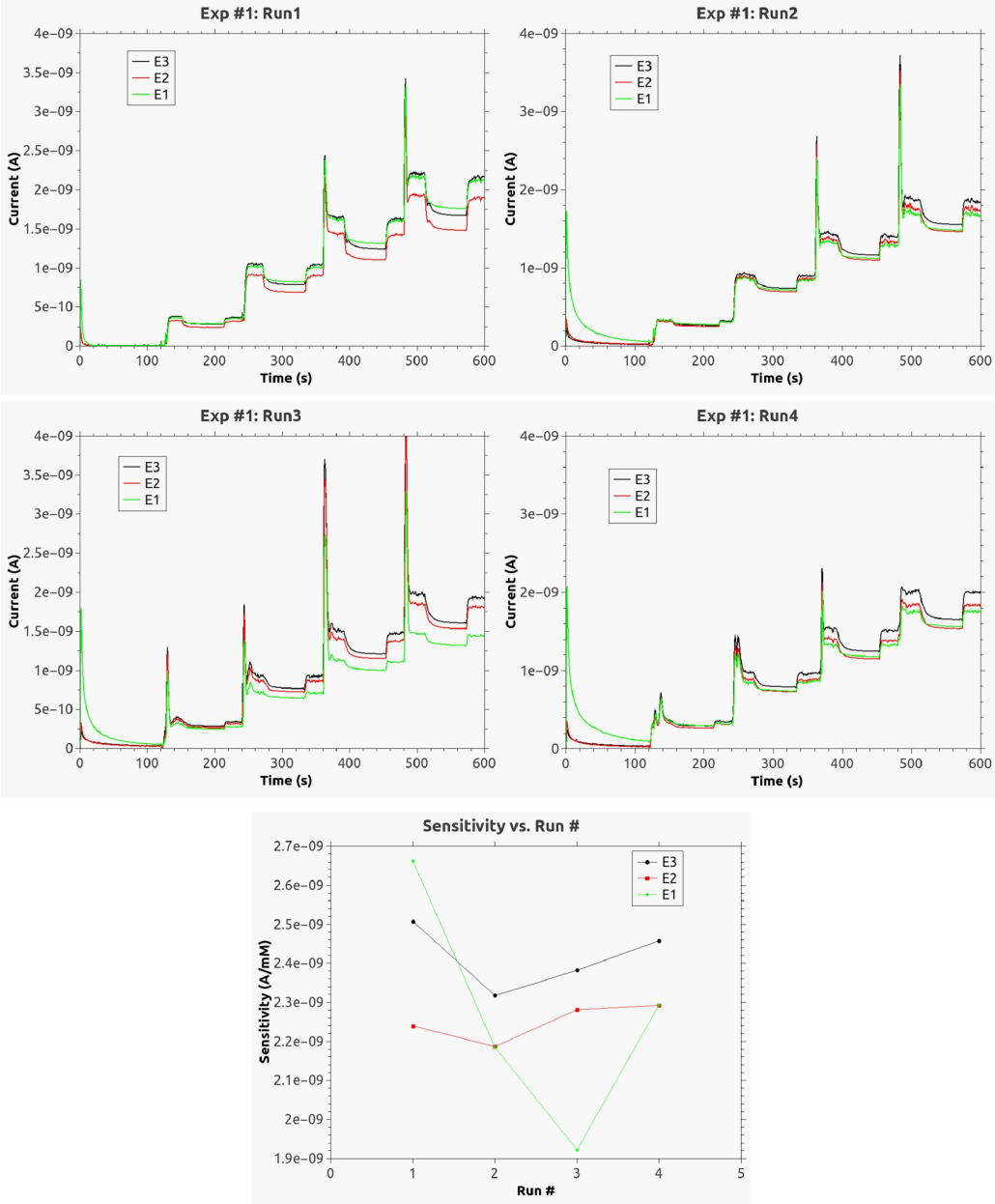

Fig. 2.16. The amperometric signals in quadruplicate H_2O_2 calibrations using three 10 μm $\times$ 10 μm sensing electrodes in an MEA. The replicates are designated Run1–Run4. The signal is conditioned in zero H_2O_2 for the initial 120 s; then drops of H_2O_2 solution are added to bring the H_2O_2 concentrations up to 0.1, 0.3, 0.5 and 0.7 mM; after addition of each drop the solution is stirred with a magnetic bar during 30 s, then remains static for 60 s, and then is stirred again for 30 s; at the end of this 30 s stirring, the next drop of H_2O_2 solution is added and the stir/static/stir procedure is repeated. The bottom most plot clearly shows that the sensitivity varies from Run to Run, i.e., from experiment to experiment.

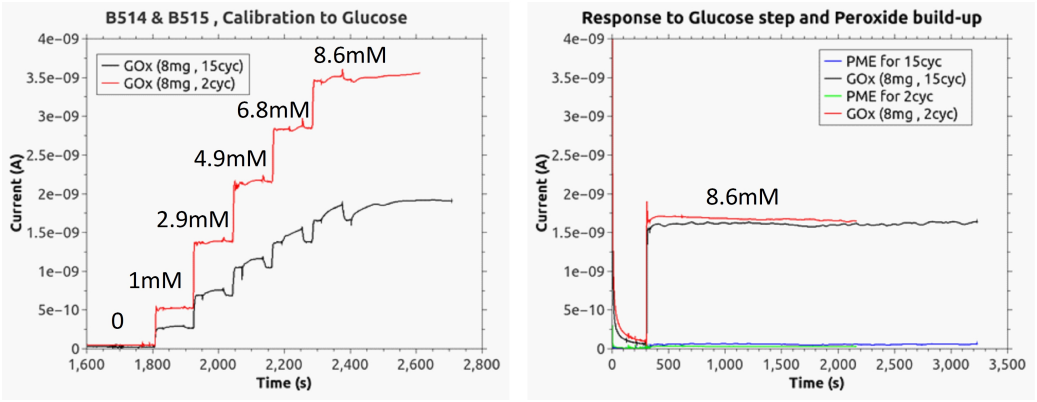

Fig. 2.17. The amperometric signals from two 10 μm $\times$ 10 μm sensing electrodes which are functionalized with glucose oxidase (GOx) to respond selectively to glucose. Calibration curves for the two electrodes are shown in the left plot. The glucose concentrations at the concentration steps are indicated in each plot. During the GOx functionalization, one electrode received more cyclic voltammetry cycles (15 vs. 2 cycles) than the other in order to observe the effect of increasing the thickness of the polymer matrix. The electrode with only 2 cycles showed more sensitivity than the one with 15 cycles (left plot). However, in a subsequent experiment (right plot) the sensitivity of the electrode with 2 cycles was practically the same as the sensitivity with 15 cycles. This observation indicates that for the electrode with 2 cycles the sensitivity changed significantly from one experiment to the other.

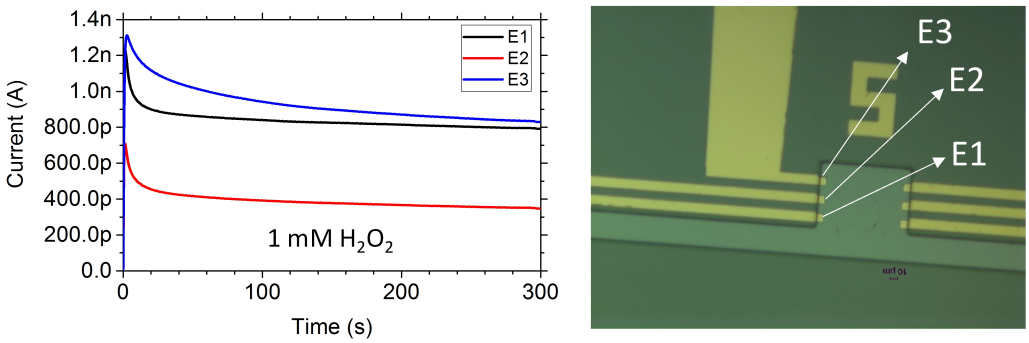

Fig. 2.18. The amperometric signals from three seemingly identical 10 μm $\times$ 10 μm sensing electrodes in response to 1 mM H_2O_2. The three electrodes respond differently despite of being nominally identical. This observation is partially explained by the effect of the relative position of the sensing electrodes with respect to the zero-flux boundaries which acts to hinder the mass transport toward certain electrodes, as discussed in Section 2.2.

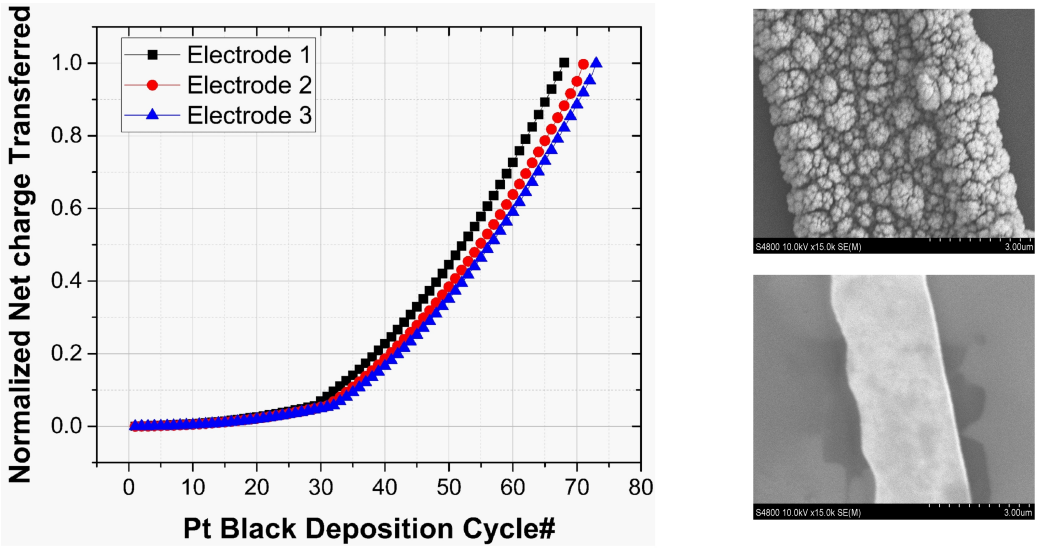

Fig. 2.19. The normalized charge injected to three sensing electrodes in an MEA during pt black deposition. Applying the same amount of deposition cycles to all the electrodes in the array will lead to some electrodes having more pt black than others. Since Pt black increases the catalytic rate for the oxidation of H_2O_2, some electrodes will exhibit much more sensitivity than others. To help equalize this situation, the deposition should control for the amount of injected charge. The photographs show an electrode before and after the deposition of Pt black.

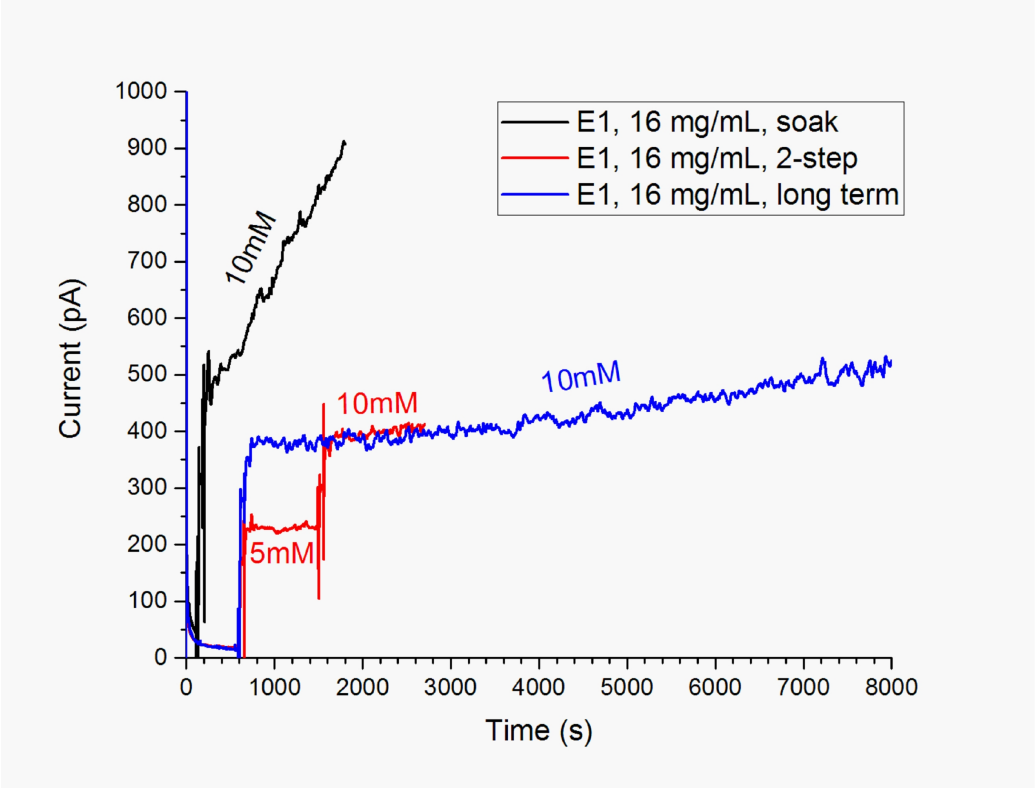

Fig. 2.20. Non-selective binding of glucose oxidase (GOx) onto the substrate yields signal (black curve) that rapidly increases with time despite the glucose concentration being uniform and constant at 10 mM. After the treatment to remove non-selectively bound GOX, the sensors show consistent responses for steps in concentration from 0 to 5 to 10 mM (red curve) and from 0 to 10 mM (blue curve). The signal at 10 mM (blue curve) is stable up to 3600 s. After 3600 s, the increase in the signal is believed to be due to H_2O_2 build-up. These results indicate that measurements are reliable within the 3600 s time window.

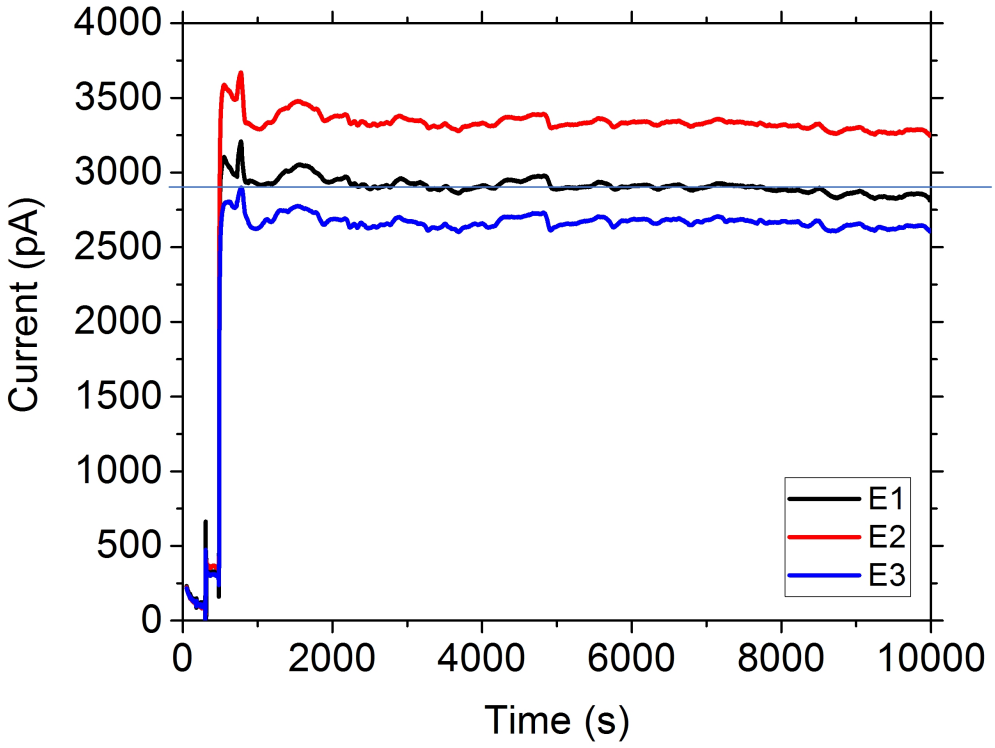

Fig. 2.21. The treatment of the SU-8 surface by soaking in a solution of primary amines helps reduce the non-selective binding of glucose oxidase on the SU-8 surface and therefore the signals of the three sensing electrodes are stable for longer. The horizontal line is just a guide to the eye.

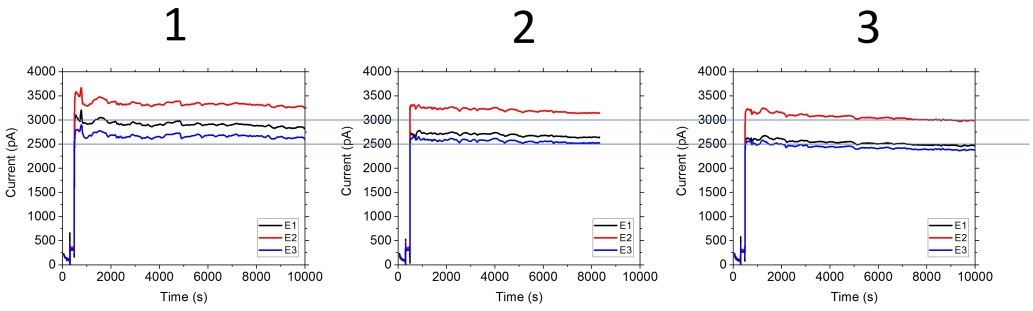

Fig. 2.22. The signals in response to 15 mM glucose from three electrodes in an MEA during three consecutive experiments, denoted by the numbers 1, 2 and 3 on top of each plot. The signals are consistently stable over periods as long as 10,000 s, thus constituting an outstanding result. However, the issue of sensitivity variation from experiment to experiment still remains. The solution to this persistent issue is discussed in Chapter 3. The horizontal lines are just guides to the eye.

3. MEASUREMENT OF FAST TRANSIENT GRADIENTS USING A CONTROLLABLE, NON-PHYSIOLOGICAL REACTION-DIFFUSION SYSTEM

The content in this chapter corresponds to a published journal article: Sridharan SV, Rivera JF, Nolan JK, Alam MA, Rickus JL, Janes DB, *"On-chip microelectrode array and in situ transient calibration for measurement of transient concentration gradients near surfaces of 2D cell cultures"*, Sensors and Actuators B: Chemical, 2018 May 1, 260:519–528.

3.1 Abstract

Amperometric microelectrode arrays (MEAs) interrogate the concentration at multiple positions simultaneously and with sufficient sampling rates, thus being able to capture fast transient gradients. However, sensitivity variability issues in amperometric MEAs degrade the reliability of the measurements, particularly at the small concentration scales found in physiological studies. This paper describes the development of on-chip platinum amperometric MEAs and in-situ transient calibration for reliable measurement of physiological transient concentration gradients. The designed MEA geometry facilitates positioning near a 2D cell culture setup, and the proposed in-situ transient calibration minimizes the effects of sensitivity variability, thus allowing for calculation of gradients based on concentration differences between closely spaced electrodes. The effectiveness of the MEA and the in-situ transient calibration was evaluated by measuring controllably-generated gradients, and then calculating the difference between experimental and simulated data using normalized time analysis. Gradients generated by periodic uptake intervals as fast as 150 ms followed by recovery intervals of 60 s were measured over a spatial range of 70 μm,

with spatial resolution of 35 μm, and sampling time and measurement time of 10 ms. Transient gradients of hydrogen peroxide were also measured above the surface of a 2D cell culture of human astrocytes, thus demonstrating the approach in actual physiological measurements.

3.2 Introduction

Concentration gradients are crucial in many biological processes [7, 13, 19, 54–60] at the single-cell, tissue, and organ levels. Cells act as sources and sinks of molecules via release and uptake processes, respectively, resulting in concentration gradients in the extracellular space. In adherent 2D cell cultures, these uptake/release processes generate concentration gradients exhibiting spatial scales of hundreds to thousands of microns with time scales ranging from steady-state to millisecond regimes, and local concentration changes going up to a few hundreds of μM [14, 61–64]. The magnitude, direction, and time scales of the gradients from the cell surface carry information that is communicated both internally to the cell and externally to neighboring cells.

Gradient measurements require accurate absolute concentration values at various spatial positions to allow for quantitative determination of critical physiological information such as diffusive fluxes [10, 13, 54, 65], uptake/release kinetics [66–68], influence radii [57, 69] and local concentration dependencies [14, 65]. Obtaining information about the sink/source dictates that the sensing positions must be within the transient spatial scale (also known as depletion/accumulation width) of the dynamic gradient. In the context of gradient measurements, the relevant spatial and temporal quantities are the spatial range, defined as the distance between the nearest and farthest measurement positions with respect to the source/sink; the spatial resolution, defined as the distance between each measurement position; the sampling time, defined as the time interval between data points; and the measurement time, defined as the time it takes to obtain quantitative concentration information over the

entire spatial range. In general, the shortest transient gradient that can be measured is limited by the measurement time.

Techniques such as the vibrating probe self-referencing technique (SRT) [7–13] have been employed to measure biomolecule gradient/flux from cell surfaces using a single biosensor oscillating between two sensing positions separated by a fixed distance (Fig. 3.1). While SRT techniques can obtain data over reasonably large spatial ranges, the measurement time is much longer than the sampling time due to the restrictions on tip velocity to avoid stirring and the required number of oscillations for lock-in detection [9–13]. Acquisition of gradient information at multiple spatial locations requires multiple measurements, typically over tens of seconds, even with rapid sampling times (μs or ms scale) and high spatial resolution (nm scale). Techniques such as scanning electrochemical microscopy (SECM) also have high spatial resolution (nm scale) and short sampling times (μs or ms scale) [2–6]; however, in the context of gradient measurements, the multi-point measurements also result in relatively large measurement times due to the restrictions on scan rate (typically 8-25 μm s^{-1}) [2,14] in order to avoid disruption of the gradient via induced convection [2,17]. Moreover, optical techniques involving a fluorescent dye that binds to the analyte of interest have been employed to make concentration sampling over the entire reaction volume. While optical techniques have been used to image a concentration gradient of an electroactive fluorescent molecule near a 2D sink electrode [70], such techniques have not been extended to analytes of biological interest. The lack of reversible optical probes for analytes of biological significance like hydrogen peroxide has been identified as a limiting factor in extracellular measurements [71].

Individually addressed microelectrode arrays (MEAs) provide customizable spatial range and short measurement times by simultaneously measuring at multiple sensor electrodes. Amperometric MEAs have been used to demonstrate real time imaging of various non-physiological transient gradients that were set up by injecting or flowing highly-concentrated solutions (10-1000 mM) within or near a 2D MEA [33,35–37,39]. Amperometric MEAs have also been used for purposes other than gradient measure-

ments, e.g., detection of exocytotic release from both single cells [40, 41] and clusters of cells scattered on the MEA surface [42–46, 48]. To date, MEAs have not been widely used to study concentration profiles/gradients in the vicinity of 2D cell cultures or other common culture geometries. Even in measurements involving artificial (non-physiological) gradients, many reports present raw current data or rise times rather than absolute concentration values, thereby preventing the quantification of gradients. Several factors are believed to limit the ability to quantify gradient information. First, the MEA substrate geometry and packaging typically are not optimized for positioning the electrodes along a gradient field in proximity to a 2D cell culture or artificial analog thereof. Second, sensitivity variability hinders the determination of absolute concentrations at multiple electrodes with sufficient accuracy. Sensitivity variability in the forms of "response variability" (when sensitivity changes from experiment to experiment) and "sensitivity drift" (when sensitivity changes during the time course of an experiment) are inherent to amperometric sensing [26,27,43,45,50]. Additionally, MEAs exhibit "electrode variability", i.e., sensitivity changes among electrodes in the array. Evidence from the literature indicates that typical values of "electrode variability" [33, 36, 37, 39, 42–44] and "response variability" [37, 38, 47] are between 10-20%. Although "sensitivity drift" is common in the literature of single electrodes [26,27,50], data in previous MEA reports show clear evidence of sensitivity drift [42, 43, 45]. As the background concentrations become smaller (e.g., < 1 mM), the three categories of sensitivity variability make it difficult to determine concentrations at multiple electrodes with sufficient accuracy to calculate gradients based on concentration differences (ΔC) between pairs of adjacent electrodes.

This study showcases the quantitative measurement of transient gradients using amperometric 1D MEAs and in-situ transient calibration. The MEAs were designed in a geometry suitable for measurements of gradients in conventional 2D cell culture setups. The proposed in-situ transient calibration minimizes the aforementioned effects of sensitivity variability via the in-situ acquisition of sensitivity factors for each electrode in the array just prior to capturing the transient of interest. This approach

to measuring gradients could be considered a hybrid between SRT and traditional 2D MEAs, allowing acquisition of quantitative gradient information at multiple locations with measurement times significantly faster than typical SRT approaches (Fig. 3.1). A planar large sink electrode (LSE) is used to controllably induce dynamic gradients of hydrogen peroxide (H_2O_2) by consuming H_2O_2 upon excitation (Fig. 3.2). This LSE geometry mimics a 2D cell assembly, e.g., a monolayer of astrocytes [61, 62], endothelial cells [63] or bacteria [14], consuming H_2O_2 from the surroundings. Transients/gradients generated by the LSE were characterized experimentally, and the reliability of the measurements was assessed by comparing experimental and numerical data via normalized time analysis. In contrast to previous MEA reports, the current study focuses on gradients that are characterized by smaller background concentration scales (20 μM to 1 mM), short to long transients (150 ms-1000 s), and most importantly, small local concentration differences (ΔC down to sub-μM scale). Finally, the application of the approach to a physiological system is demonstrated by measuring H_2O_2 concentration transients near a 2D cell culture of human astrocytes and determining the associated gradients.

3.3 Materials and methods

3.3.1 Reagents

Hydrogen peroxide 30% (w/w) was purchased from Alfa Aesar (Ward Hill, MA) and phosphate buffer saline (PBS) pH 7.4 was purchased from Sigma-Aldrich (St. Louis, MO). All H_2O_2 solutions were prepared with 0.01 M PBS in ultrapure water. Human cerebral cortex astrocytes, astrocyte medium, cell freezing medium and 10 mg/ml poly-L-lysine were purchased from ScienCell Research Laboratories (Carlsbad, CA). Astrocyte medium contained 500 ml of basal medium, 10 ml of fetal bovine serum (FBS, Cat. No. 0010), 5 ml of astrocyte growth supplement (AGS, Cat. No. 1852) and 5 ml of penicillin/streptomycin solution (P/S, Cat. No. 0503). Glu-

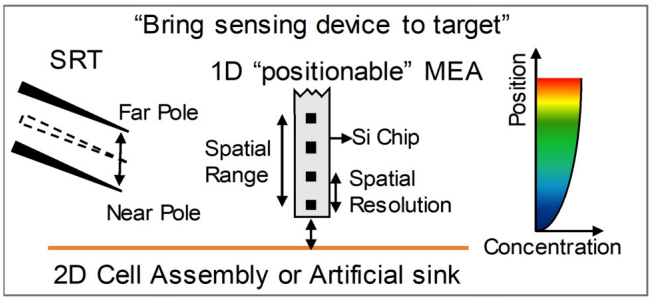

Fig. 3.1. **Analyte sink induces a concentration profile (rainbow colored) where concentration increases with position with respect to the sink. A positionable MEA (1D in this work) interrogates simultaneously all the electrodes within a desired spatial range every 10 ms, thus yielding a measurement time suitable for quantifying gradients induced by sub-second events in a "single-shot" measurement.** Vibrating probe techniques like SRT (left) acquire gradient information at a single spatial location by oscillating the probe tip between near and far poles. Even at a single spatial location, measurement times are typically much greater than sampling time due to restricted oscillation frequency (typically less than 1 Hz), required to keep the tip velocity below the level that disrupts the gradient of interest, and due to the need for measurements over multiple oscillation periods. The use of an MEA with appropriate electrode size and spatial range, along with in-situ calibration approach, allows measurements of concentration transients at various electrode locations, and determination of local gradients/fluxes near artificial or physiological (e.g. common 2D cell/tissue culture geometries) planar sinks of analytes.

cose solution (50 ml of 200 g/L) and 4-well chambered cover glass systems with 1.0 borosilicate glass were purchased from Thermo Fisher Scientific (Waltham, MA).

3.3.2 MEA design and fabrication

For the non-physiological measurements, the MEA consists of a 1D array of three electrodes (5 μm $\times$ 5 μm) with inter-electrode separation of 35 μm center-to-center (or 30 μm edge-to-edge). Electrodes are located very close (30 μm) to the bottom edge of the silicon die, and designated E1, E2 and E3, where E1 is the electrode closest

to the edge. Fig. S-1 in Supplementary Material shows the details of the MEA design and fabrication process. For the physiological measurements, the MEA consists of a 1D array of five electrodes (10 μm $\times$ 10 μm) with inter-electrode separation of 140 μm center-to-center, which allows for measurements over a larger spatial range of the concentration profile ($\sim$600 μm).

3.3.3 Apparatus

Multiple potentiostats (Reference 600, Gamry Instruments Inc., Warminster, PA) were employed to individually bias the electrodes in the array and the LSE; the latter consisted of a platinum disk electrode (1.6 mm diameter). Platinum wire and disk (0.5 mm and 1.6 mm diameter, respectively) were used as counter electrodes; the wire was shared among the sensing electrodes in the array, while the disk was the auxiliary for the LSE. Two Ag/AgCl (sat'd 3M NaCl) reference electrodes were used; the sensing electrodes in the array shared a single reference electrode. Both the counter electrodes, LSE and reference electrodes were purchased from BASI Inc. (West Lafayette, IN). For the measurements with cultured human astrocytes, only the sensing electrodes in the MEA were used. Unless stated otherwise, all potentials are referred to the Ag/AgCl (sat'd 3M NaCl) reference electrode, and all experiments were performed at room temperature.

3.3.4 MEA characterization

Cyclic voltammetry of 0.5 mM H_2O_2 in 0.01 M phosphate buffered saline was used to characterize the oxidation peak of H_2O_2 at Pt surface, which was found to be 0.5 V. For initial characterization, the amperometric response of the electrodes to concentrations ranging from 0 to 1.2 mM H_2O_2 were recorded by immersing the MEA chip in various unstirred H_2O_2 solutions (6 mL) followed by biasing the electrodes at 0.5 V. The obtained data were used to evaluate linearity, transient sensitivities, and electrode-to-electrode variabilities. For all concentration transient/gradient measure-

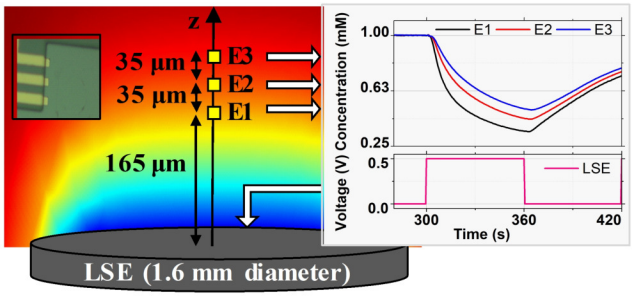

Fig. 3.2. **Schematic of experimental setup, not drawn to scale. Large sink electrode (LSE) controllably generates a concentration field (indicated by color scale) with associated gradients as a function of time and position, and in response to a potential of 0.5 V applied between 300-360 s (see inset). This diffusion-reaction system emulates a 2D assembly of cells consuming analyte from the surroundings, and constitutes the benchmark to evaluate the performance of the microelectrode array (MEA) as a reliable tool for measurement of physiological gradients.** Platinum microelectrodes E1, E2 and E3 (5 μm $\times$ 5 μm each) in the MEA are one-dimensionally arranged with inter-electrode separation of 35 μm (center-to-center). MEA packaging allowed positioning of E1 at 165 μm from the LSE. These microelectrodes record changes in local concentration at positions 165, 200, and 235 μm with respect to the LSE via amperometric signals, which are later converted into concentration data. The spatial dependence of the concentration field dictates that concentration increases with distance from LSE. Left inset shows photograph of the three microelectrodes in the MEA. Right inset shows concentration transients obtained simultaneously from the three microelectrodes in response to a potential of 0.5 V applied to the LSE between 300-360 s followed by a recovery interval from 360-420 s. The concentration was uniform and constant at 1 mM before 300 s. The spatial dependence of the concentration field dictates that concentration increases with distance from LSE, as indicated by the order E1 $<$ E2 $<$ E3 in the concentration amplitudes. This systematic behavior indicates that each microelectrode records the concentration transient locally.

ments, the electrodes were calibrated via in situ transient calibration procedure, as described in Section 3.3.6.

3.3.5 Geometry for transient and gradient measurements with LSE

The silicon chip with the MEA was manually brought into proximity to the LSE surface (Fig. 3.2) such that the three sensor electrodes were aligned perpendicular to the surface of the LSE and centered within the area of the LSE. Using optical microscopy, the distances z_i between the LSE surface and the center of each electrode E_i (i = 1, 2, 3) were found to be $z_1 \approx 165$ μm, $z_2 \approx 200$ μm and $z_3 \approx 235$ μm (Fig. 3.2). Once the chip was placed in position, all the experiments were run in sequence without movement of the chip with respect to the LSE. A Petri dish containing 6 mL 0.01M phosphate buffer saline with uniform concentration of 1 mM H_2O_2 was used throughout the measurements.

3.3.6 In situ transient calibration and measurement of transient concentrations and their gradients

With the MEA chip positioned as described in Section 3.3.5, the three MEA electrodes were biased at 0.5 V starting from t = 0 s and throughout the course of an experiment. Every electrode i in the array provides a current $I_i(t)$ due to the time-dependent local concentration at the position z_i perpendicular to the LSE surface. No bias was applied to the LSE during the first 300 s, such that the amperometric data corresponded to the electrode responses to the uniform concentration of 1 mM H_2O_2. Taken together, the known H_2O_2 concentration (C_0 = 1 mM) and the electrode currents at t = 300 s (called I_{300}) were subsequently used to convert $I_i(t)$ from each electrode into a spatially-resolved concentration vs. time, namely $C_i = C(z_i, t) = (C_0/I_{300})_i \times I_i(t)$, where $(C_0/I_{300})_i$ is the sensitivity factor for electrode i. This procedure is denoted âĂIJin situ transient calibrationâĂİ. The settling time of 300 seconds was chosen to reduce the sensitivity drift to a level (1.7% min^{-1}) that allows measurement of transient response over several minutes, as determined by a separate experiment involving monitoring of the electrode sensitivities over approximately 2000 seconds.

Immediately after, starting at t = 300 s, time-dependent gradients were generated electrochemically by applying a sequence of four potential pulses to the LSE, consisting of voltages of 0.5 V during the interval t_{uptake} and open circuit potential during the interval $t_{recovery}$; hence, the pulse period was $t_{pulse} = t_{uptake} + t_{recovery}$. The interval t_{uptake} was set at 0.15, 1, 10 or 60 s for a given experiment, and the time $t_{recovery}$ was kept constant at 60 s for all the experiments. The local time-dependent gradient was calculated as $G_{i+1,i} = (C_{i+1} - C_i)/\Delta z$, where Δz is the distance between z_i and z_{i+1} in the direction perpendicular to the LSE surface. The $G_{i+1,i}$ is associated with the position at half the distance between z_i and z_{i+1}. From this result, the diffusive flux $J_{i+1,i}$ is calculated by invoking Fick's second law as $J_{i+1,i}$ = -D $G_{i+1,i}$, assuming that the H_2O_2 diffusion coefficient D is 1.71×10^{-5} cm^2 s^{-1} [72]. This methodology is a logical extension of the self-referencing technique (SRT), which has shown that the numerical value of $G_{i+1,i}$ is a good approximation to the actual local gradient as long as Δz is small enough to ensure the linearity of the gradient between z_i and z_{i+1} [7, 10]. Typically, gradient measurements using SRT have been performed with $\Delta z \sim 30$ μm [9–13].

3.3.7 Numerical model

Numerical solution of a diffusion-reaction model was performed using Comsol Multiphysics to resolve the spatio-temporal changes in the concentration profile as a function of the potential pulses applied to the LSE. Due to the cylindrical symmetry of the problem, the geometry of the Petri dish corresponds to the volume enclosed by r = 20 mm and $0 \leq z \leq 10$ mm, and the geometry of the circular LSE corresponds to the surface enclosed by r = 0.8 mm at z = 0. Therefore, a two-dimensional solution of the diffusion equation in cylindrical coordinates with surface reactions occurring at both the LSE and the sensing electrodes was sufficient to resolve the physics of the problem. The diffusion coefficient of H_2O_2, 1.71×10^{-5} cm^2 s^{-1}, was obtained from

the literature [72], and the heterogeneous reaction rate constant (k_F) of the LSE was adjusted to fit the experimental data.

3.3.8 Cell culture

Human cerebral cortex astrocytes were obtained from Sciencell (Carlsbad, CA) cryopreserved at passage one. Astrocytes were expanded and maintained per the company's protocol. For each experiment, passage three astrocytes (5.0×10^4 cells cm^{-2}) were seeded onto poly-L-lysine-coated chambered cover glass system wells and incubated for two days in a humidified atmosphere containing 5% CO_2 at 37°C. Medium was replaced with fresh astrocyte medium one day after seeding. Cells were used for gradient measurements after two days of incubation. Prior to the gradient measurements, the cultures were washed twice with PBS (pH 7.4), and then 0.3 mL of 5.5 mM glucose in PBS was added to culture well.

3.3.9 Geometry and timeline for transient and gradient measurements with cultured human astrocytes

For the physiological experiments, a MEA with different dimensions (10 μm $\times$ 10 μm electrodes with a 140 μm pitch) was used to enable measurements over the temporal and spatial ranges of interest for H_2O_2 consumption by the cells. In addition, an alternative approach for establishing the starting time for H_2O_2 consumption and performing in-situ transient calibration was developed, as follows. The MEA was initially positioned over the cell culture, such that the bottom of the chip was 5 mm from the cell surface. Initially, the cell culture contained 0.3 mL of 5.5 mM glucose in PBS. At t = 0 s, 1.2 mL of solution containing 25 μM H_2O_2 and 5.5 mM glucose in PBS was added to obtain 1.5 mL of solution with final concentrations of 20 μM H_2O_2 and 5.5 mM glucose in PBS. At t = 30 s, the five electrodes in the MEA were simultaneously biased at 0.5 V; this bias was maintained throughout the course of the experiment. The amperometric response was allowed to settle for 300 s; then the current at each

electrode at t = 330 s was used to determine the in-situ sensitivity factor for that electrode. Based on modeling of the diffusion profile using the inferred consumption rate of peroxide (and confirmed by the experimental results), the diffusion profile has not yet reached the position of the MEA electrodes at t = 330 s, so the concentration at the location of the MEA is the background concentration of 20 μM. Just after the measurement at t = 330 s, the MEA was moved using a XYZ micro-positioner to a position such that the distances z_i between the cell culture surface and the center of each electrode E_i (i = 1, 2, 3, 4, 5) were $z_1 \approx 60$ μm, $z_2 \approx 200$ μm, $z_3 \approx 340$ μm, $z_4 \approx 480$ μm and $z_5 \approx 620$ μm. The transient measurements started immediately thereafter, and the current at each electrode was converted into a concentration using the corresponding in-situ sensitivity factor. Concentration measurements at all five electrodes were obtained in a single measurement run, and gradients were calculated at each time point from the corresponding concentration values, without smoothing or multi-point averaging.

3.4 Results and Discussion

3.4.1 MEA device characterization

Amperograms of ultramicroelectrodes typically exhibit an initial transient response (settling time) before achieving steady state, and conventional calibration methods use the values of steady state current to extract sensitivities. In our experiments, the amperograms of the electrodes biased at 0.5 V were monitored for 2000 s without observing steady state currents (Fig. S-2 in Supplementary Material). This effect, interpreted as a drift in sensitivity and observed in other MEA [43, 45] and single-electrode [26, 27, 50] studies, precluded the extraction of conventional steady state sensitivities. Alternatively, sensitivity was obtained by plotting the current measured at t = 300 s (called I_{300}) vs. the concentration present in the solution (0, 0.2, 0.4, 0.8 and 1.2 mM H_2O_2), for each electrode in the array (Fig. S-3 in Supplementary Material). This time point (t = 300 s) was chosen to provide a good

trade-off between settling time and average rate of sensitivity drift, which was found to be 1.7% min^{-1} (see discussion of Fig. S-2 in Supplementary Material). The data of I_{300} vs. concentration (shown in Fig. S-3 in Supplementary Material) were used to assess linearity and to determine sensitivity (called S_{300} as it is associated to I_{300}) and limit of detection for each electrode. Linear fitting provided S_{300} values of 2.07 ± 0.11, 1.44 ± 0.05 and 1.47 ± 0.06 nA mM^{-1} (mean ± standard error, n = 3) for E1, E2 and E3, respectively, and the corresponding R-square values were always above 0.99, indicating that the three electrodes in the array are linear over the range of interest (0-1.2 mM). The average sensitivity ± standard deviation was 1.65 ± 0.36 nA mM^{-1}, yielding electrode variability of 21.8%, whereas the response variability from triplicate experiments was found to be 2.5%. In order to avoid the need for selectivity, the experiments were performed with media containing only H_2O_2 and buffered inert electrolyte (phosphate buffer saline), as has been common in prior reports [62, 64, 65, 73–77]. However, our approach can be applied to the sensing of other analytes and can incorporate typical approaches for achieving selectivity through enzymatic and nanostructured functionalizations [9–13, 51, 78–81].

3.4.2 In situ transient calibration

Characterization of the MEA indicates that the electrode variability (21.8%) and the response variability (2.5%) are large enough to prevent accurate determination of dynamic gradients based on concentrations quantified by the traditional MEA calibration (see Supplementary Material for a description of the traditional MEA calibration). Therefore, in situ transient calibrations were performed, as described in Section 3.3.6, to obtain calibration factors immediately prior to applying a potential pulse waveform or prior to approaching the chip to the cell surface. The in situ transient calibration minimizes both response variability and sensitivity drift by obtaining a calibration factor for every experiment "in situ" just prior to the generation of the gradient of interest, and minimizes electrode variability by performing an individ-

ual calibration of each electrode in the MEA. This approach could be viewed as a multi-electrode version of in situ calibration approaches previously used to interpret single electrode experiments [2, 65]. Like the conventional single point calibration, the in situ transient calibration relies on response linearity and negligible offset, as established by the data of I_{300} vs. concentration, and works well for concentration transients that change more rapidly than the sensitivity drift rate (see discussion of Fig. S-2 in Supplementary Material).

3.4.3 Spatio-temporal resolution of transient concentrations using the MEA

Fig. 3.2 shows the schematic diagram of a diffusion-reaction system constituted by an LSE surrounded by H_2O_2 solution. This system was used to controllably generate transient gradients by applying potential pulse waveforms to the LSE, and the generated gradients were measured by the MEA. A potential pulse waveform comprises four pulses, and each pulse consists of an interval (t_{uptake}) with potential at 0.5 V followed by an interval ($t_{recovery}$) at open circuit potential. During the interval t_{uptake}, the LSE electro-oxidizes (i.e., consumes) H_2O_2 causing a depletion in concentration. During the interval $t_{recovery}$, the depleted solution adjacent to the LSE recovers progressively toward the initial concentration due to diffusion from the bulk solution. Fig. 3.2 (right inset) shows the processes of depletion and recovery of the concentration near the LSE in response to a single pulse applied to the LSE. In this case, the background concentration is 1 mM, the pulse starts at t = 300 s and has t_{uptake} and $t_{recovery}$ equal to 60 s, and the concentrations at the positions of the electrodes display transient behaviors consistent with depletion and recovery. Similar results for a single pulse having t_{uptake} = 1 s and $t_{recovery}$ = 60 s in 20 μM background concentration are shown in Fig. S-4 in Supplementary Material. Note that other reports on gradient measurements using amperometric MEAs have worked with concentrations in the range of 10-1000 mM [33, 35–37, 39] whereas the expected

physiological concentrations of H_2O_2 are below 1 mM [82]. Since sensitivity variability is more detrimental at small concentrations, the above results indicate that MEA and in situ transient calibration, altogether, are effective at physiological concentrations.

Fig. 3.3A and 3.3C show the transient concentrations for potential pulse waves with t_{uptake} of 0.15 and 60 s. Corresponding results for pulse waves with t_{uptake} of 1 and 10 s are shown in Fig S-5 in Supplementary Material. In these four cases, $t_{recovery}$ is 60 s and the positions of the sensors with respect to the LSE are 165, 200, and 235 μm, as illustrated in Fig. 3.2. The systematic change in signal waveforms at various electrodes, and the order in the signal amplitudes (E1 < E2 < E3), indicate that each sensor captures the concentration dynamics locally, with spatial resolution given by the inter-electrode separation (35 μm).

Experimental curves in Fig. 3.3A and 3.3C agree well with the simulated curves shown in Fig. 3.3B and 3.3D, respectively. These results indicate that the intrinsic response time of each individual electrode is fast enough to resolve the transient concentrations arising from uptake events as short as 0.15 s. This ability to measure gradients caused by rapid (e.g., sub-second) uptake events in stagnant solution is a major advantage of MEAs over scanning probe techniques. The good agreement between experimental and numerical results also indicates that accurate quantification of concentration is possible via the in situ transient calibration, wherein the currents corresponding to a known background concentration (in this case, 1 mM) are measured for each electrode just prior to the onset of the uptake event. In contrast, the concentrations quantified via the traditional MEA calibration do not agree with the numerical predictions neither qualitatively nor quantitatively, as shown in Fig. S-6 (B and E) in Supplementary Material.

Altogether, the above results differ from other amperometric MEA reports in various aspects. First, all the measured transients are due to diffusion, as the solution is stagnant, whereas in other reports the transients are due to flow or injection of analyte [35–37, 39]. Second, all the measurements are performed in the direction perpendicular to the active surface. This geometry is consistent with the direction

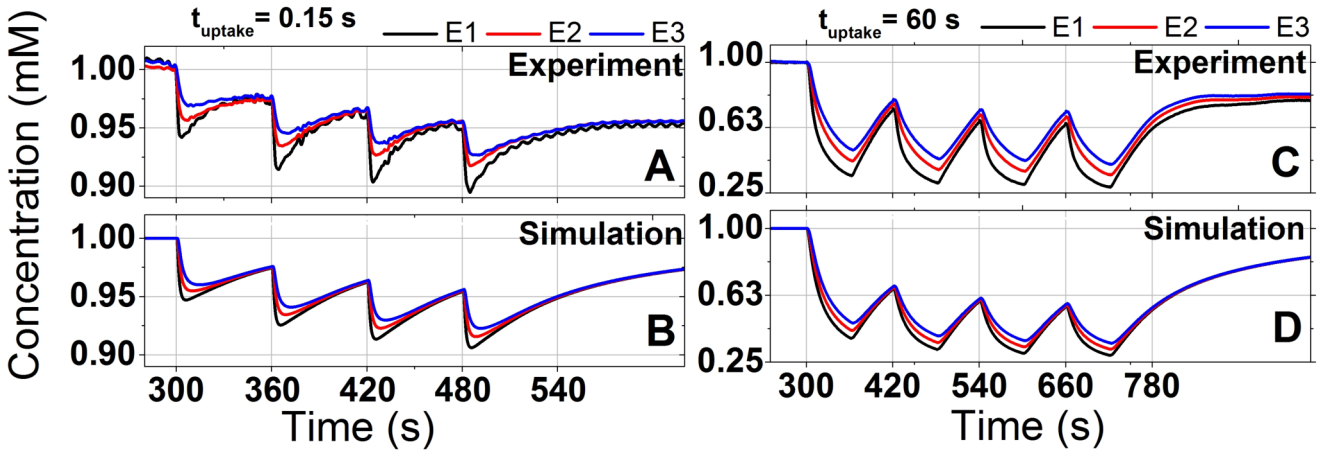

Fig. 3.3. **Simultaneous concentration measurements were obtained at multiple electrodes, thus capturing transients induced by the LSE in response to uptake intervals as short as 0.15 s (left). Experimental curves (A, C) agree well with corresponding numerical simulation results (B, D) over most of the temporal scale of the experiments.** The plotted curves indicate concentrations measured at electrodes E1 (165 μm), E2 (200 μm) and E3 (235 μm) in response to potential pulse waves applied to the LSE, starting at t = 300 s. Each wave comprises four pulses, and each pulse has duration $t_{pulse} = t_{uptake} + t_{recovery}$, with $t_{recovery} = 60$ s for all the pulse waves. (A, B) $t_{uptake} = 0.15$ s, (C, D) $t_{uptake} = 60$ s. The concentration was uniform and constant at 1 mM before 300 s.

of mass transport in 2D adherent cell cultures [13]. Third, the signals are quantified in absolute concentration scale. Absolute concentration values allow for quantitative determination of critical physiological information such as diffusive fluxes [10, 13, 54, 65], uptake/release kinetics [66–68], influence radii [57, 69] and local concentration dependencies [14, 65]. Fourth, the experiments addressed measurements of uptake intervals as short as 150 ms, thus paving the way toward the study of rapid transient gradients in, for instance, in vitro cell networks [13, 83].

3.4.4 Dynamic gradients and fluxes of hydrogen peroxide

Transient gradients were obtained by calculating the difference in the measured transient concentrations between pairs of adjacent electrodes, as described in Section 2.6. Fig. 3.4 shows the transient gradients for potential pulse waves with t_{uptake} of 0.15 and 60 s. Corresponding results for pulse waves with t_{uptake} of 1 and 10 s are shown in Fig. S-7 in Supplementary Material. The peak of the gradient inferred from the concentration difference between E1 and E2 is larger than that inferred from E2 and E3, as expected from the relative positions with respect to the LSE. The gradients are presented here in units of μM μm^{-1}, which are particularly useful for intuitive understanding of physiological scenarios; other relevant units such as mol cm^{-4} can be obtained using appropriate conversion factors. Using diffusion coefficients from the literature, the calculated gradients can be converted to diffusive fluxes, with peak amplitudes in the range of 34-625 pmol cm^{-2} s^{-1}. Fluxes exhibiting peak amplitudes in the range of 2-5 pmol cm^{-2} s^{-1} were also measured for background concentration of 20 μM (Fig. S-4 in Supplementary Material). These experimental results are in the same order of magnitude as reported physiological measurements. For instance, data from literature allows to calculate an average H_2O_2 influx of 29 pmol cm^{-2} s^{-1} for a monolayer of human breast cancer cells (MDA-MB-231, 2.1×10^5 cells distributed on a circular surface of 6.35 mm diameter) [62], and other report quoted H_2O_2 influx of 10 pmol cm^{-2} s^{-1} for bacteria biofilm. [14] These gradient measurements illustrate the potential of the MEA as an analytical tool for physiological studies.

3.4.5 Numerical Simulation

Calculation of transient gradients requires reliable measurements of transient concentrations. The reliability of the measurements was assessed via predictions based on the well-known diffusion-reaction model [50, 84–88], which allows for computation of the local concentration profile as well as the corresponding transient concentrations at the positions of the sensor electrodes. The diffusion-reaction model sets the

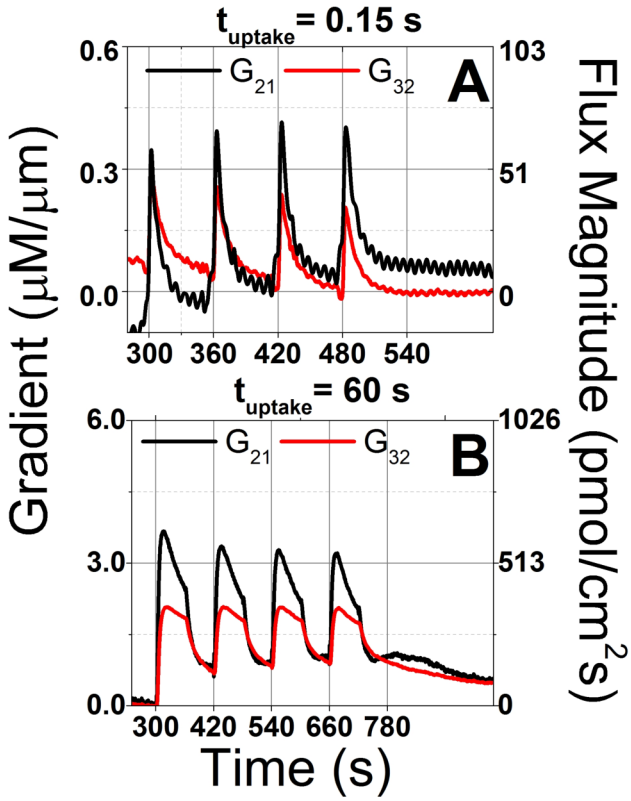

Fig. 3.4. **Reliable concentration data from multiple electrodes allow for determination of transient gradients based on the concentration differences between pairs of adjacent electrodes. In situ transient calibration provides the required reliability by reducing the effects of sensitivity variability.** The plotted curves indicate the gradients obtained from computation of the concentration difference between E1−E2 (G_{21}), and E2−E3 (G_{32}) in response to potential pulse waves applied to the LSE. (A) t_{uptake} = 0.15 s, (B) t_{uptake} = 60 s. For all pulse waves, $t_{recovery}$ = 60 s. Corresponding diffusive flux magnitudes can be read from the right scale axis. Peak diffusive flux magnitudes are in the range of 34-625 pmol cm^{-2} s^{-1}. These experimental results are in the same order of magnitude as reported physiological measurements.

reaction flux occurring at the active surface (in this case, the LSE surface) to be proportional to the local concentration, with proportionality constant k_F (also known as heterogeneous reaction rate constant). As previously shown in Fig. 3.3, the simulated curves (panels B and D) agree qualitatively and quantitatively with the corresponding experimental curves (panels A and C) when k_F is set at 10^{-2} cm s^{-1}, thus indicating that explicit information about the active surface can be obtained by fitting the simulation to the experimental data. This strategy to obtain information about the active surface has been discussed theoretically [54].

The overall behavior within a pulse wave can be understood by considering Fig. 3.5, which presents simulated concentration profiles for t_{uptake} of 60 and 0.15 s. Each curve corresponds to a specific time point within the pulse waveform, as indicated by symbols in the corresponding insets, and the shaded bands represent the distance range (150-250 μm) wherein the electrodes were located during the experiments. When the LSE is biased at 0.5 V (uptake intervals), the electro-oxidation of H_2O_2 takes place at the LSE surface with a high rate constant k_F, so the concentration near the LSE becomes depleted. When the LSE is left at open circuit potential (recovery intervals), negligible electro-oxidation reaction occurs at the LSE surface, and the concentration near the LSE recovers progressively toward initial concentration due to diffusion from the bulk solution. The profile recovery is only partial for all the recovery intervals, i.e., the concentration profile never recovers the initial functional form (indicated by curves in black-filled symbols). Consequently, deeper diffusion profiles are induced pulse after pulse. This behavior indicates that, for the diffusion-reaction system studied here, each potential pulse within the studied pulse waves yields a unique concentration profile. Accordingly, the concentrations at the positions of the electrodes (i.e., within the shaded bands in Fig. 3.5) exhibit a decreasing trend from one pulse to another. This trend is captured quantitatively by the MEA, as shown in Section 3.4.3. To better assist the comprehension of spatiotemporal propagation of uptake events occurring at the LSE surface, simulated 3D plots of concentration as

a function of time and distance from the LSE, and in response to single pulses with t_{uptake} of 60 and 0.15 s, are shown in Figure S-8 in Supplementary Material.

3.4.6 Diffusional Distortion and Normalized Time Analysis of Spatial and Temporal Response

Although consumption of H_2O_2 at the LSE starts immediately after the voltage pulse is applied, the corresponding depletion of analyte at the location of the MEA electrodes does not happen instantaneously. Therefore, extracting information about the events occurring at the active surface requires an approach to account for the delay time t_0 caused by diffusion between the LSE surface and the electrode locations. This phenomenon, known as diffusional distortion [89], is used here to interpret the time-dependent measurements obtained at known distances from the LSE. Note that the delay time t_0 is a position-dependent quantity and is an inherent characteristic of diffusion-reaction systems. It should not be mistaken for the response time of the electrodes in the MEA.

The analytical expression for the measured transient concentrations has the general functional form $C/C_0 = f(t_{uptake}, t_{recovery}, D, z, t)$, where C_0 is the initial background concentration, D is the diffusion coefficient, z is the position with respect to the active surface, t is the time, and t_{uptake} and $t_{recovery}$ are the uptake and recovery intervals, as defined previously. t_{uptake} and $t_{recovery}$ are controllable parameters for excitation of the active surface. Fickian diffusion is such that, for an infinitely long uptake interval (i.e., $t_{uptake} \rightarrow \infty$, $t_{recovery} \rightarrow 0$), the general functional form boils down to $C/C_0 = f(D, z, t)$. This expression can be written in terms of the delay time t_0 as $C/C_0 = f(t/t_0)$ because D, z and t are interrelated when the mass transport is due to Fickian diffusion. Therefore, for a given D, t_0 is the time required for the ratio C/C_0 at position z to reach a given value. For instance, in the present analysis t_0 is the time at which $C/C_0 = 0.7$ at the sensor positions, where the value of 0.7 corresponds approximately to the condition at which $t_0 = {z_i}^2/2D$, with z_i being the

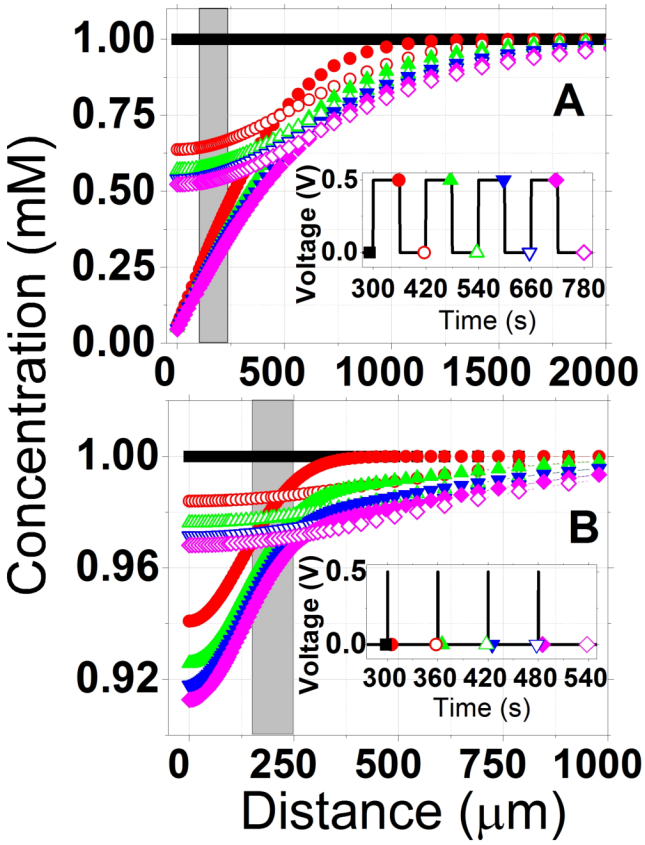

Fig. 3.5. **Simulated concentration profiles were obtained for various time points during the potential pulse waves applied to the LSE. Each pulse wave comprises four pulses. Despite being identical, the pulses yield concentration profiles that differ quantitatively from one pulse to another, due to partial recovery of the concentration profile before starting a new pulse.** Plotted curves indicate simulated concentration profiles as functions of distance along the z-axis (LSE is at z = 0) and for various time points indicated by symbols in the insets. Curves in the insets indicate potential pulse waves ($t_{pulse} = t_{uptake} + t_{recovery}$) applied to the LSE with (A) $t_{uptake} = 60$ s and (B) $t_{uptake} = 0.15$ s. In both cases $t_{recovery} = 60$ s. Shaded bands (150 μm < z < 250 μm) indicate the regions occupied by the electrodes during the experiments. Since $t_{recovery}$ is the same for all pulse waves, the numerical results indicate that t_{uptake} is responsible for the magnitude of concentration change at the electrode positions during each uptake interval, and is also responsible for the transient spatial scale of the corresponding concentration fields.

position of electrode i. Details on this derivation are provided in the Supplementary Material (Fig. S-9).

The delay time t_0 allows to write the general abovementioned expression for the measured transient concentrations in terms of normalized times, i.e., $C/C_0 = f(t_{uptake}/t_0,\ t_{recovery}/t_0,\ t/t_0)$. This normalization allows for direct comparison between concentrations measured experimentally and concentrations obtained from simulations, without requiring experimental determination of the exact values for sensor positions and diffusion coefficient. To perform the reliability assessment, both experimental and simulated data must be normalized to the corresponding values of t_0. Experimental data for t_{uptake} of 60 s provided t_0 values of 12, 18 and 25 s for E1, E2 and E3, respectively. Similarly, t_0 values from simulated data were obtained by simulating the transient concentrations measured by electrodes at positions 165, 200, and 235 μm with respect to the LSE, in response to a pulse with t_{uptake} of 100 s, and then extracting the time at which $C/C_0 = 0.7$. Experimental data in Fig. S-9 shows that electrode positioned closer to the LSE (40, 65 and 90 μm) result in smaller values of t_0 (0.5, 1.5, and 2.5 s).

Fig. 3.6 shows the concentration minima $C_{min,i}$ (normalized to initial background concentration C_0) as a function of t_{uptake}/t_0, for the four studied pulse waves, and from both experimental and simulated data. $C_{min,i}$ indicates the concentration minimum associated to the i-th pulse in a pulse wave (see naming conventions in Fig. S-10 in Supplementary Material). A maximum difference of 7% relative to full concentration scale (i.e., relative to C_0) is observed between experimental and simulated results, thus quantifying the ability of the MEA to resolve the signal minima for successive pulses. It is important to note, first, that this result was obtained despite the electrode variability (21.8%) and response variability (2.5%) observed in our experiments, and second, that other works in the literature have reported similar variabilities for MEAs [33,36,37,39,42–44]. These observations indicate that the in situ transient calibration is crucial to minimize the effects of sensitivity variability.

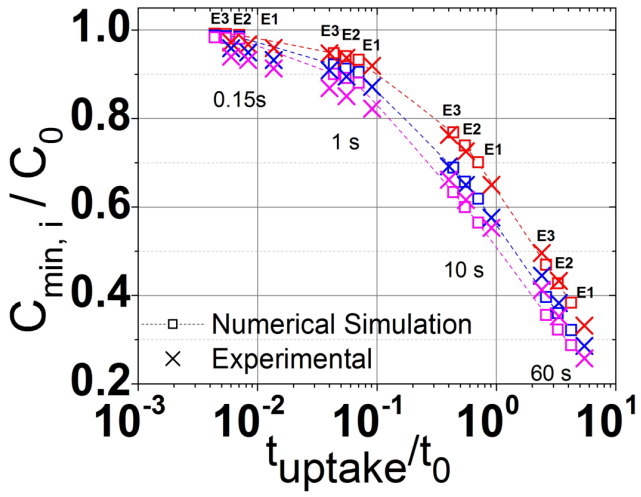

Fig. 3.6. **Concentration minima (normalized to C_0) associated to the i-th pulse in a pulse wave are plotted as a function of t_{uptake}/t_0, for the four studied pulse waves, and from both experimental and simulated data. Normalization of the uptake interval t_{uptake} by the characteristic delay time t_0 associated to each electrode position allows for direct comparison between experimental and simulated data independently of diffusion coefficient and electrode positions. Experimental and simulated data agree quantitatively within a maximum difference of 7% relative to full concentration scale.** Red: pulse i = 1, blue: pulse i = 2, pink: pulse i = 4. C_0 is the initial background concentration, and pulse i = 3 has been omitted for clarity. Each group of points corresponds to data for the three electrodes (E1, E2, and E3) and for the indicated t_{uptake} values (0.15, 1, 10 and 60 s). Normalization of t_{uptake} by t_0 spreads and arrange the data points in the order E3, E2 and E1 from left to right in each group, consistent with t_{uptake}/t_0 being smaller for electrodes located farther from the LSE. Line connecting numerical simulation points is a guide to the eye.

Fig. 3.7 shows the concentrations (normalized to C_0) at various stages of recovery (after the fourth pulse in a pulse wave) as a function of t_{uptake}/t_0, for the four studied pulse waves, and from both experimental and simulated data. The various stages of recovery are denoted by C_{R1}, C_{R2} and C_{Rf} (see Fig. S-10 in Supplementary Material), where C_{R1} is the concentration at the end of the fourth pulse, C_{R2} is the concentration after 60 s from C_{R1}, and C_{Rf} is the concentration after 200 s from C_{R1}. In this case, the difference between the experimental and simulated results is larger, particularly for later stages of the recovery, but without exceeding 15% relative to full concentration scale. For instance, in the case of $t_{uptake} = 60$ s the simulation predicts 90% of recovery, whereas the experiment exhibited 80%. In the initial stages of recovery (C_{R1} and C_{R2}), there is reasonable agreement between the experimental and simulation results. In general, the electrode response becomes saturated as it evolves from C_{R1} to C_{R2}, and finally to C_{Rf}. This effect is attributed to the signal drift in a uniform constant concentration, which is a phenomenon inherent to amperometric sensing, as observed in other reports [26, 27, 43, 45, 50]. It is important to note that this drift dominates only in conditions where the gradient of interest is either absent (i.e., in uniform constant concentration) or sluggish with respect to the signal drift rate (e.g., at later recovery stages). This observation indicates that quantitative measurements can be made with minimal errors in presence of a transient gradient that changes faster than the sensitivity drift rate.

3.4.7 Quantification of physiological gradient in 2D cell culture of human astrocytes

In-vitro demonstration of a physiological gradient takes advantage of the fact that 2D monolayers of astrocytes uptake H_2O_2 from the extracellular space [61, 62], thus setting up a concentration profile with associated gradients. Fig. 3.8 demonstrates the ability of the MEA to be positioned near the 2D cell culture and extract concentration transients at each electrode position when the cells are exposed to 20 μM H_2O_2. Due

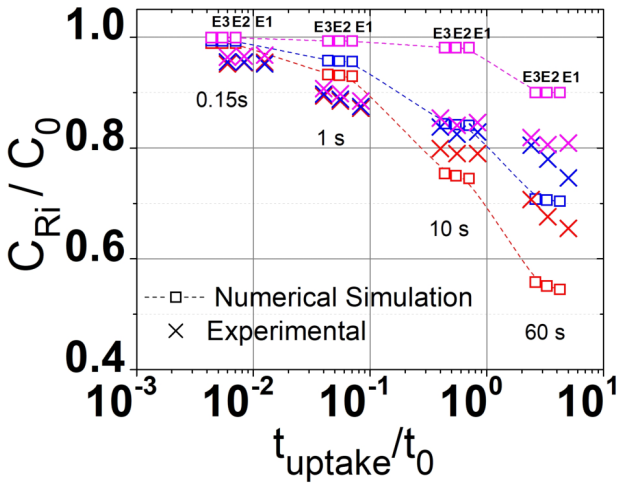

Fig. 3.7. **Concentrations (normalized to C_0) at three time points after the fourth pulse in a pulse wave are plotted as a function of t_{uptake}/t_0, for the four studied pulse waves, and from both experimental and simulated data. Experimental and simulated data agree quantitatively within a maximum difference of 15% (relative to full concentration scale) during the illustrated stages of recovery. This increase in the difference between data sets is explained in the main text in terms of sensitivity drift.** The illustrated stages of recovery are denoted by C_{Ri} (i = 1, 2, f), where C_{R1} (red) is the concentration at the end of the fourth pulse, C_{R2} (blue) is the concentration after 60 s from C_{R1}, and C_{Rf} (pink) is the concentration after 200 s from C_{R1}. These stages quantify the final recovery when the concentrations change from C_{R1} $\rightarrow$ C_{R2} $\rightarrow$ C_{Rf} at the electrode positions. Each group of points corresponds to data for the three electrodes (E1, E2, and E3) and for the indicated t_{uptake} values (0.15, 1, 10 and 60 s). Normalization of t_{uptake} by t_0 spreads and arrange the data points in the order E3, E2 and E1 from left to right in each group, consistent with t_{uptake}/t_0 being smaller for electrodes located farther from the LSE. Line connecting numerical simulation points is a guide to the eye.

to the non-availability of a stimulus to start the uptake, a modified in situ transient calibration is employed, consisting in locating the MEA at 5 mm from the cell surface (prior to t = 330 s) to extract the calibration factors of the electrodes, and then positioning the MEA near the cells (at t = 330 s) such that the electrodes end up located at 60, 200, 340, 480 and 620 μm from the cell surface (see Fig. 3.8A). Fig. 3.8C shows the transients extracted beyond 334 s (the motion of the MEA chip takes 4 s) and indicates the presence of a gradient of H_2O_2 set up by cellular uptake, such that the order in the concentration amplitudes is E1 < E2 < E3 < E4 < E5 at any time. Fig. 3.8D shows the gradients and fluxes calculated from the measured transient concentrations. The concentration transients in this figure, and the corresponding gradients, were determined from single measurement runs, without averaging or smoothing.

3.5 Conclusions

Sensitivity variability in amperometric sensing, and particularly in MEAs, has hindered the determination of local absolute concentrations with enough accuracy as to determine gradients based on concentration differences between closely spaced electrodes. This issue becomes worse at the smaller concentration scales found in physiological studies. In this work, we demonstrated quantitatively the measurement of transient gradients of H_2O_2 using MEAs and an active surface that controllably induces transient gradients upon excitation, and we evaluated the reliability of the measurements by comparing experimental and simulated data via normalized time analysis. The results of this analysis indicate that the in situ transient calibration, developed here, minimizes the effects of sensitivity variability to such an extent that accurate determination of local absolute concentrations is possible. Measurements demonstrated here include transient gradients caused by sub-second uptake events (using sampling time and measurement time of 10 ms, spatial range of 70 μm, and spatial resolution of 35 μm), and in vitro gradients caused by continuous H_2O_2 uptake

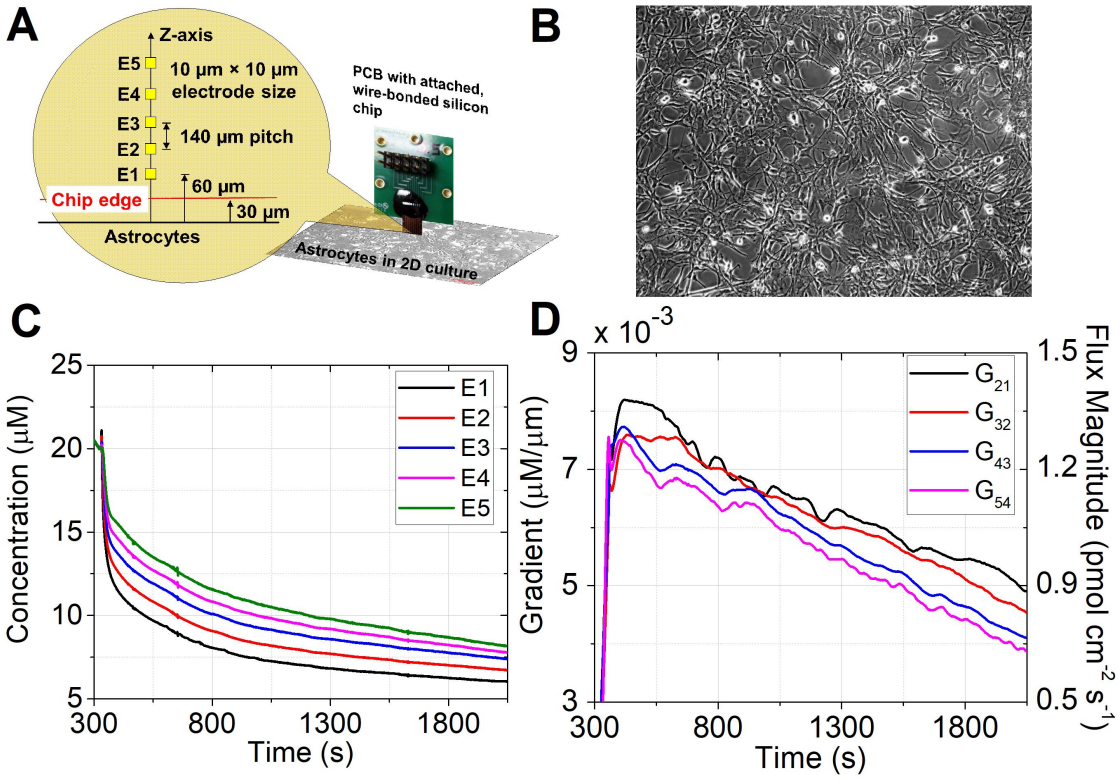

Fig. 3.8. **On exposure to 20 μM hydrogen peroxide (H_2O_2), adherent 2D cell culture of human astrocytes continuously consumes H_2O_2, setting up an extracellular concentration gradient which is quantified using on-chip MEA and in situ transient calibration.** (A) Setup for the experiment. MEA comprises five platinum electrodes labeled E1 through E5, which are positioned at 60, 200, 340, 480 and 620 μm from the cell surface, respectively, during the transient measurements (t > 330s). As described in the text, a modified in-situ transient calibration approach involved positioning the MEA at 5 mm from the cell surface during the time interval 0<t<330 s and using the current at each electrode at t = 330 s in order to obtain a calibration factor in the presence of a uniform background concentration. (B) Photograph of the 2D culture of astrocytes seeded in a chambered cover glass well prior to H_2O_2 exposure. (C) Concentration transients measured with the five electrodes in the MEA, at the positions illustrated in (A), corresponding to H_2O_2 exposure started at t = 0. The concentration amplitudes follow the order E1 < E2 < E3 < E4 < E5, clearly indicating the presence of a dynamic gradient. (D) Gradients calculated from measured concentrations at adjacent electrodes and corresponding diffusive fluxes, which are in the range of 0.7-1.4 pmol cm^{-2} s^{-1} and decrease with time due to depletion of the local concentration.

by a 2D cell culture of human astrocytes (using spatial range of 560 μm). The diffusive fluxes associated to the measured gradients exhibited values in the range of 0.7-625 pmol cm^{-2} s^{-1}, being this a range that holds physiological relevance. Taken together, these results demonstrate the design, fabrication and application of amperometric MEAs and in situ transient calibration for the measurement of physiological gradients and fluxes in real time.

3.6 Acknowledgements

The author thanks The National Science Foundation (NSF Nano-biosensing Program Grant #1403582) and the Colombia-Purdue Institute for Advanced Scientific Research for supporting this work. The author acknowledges the valuable insights, comments and guidance provided by Prof. David B. Janes, Prof. Jenna L. Rickus, and Prof. Muhammad A. Alam. The author also acknowledges the collaboration with Siddarth Sridharan to share the design/fabrication of the MEAs and execution of the experiments, and the collaboration with James K. Nolan to culture and assay the astrocytes.

4. MEASUREMENT OF HYDROGEN PEROXIDE UPTAKE KINETICS OF HUMAN ASTROCYTES AND GLIOBLASTOMA MULTIFORME CELLS IN 2D CULTURE

The content in this chapter corresponds to a published journal article: Rivera JF, Sridharan SV, Nolan JK, Miloro SA, Alam MA, Rickus JL, Janes DB, *"Real-time characterization of uptake kinetics of glioblastoma vs. astrocytes in 2D cell culture using microelectrode array"*, Analyst, 2018; 143(20):4954–4966.

4.1 Abstract

Extracellular measurement of uptake/release kinetics and associated concentration dependencies provides mechanistic insight into the underlying biochemical processes. Due to the recognized importance of preserving the natural diffusion processes within the local microenvironment, measurement approaches which provide uptake rate and local surface concentration of adherent cells in static media are needed. This paper reports a microelectrode array device and a methodology to measure uptake kinetics as a function of cell surface concentration in adherent 2D cell cultures in static fluids. The microelectrode array simultaneously measures local concentrations at five positions near the cell surface in order to map the time-dependent concentration profile which in turn enables determination of surface concentrations and uptake rates, via extrapolation to the cell plane. Hydrogen peroxide uptake by human astrocytes (normal) and glioblastoma multiforme (GBM43, cancer) was quantified for initial concentrations of 20 to 500 μM over time intervals of 4000 s. For both cell types, the overall uptake rate versus surface concentration relationships exhibited non-linear kinetics, well-described by a combination of linear and Michaelis-Menten mechanisms and in agreement with the literature. The GBM43 cells showed a higher uptake rate over the

full range of concentrations, primarily due to a larger linear component. Diffusion-reaction models using the non-linear parameters and standard first-order relationships are compared. In comparison to results from typical volumetric measurements, the ability to extract both uptake rate and surface concentration in static media provides kinetic parameters that are better suited for developing reaction-diffusion models to adequately describe behavior in more complex culture/tissue geometries. The results also highlight the need for characterization of the uptake rate over a wider range of cell surface concentrations in order to evaluate the potential therapeutic role of hydrogen peroxide in cancerous cells.

4.2 Introduction

In studies involving uptake or release of selected extracellular analytes, determination of kinetic information is vital to move from phenomenological descriptions to mechanistic insight on fundamental cellular processes, [1] such as signaling [90–94] and metabolism. [95, 96] Simultaneous measurement of uptake/release rates and concentrations at the cell surface has generally involved adherent cell cultures in stirred fluid or suspended cells in static fluid. While these configurations can be characterized using volumetric approaches, the chemical microenvironment, which includes natural diffusion of chemical species, local depletion of consumed analytes, build-up of byproducts, and availability of cell-secreted soluble factors, [97–99] is altered by the stirring or the distributed nature of cells in suspension. [100] Approaches which better maintain the natural diffusion processes within the microenvironment, e.g., adherent 2D cell cultures in static media, can in principle account for the influence of the chemical microenvironment on the cell behavior. However, the relevant concentration in static media is the concentration at the cell surface, which can be significantly different from the concentration yielded by volumetric approaches. To address this problem, this paper presents time-resolved measurements of gradients and concentrations within few hundred of μm from adherent 2D cell cultures in static media to

simultaneously determine concentrations and uptake rates at the cell surface. The ability to simultaneously determine surface concentration and uptake rate can provide mechanistic insight beyond first-order reaction kinetics, enable development of more sophisticated diffusion-reaction models, and potentially help explain the differences in cell behavior in 2D versus 3D cultures.

As a representative example, as well as the focus of this paper, consider the cellular uptake of hydrogen peroxide (H_2O_2), a reactive oxygen species (ROS) that plays a vital role in the normal cell functioning when tightly regulated [94, 101–104] and is associated to neurodegenerative diseases [105] and cancer onset [96] when dysregulated. The uptake rate of H_2O_2 (U_R), defined as the number of H_2O_2 molecules transported across the plasma membrane per unit time per cell (or per unit mass of protein), has been widely studied in bacterial, [106] fungal [93, 107] and mammalian cells, [61–63,103,108–117] including brain cells such as neurons, astrocytes and glioma cells. Neurons have the highest glycolytic rate in brain and are a major producer of ROS, including H_2O_2, [118] but the cooperative coupling of neurons with astrocytes neutralizes H_2O_2. [61, 119, 120] Glioblastoma multiforme (GBM) is the most aggressive form of brain cancer, [121] originated from astrocytes [122] and, like astrocytes, express similar mechanisms to scavenge H_2O_2. [123] Maintenance of ROS levels in GBM is pivotal since high oxidative stress aids malignant progression but insufficient regulation results in cytotoxicity. [124] GBM reliance on antioxidant defenses to control metabolically-associated ROS, including H_2O_2, is a vulnerability which could be exploited therapeutically [96, 125] and therefore has motivated the recent interest in characterization of H_2O_2 uptake rate of cancer vs. normal cells. [96,112,117,126,127]

While many studies on H_2O_2 uptake by various cell types have focused on the low concentration range where the uptake rate follows first-order kinetics, i.e., the uptake rate is proportional to the concentration, [61–64, 103, 109–112] other studies have extended the concentration range and found that uptake rate exhibits a non-linear dependence on concentration for various cell types, including astrocytes and glioma cells. [113–117] Separate determination of enzyme activities allowed this behavior to

be ascribed to a combination of linear kinetics due to catalase (CAT) and Michaelis-Menten kinetics due to glutathione peroxidase (GPx1). [113–117] Since these observations were obtained with adherent cell cultures in stirred fluid, it is thus desirable to arrive at the same results but in static media.

Dynamic mapping of the concentration profile near the cell surface allows for determination of surface concentration (C_S) and surface gradient (G_S) by extrapolation to the cell plane. Surface uptake flux (F_S) is derived from G_S using Fick's law. Available fluorometric assays for extracellular H_2O_2 detection (see reviews [71, 128–130]) have not been used to dynamically map concentration profiles. The most popular fluorometric assays, 10-acetyl-3,7-dihydroxyphenoxazine and boronate-based probes, are irreversible and therefore measure cumulative bulk effects rather than real-time local concentrations. [71, 129, 131, 132] In contrast, electrochemical techniques like scanning electrochemical microscopy (SECM) [2–6] and self-referencing vibrating probe (SR) [7–13] can map concentration profiles perpendicular to the surface of 2D cell cultures [9, 12, 14] but are generally limited in terms of the overall measurement time required to obtain multi-point concentration measurements over relevant spatial scales, without perturbing the solution around the probe tip. [2, 9–14, 17] Electrochemical techniques based on microelectrode arrays (MEAs) [33–49, 133] can provide real-time, customizable (in time and space) measurement capabilities and are more amenable to miniaturization, automation, and lab-on-a-chip integration, [46, 134, 135] which are desirable features for applications like point-of-care, microfluidic cell cultures, high-throughput drug screening, and space missions. MEAs have been generally utilized for 2D imaging of ex-vivo tissue and multi-point detection of cellular exocytotic release. Recently, MEA geometries and measurement approaches suitable for real time measurement of multi-point concentrations/gradients near aerobic granules and 2D cell cultures have been reported. [34, 133]

In this study we have utilized a MEA-based approach to measure the time-dependent local concentration of H_2O_2 at multiple spatial locations near the surface of adherent 2D cell cultures of human astrocytes and glioblastoma multiforme (GBM43)

cells in unstirred solutions. At each time point, the spatial profile is extrapolated to the cell plane to determine the corresponding C_S and G_S. Experiments over a range of initial concentrations (20-500 μM) allow determination of relationships between U_R and C_S. For both cell types, we found that the uptake rate is non-linear with the cell surface concentration, and this behavior is described by a combination of linear and Michaelis-Menten kinetic mechanisms, in agreement with observations from astrocytes and glioma cells from rat. [117] The obtained kinetic parameters describe the concentration dependence of the uptake rate and therefore can be used to refine reaction-diffusion models of antioxidant metabolism. Our results point to the need for characterization of U_R over a wider range of C_S whenever H_2O_2 plays a role as a therapeutic agent against cancer. Altogether, the MEA, methodology and experimental results constitute a proof-of-concept of on-chip characterization of H_2O_2 uptake kinetics of cancer vs. normal cells.

4.3 Experimental

4.3.1 Reagents

Human cerebral cortex astrocytes, astrocyte medium, cell freezing medium and 10 mg/ml poly-L-lysine were purchased from ScienCell Research Laboratories (Carlsbad, CA). Dulbecco's Modified Eagle's Medium (DMEM) and EDTA solution were purchased from Life Technologies (Carlsbad, CA). Astrocyte medium contained 500 ml of basal medium, 10 ml of fetal bovine serum (FBS, Cat. No. 0010), 5 ml of astrocyte growth supplement (AGS, Cat. No. 1852) and 5 ml of penicillin/streptomycin solution (P/S, Cat. No. 0503). Glucose solution (50 ml of 200 g/L) and chambered coverglass systems with 1.0 borosilicate glass and 4-wells were purchased from Thermo Fisher Scientific (Waltham, MA). Hydrogen peroxide 30% (w/w) was purchased from Alfa Aesar (Ward Hill, MA) and phosphate buffer saline (PBS) pH 7.4 was purchased from Sigma-Aldrich (St. Louis, MO).

Table 4.1.
List of symbols and units.

Symbols	Definition and Units
$C(z,t)$	Concentration of H_2O_2 as a function of position z and time t (μM)
C_0	Initial concentration (μM)
C_S	Surface concentration (μM)
C_{bulk}	Concentration at the air/solution interface (μM)
G_S	Surface gradient (μM μm^{-1})
F_S	Surface uptake flux (pmol cm^{-2} s^{-1})
U_R	Uptake rate (fmol s^{-1} cell^{-1})
k_F	Uptake rate factor, defined as the ratio U_R/C_S (L s^{-1} cell^{-1})
k_1	Rate constant of the linear kinetic mechanism (L s^{-1} cell^{-1})
J_0	Saturation rate of the Michaelis-Menten kinetic mechanism (fmol s^{-1} cell^{-1})
k_2	Concentration at $J_0/2$ (μM)
k_{obs}	Observed rate constant during volumetric sampling (s^{-1})
k_{cell}	k_{obs} normalized by the number of cells per unit volume of solution (L s^{-1} cell^{-1})
A	Culture area (cm^2)
N	Number of cells (cell)
V	Volume of solution (L)

4.3.2 MEA design, fabrication and characterization

The 1D MEA array consists of five electrodes (10 μm $\times$ 10 μm) with inter-electrode separation of 140 μm center-to-center such that the spatial range of the gradient measurements is 560 μm (Fig. 4.1). Electrodes are located very close to the bottom edge of the silicon die and are designated E1, E2, E3, E4 and E5. Relative to the bottom edge of the die, E1 and E5 are the closest and the farthest electrodes, respectively. Fig. S-3† provides details of the microfabrication process. Platinum black was electrodeposited to increase the sensitivity of the electrodes, using reported protocols. [13, 81] Electrodes were characterized for H_2O_2 response by performing cyclic voltammetry and amperometry in unstirred solution, finding sensitivity variations from electrode to electrode (21.8%) and from experiment to experiment (2.5%). The effects of these sensitivity variations are minimized via in situ transient calibrations where calibration factors are acquired immediately prior to the measurements near the cell surface. [133] No additional functionalization was required to achieve selectivity for H_2O_2 in the medium consisting of glucose and buffered inert electrolyte (phosphate buffer saline), a composition commonly found in the literature. [62, 64, 65, 73–77, 117] Control experiments (Fig. S-1†) showed that background signals measured for astrocytes and GBM43 in PBS/glucose (without H2O2) were smaller than the signal measured during exposure to 20 μM H_2O_2. The relative sensitivities of the electrodes to H_2O_2, glucose and lactate were also characterized (Fig. S-2†), and the selectivities of H_2O_2 with respect to glucose and lactate were found to be 1130 and 437, respectively. In general, changes in metabolic activity upon exposure to H_2O_2 would change the magnitude of background signals. Reports from the literature can be used to estimate the relative effects. The exposure of rat astrocytes to a sustained concentration of 50 μM H_2O_2 for 2 hours has been reported to reduce both glucose uptake and lactate release. [136] While some types of cancer cells release H_2O_2 due to oxidative stress, [137, 138] no release of H_2O_2 by human glioblastoma cells has been observed upon exposure to H_2O_2. [139] Therefore, for cells in PBS/glucose with or without

H_2O_2, the response due to cellular release of interferents (if any) is expected to be below the magnitude of the signals measured for H_2O_2, even for the smallest H_2O_2 concentration in this study.

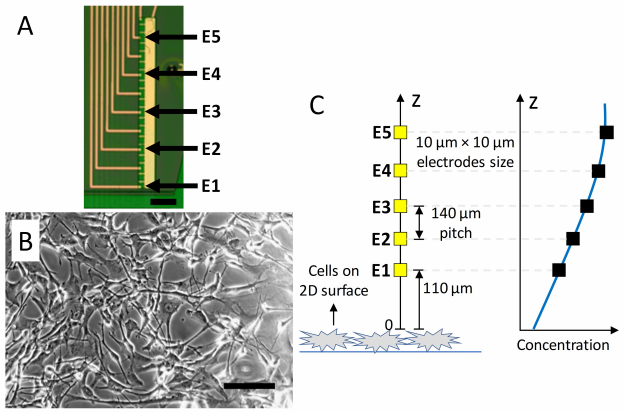

Fig. 4.1. **MEA simultaneously measures concentrations at five positions near the surface of cells in 2D cell culture.** (A) Photograph of a representative MEA. 10 platinum microelectrodes, 10 μm $\times$ 10 μm each, are arranged in a one-dimensional array, with the five electrodes indicated by arrows used in experiments, thus yielding a pitch of 140 μm. Scale bar is 100 μm. (B) Photograph of a representative culture of human astrocytes on a 2D surface. Scale bar is 100 μm. (C) Schematic of the experimental setup (not drawn to scale) illustrating how the five MEA electrodes acquire five spatial data points of the concentration profile near the cell surface. The MEA packaging allows positioning of E1 at 110 μm from the cell surface.

4.3.3 Apparatus and method for spatio-temporal resolution of gradients

The schematic diagram in Fig. 4.1(C) illustrates a reaction-diffusion system comprising a 2D cell culture (astrocytes or GBM43) surrounded by H_2O_2 solution and having five MEA electrodes arranged perpendicularly to the cell culture plane. Each electrode in the MEA operates amperometrically due to the application of a potential that drives the electrooxidation of H_2O_2 at the electrode surface and results in an electrical current proportional to the local concentration of H_2O_2. The MEA electrodes

were individually addressed by dedicated potentiostats (Reference 600, Gamry Instruments Inc., Warminster, PA) using shared counter and reference electrodes. The counter electrode was a platinum wire of 0.5 mm diameter and the reference electrode was Ag/AgCl (sat'd 3M NaCl), both purchased from BASI Inc. (West Lafayette, IN). Unless stated otherwise, all potentials are referred to the Ag/AgCl (sat'd 3M NaCl) reference electrode, and all experiments were performed at room temperature. The 1D arrangement of the MEA electrodes allows mapping of the concentration profile over a spatial range of 560 μm. The sampling period of each electrode was set at 0.5 s. The measurements were run in a sequence of steps, as follows. Initially, no intentional H_2O_2 was in the culture medium. Upon exposure to H_2O_2 at t = 0 s, the cells immediately begin uptaking H_2O_2 and this uptake generates a transient concentration gradient in the direction perpendicular to the cell culture plane. As it is usual in amperometric measurements, the signals must be conditioned for some time such that the diffusion field around each electrode is reasonably stable. In the present study the conditioning time is 300 s and begins by biasing the electrodes 30 s after H_2O_2 exposure. During the conditioning time the MEA chip edge is at 5 mm from the cell surface, and just at the end of this conditioning time (i.e., at t = 330 s) the chip edge is positioned at 30 μm from the cell surface using a XYZ motion control system (Applicable Electronics, New Haven, CT). This movement of the MEA chip from 5 mm to 30 μm takes 4 s. The relevant data is thus acquired from t = 334 s onwards and the electrode closest to the cell surface (i.e., electrode E1) is located at 110 μm from the cell surface, as illustrated in Fig. 4.1. The amperometric signals measured at t = 330 s and the bulk initial concentration of H_2O_2 provided the information to compute the calibration factors for the electrodes, as reported elsewhere. [133]

4.3.4 Astrocyte cell culture

Human cerebral cortex astrocytes arrived from ScienCell (Carlsbad, CA) cryopreserved at passage one. Astrocytes were expanded and maintained according to

the company's protocol. For each measurement of H_2O_2 consumption, passage-three astrocytes (5.0×10^4 cells cm^{-2}) were seeded onto poly-L-lysine-coated chambered coverglass 4-well systems and incubated for two days in a humidified atmosphere at 37 °C with 5% CO_2. Medium was replaced with fresh astrocyte medium one day after seeding. H_2O_2 uptake rate was measured after two days of incubation. By this time, cultures had grown to approximately 1.2×10^5 cells cm^{-2}. This number was calculated from a growth curve of three human astrocyte cultures (5.0×10^4 cells cm^{-2}) counted each day of incubation for three days. The doubling time was calculated to be 1.547 days. The exponential fit of the cell counts had an $R^2 > 0.99$. Cells were counted by hemocytometer and viability was determined through Trypan Blue Exclusion. Individual cell counts for each culture were acquired immediately following each measurement.

4.3.5 Glioblastoma cell culture

Primary patient-derived GBM43 cells were provided by Dr. Jann Sarkaria (Mayo Clinic, Rochester, MN) and have been described prior. [140] Cells were maintained in Dulbecco's Modified Eagle's Medium (DMEM) containing 10% fetal bovine serum in humidified atmosphere at 37 °C with 5% CO_2. Cells were propagated in T75 flasks and fed with growth media every other day. Cells were enzymatically dissociated using 0.25% trypsin/0.5 mmol L^{-1} EDTA solution and passaged every 3 days. For each measurement of H_2O_2 uptake rate, propagated GBM43 cells were trypsinized and plated at a density of 10^5 in 1 mL of growth media in 12-well plates (Corning Costar 3515). H_2O_2 uptake rate was measured after the cells had grown to confluency over 3 to 4 days. Cells were counted by hemocytometer and viability was determined through Trypan Blue Exclusion. Individual cell counts for each culture were acquired immediately following each measurement.

4.3.6 Cell imaging and preparation for MEA measurements

Prior to exposing cultures to H_2O_2 and measuring uptake rate, cultures were imaged at 100X magnification with ToupView then washed twice with 5.5 mM glucose in PBS (pH 7.4). The culture wells were then filled with 0.3 ml (astrocytes) or 1 ml (GBM43) of 5.5 mM glucose in PBS. Next, the culture wells and MEA were put in position for measurement. Finally, 1.2 ml (astrocytes) or 2 ml (GBM43) of PBS with 5.5 mM glucose and H_2O_2 was added, so the resulting H_2O_2 concentrations were 20, 60, 100, 200, 300 or 500 μM in total volumes of 1.5 ml (astrocytes) or 3 ml (GBM43). The corresponding surface area and height of the liquid were 1.8 cm^2 and 0.83 cm (astrocytes), and 3.8 $cm^2$and 0.79 cm (GBM43), respectively. Following each measurement in H_2O_2 solution, cells were imaged again. Fig. S-4† shows representative pictures of astrocyte and GBM43 cultures before and after exposure to 500 μM H_2O_2.

4.3.7 Viability assays

Live/dead assay of astrocyte and GBM43 was used to assess viability of cells after 2 hours of H_2O_2 exposure. Cultures were treated in one of four ways: (1) 2 hours in PBS with 5.5 mM glucose, (2) 2 hours in PBS with 5.5 mM glucose and 500 μM H_2O_2, (3) 20 minutes in formalin (negative control), and (4) directly assayed without treatment (positive control). Following treatment, cultures were stained with CellTracker Green (live stain) and propidium iodide (dead stain) (Thermo Fisher Scientific). Images were obtained using confocal fluorescence microscopy with model FV1000 (Olympus). Fig. S-5† shows the results. Two hours in 500 μM H_2O_2 had no apparent harmful effect on glioblastoma viability (Fig. S-5(H)†). On the other hand, two hours in H_2O_2 caused a fraction of astrocytes to lose adherence and thus being washed away during the live/dead assay, which would explain the apparent reduction in cell confluence (Fig. S-5(D)†). However, the astrocytes that remained adhered were viable.

4.3.8 Simulation details and numerical model

Since the concentration field induced by cellular uptake of H_2O_2 is one dimensional, i.e., perpendicular to the plane of cell culture, the simulation geometry consisted of a one-dimensional domain with length L equal to the distance between the cell surface and the solution/air interface, as shown in Fig. S-6†. The diffusion equation (4.1) is solved numerically using Comsol finite element software,

$$\frac{\partial C(z,t)}{\partial t} = D\frac{\partial^2 C(z,t)}{\partial z^2} \tag{4.1}$$

where $C(z,t)$ is the concentration of H_2O_2 as a function of position z and time t, and $D = 1.71\times\ 10^{-9}$ m^2 s^{-1} is the diffusion coefficient of H_2O_2. [72] The boundary condition at the cell surface, located at $z = 0$, is set by U_R which is a function of C_S, as given by Eq. (4.2),

$$D\frac{A}{N}\frac{\partial C(z,t)}{\partial z}\bigg|_{z=0} = U_R = k_F(C_S)\cdot C_S \tag{4.2}$$

where A is the culture area and N is the number of cells. The C_S dependent uptake rate factor $k_F(C_S)$ is defined as the ratio U_R/C_S. As discussed in Section 4.4.4, the U_R vs. C_S relationship for each cell type is determined from experiments at multiple initial concentrations C_0, and $k_F(C_S)$ is expressed in units of L s^{-1} $cell^{-1}$. The boundary condition at the air/solution interface is set to zero flux, as given by Eq. (4.3).

$$D\frac{\partial C(z,t)}{\partial z}\bigg|_{z=L} = 0 \tag{4.3}$$

For each cell type, simulations were performed at the same values of C_0 used in the experiments, i.e., $C(z,0) = C_0$ where C_0 = 20, 60, 100, 200, 300 or 500 μM.

4.4 Results

4.4.1 Real time acquisition of transient concentrations at multiple positions from the cell surface

Fig. 4.2 shows representative concentration transients measured in real time at the electrode positions during experiments wherein the cell cultures of astrocytes and

GBM43 are exposed to C_0 of 100 μM H_2O_2. Electrodes are labeled as E1 through E5, with E1 and E5 denoting the electrodes nearest to and farthest from the cell surface, respectively. These signals were acquired with sampling period of 0.5 s and were neither filtered nor averaged over time. Corresponding results for C_0 of 20, 60, 200, 300 and 500 μM H_2O_2 are included in Fig. S-7†. The relative values of the concentration amplitudes (E1 < E2 < E3 < E4 < E5) indicates the presence of a gradient in H_2O_2 concentration due to cellular uptake. The recorded concentration transients shown in Fig. 4.2 provide the information required to dynamically map the concentration profile of H_2O_2 and determine the corresponding uptake kinetics.

4.4.2 Mapping of the dynamic concentration profile from experimental data

Fig. 4.3 shows concentration as a function of distance from the cell surface at selected time points for both astrocytes and GBM43 cells exposed to C_0 of 100 μM H_2O_2. Solid symbols are experimental data points obtained from the MEA electrodes (E1-E5) at the indicated time points. The solid red lines represent fits at the corresponding time points, discussed later. Collectively, the data points indicate the evolution of $C(z,t)$ measured over a spatial scale of ~700 μm and for various time points between 360 and 4000 s. Although the concentration at each electrode was sampled every 0.5 s, as shown in Fig. 4.2, $C(z,t)$ is only shown for selected time points for the sake of clarity. Corresponding results for C_0 of 20, 60, 200, 300 and 500 μM H_2O_2 are included in Fig. S-6†.

The uptake of H_2O_2 at the 2D cell surface depletes the analyte nearby and therefore induces a one-dimensional concentration gradient extending continuously into the bulk solution. Overall, the GBM43 cells exhibit higher H_2O_2 U_R than the astrocytes since the concentrations near the surface of GBM43 cells are smaller than those of astrocytes. While a nonlinear $C(z,t)$ was observed for both cell types at early times (0-500 s), non-linearity is more evident in GBM43 cells due to higher U_R. Beyond

500 s, the $C(z,t)$ over the spatial scale addressed is linear for both cell types. For

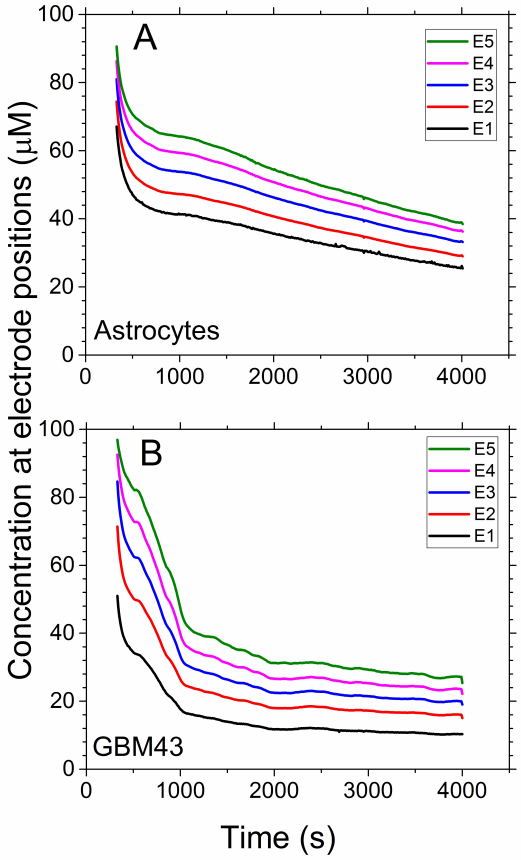

Fig. 4.2. **Curves are representative measurements of local concentrations at the positions of the electrodes E1-E5 (located within 700 μm from the cell surface) for astrocytes (A) and GBM43 (B) exposed to C_0 of 100 μM H_2O_2.** The sampling period is 0.5 s and no filtering nor moving-window averaging is performed on the acquired signals. A 330 s interval between addition of H_2O_2 (t = 0 s) and start of measurement allows stabilization of electrode response, and in-situ calibration technique described in text utilizes the current at each electrode at the end of that interval. The order in the amplitudes of the signals, E1 < E2 < E3 < E4 < E5, indicates the presence of a concentration gradient since E1 and E5 are the closest and farthest electrodes from the cell surface, respectively. Measurements were conducted with astrocytes and GBM43 cells at various initial concentrations, as described in text.

each time point, C_S and G_S can be obtained via extrapolation of the concentration

to $z = 0$ and calculation of the corresponding gradient, respectively. Considering the nonlinear $C(z,t)$ observed in the experimental points in Fig. 4.3, particularly at earlier time points, a simple linear extrapolation does not provide accurate values for C_S and G_S. In order to provide an expression which better fits the experimental data and can be directly related to physical parameters, a general form of an expression describing a first-order irreversible reaction at a planar electrode in contact with a semi-infinite volume of solution [24] (see discussion and original expression in ESI†) was employed,

$$C(z) = A_1 \left[1 + A_2 erfc(A_3 z)\right] \tag{4.4}$$

where A_1, A_2 and A_3 are fitting parameters. Eq. (4.4) was used to fit the experimental concentration versus distance data at time points spaced by 10 s. Fig. 4.3 shows the fitted curves (solid red lines) corresponding to the experimental data sets presented in the figure. In the current study, the depth of the solution is finite and the 2D monolayer of cells is expected to act as H_2O_2 sink exhibiting kinetics beyond first-order; hence the fitting parameters A_1, A_2 and A_3 will have somewhat different but related physical interpretations from the original expression. The fitting was performed at each time point independently, without carrying any information over from prior time points, and the obtained best fits consistently provided $R^2 > 0.99$ at every time point for all the experiments: 36 experiments in total; 18 experiments for each cell type, comprising triplicates of 6 initial concentrations. The experimental results were also fitted by linear regressions (not shown), resulting in R^2 values within 0.79–0.95 and therefore confirming that fitting to a well-established diffusion-reaction model is better than simple linear regression.

4.4.3 Determination of surface concentration and gradient from experimental data

Once A_1, A_2 and A_3 are determined for a given time, the corresponding $C_S(t)$ and $G_S(t)$ can be obtained using expressions developed from Eq. (4.4), namely

$$C(z,t)|_{z=0} \equiv C_S(t) = A_1 + A_2 \tag{4.5}$$

$$\left.\frac{\partial C(z,t)}{\partial z}\right|_{z=0} \equiv G_S(t) = -\frac{2A_2A_3}{\sqrt{\pi}} \tag{4.6}$$

Curves of C_S and G_S versus time are determined using (4.5) and (4.6), respectively, for all the experiments performed in this study. The triplicate curves of C_S and G_S for each initial concentration are combined into averaged curves, and these averaged curves are indicated by solid lines in Figs. 4.4 and 4.5, respectively, for astrocytes and GBM43 cells exposed to C_0 of 20, 60, 100, 200, 300 and 500 μM H_2O_2. The error bars indicate standard deviation of the averaged curves (n = 3). The dashed lines in Figs. 4.4 and 4.5 represent the results of simulations for the corresponding C_0, discussed later. G_S is presented in units of μM μm^{-1} to facilitate physiological interpretations but other relevant units such as mol cm^{-4} can be obtained using appropriate conversion factors. Using the H_2O_2 diffusion coefficient from the literature, [72] the G_S values are converted into surface fluxes (F_S) as indicated by the corresponding scale in Fig. 4.5. Considering the whole spectrum of C_0 from 20 to 500 μM, astrocytes show less uptake than the GBM43 cells. Although both astrocytes and GBM43 cells showed changes in morphology after exposure to 300 and 500 μM H_2O_2 (see Fig. S-4†), the cells kept consuming H_2O_2, highlighting the robust nature of the oxidant scavenging mechanisms present in both cell types. Separate live/dead stains (see Fig. S-5†) performed on the cells after exposure to 500 μM H_2O_2 indicated high viability of both cell types. The GBM43 cells exhibited better viability than astrocytes, suggesting that the cancerous cells are more resilient to H_2O_2 than their healthy counterparts. The dashed lines in Figs. 4.4 and 4.5 are simulated curves obtained from numerical solutions of the reaction-diffusion model (see Section 4.4.4) at the indicated C_0, using the geometry of the 2D cell culture and the kinetic parameters extracted

from analysis of U_R as a function of C_S, as discussed in Section 4.4.5. It is important to note that only C_0 is modified from simulation to simulation, indicating that the diffusion model developed here qualitatively captures the physics of cellular uptake of H_2O_2 over the different time regimes and over the whole spectrum of C_0.

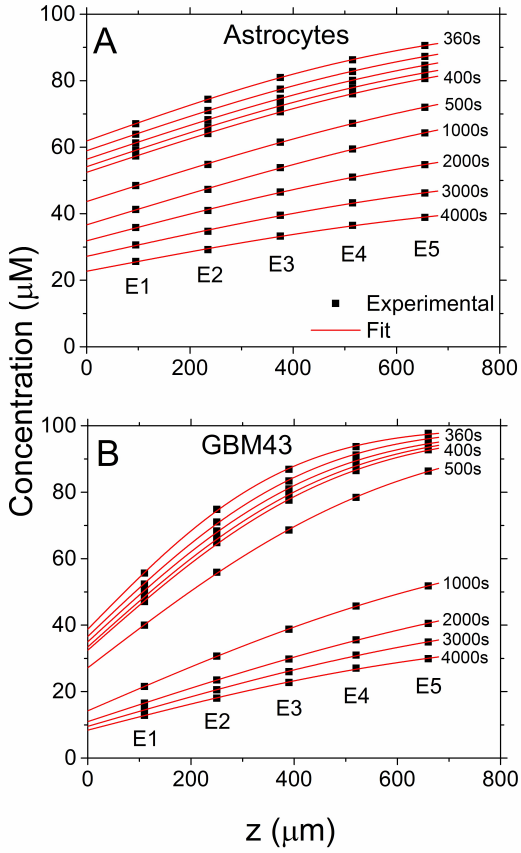

Fig. 4.3. **Representative concentration profiles at the indicated time points, as measured by the electrodes E1-E5 (symbols) and as obtained from the best fits to a reaction-diffusion model (solid lines) for astrocytes (A) and GBM43 (B) exposed to C_0 of 100 μM H_2O_2.** The procedure for the best fits and the reaction-diffusion model are described in the text. For clarity, the profiles are shown at relatively fewer time points as compared to the sampling time of 0.5 s. Concentration profiles within 360 and 400 s are shown in steps of 10 s. The data fits allow determination of surface concentration and surface gradient at each time point by extrapolation to the cell surface.

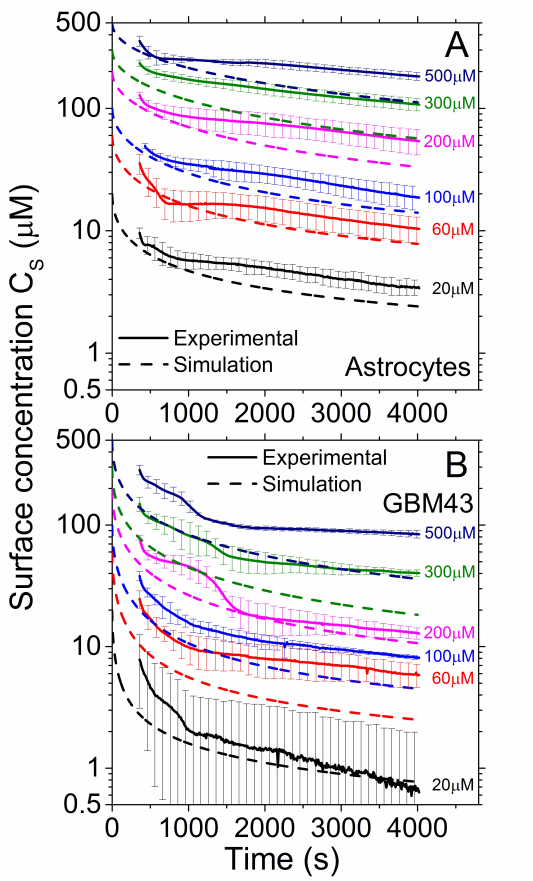

Fig. 4.4. **Transient surface concentrations, C_S, for experiments with the indicated C_0 values for astrocytes (A) and GBM43 (B), as extrapolated from the concentration profiles fitted from experimental data (solid lines) and as obtained from simulations (dashed lines).** Data points in solid lines are spaced by 10 s. Error bars indicate standard deviation of the mean value from triplicate experiments. For the sake of clarity, error bars are plotted every 100 s. The kinetic parameters (see Table 4.2) were kept fixed and only the initial concentrations were changed from simulation to simulation. Other simulation details are described in the text.

4.4.4 Real time determination of uptake kinetics and extraction of kinetic parameters

The transient behavior of C_S and G_S discussed above captures the effects of cellular kinetics in conjunction with the diffusion profile in the given geometry. In order

to minimize variability in cell density between multiple experiments and extract the kinetic parameters in the same units as standard volumetric rate constants (see Discussion), the F_S (mol cm^{-2} s^{-1}) presented in Fig. 4.5 is normalized to the cell density (cell cm^{-2}) to obtain U_R on a per cell basis (mol s^{-1} cell^{-1}).

Open symbols in Figs. 4.6 and 4.7 indicate the values of U_R versus C_S extracted from experimental data for astrocytes and GBM43; both figures present the same data but over different ranges of C_S to help visualize some details in the U_R–C_S relationship. For each cell type, data is plotted for the various C_0 values in order to span the whole spectrum of concentrations for both cell types. This yields a series of overlapping segments (e.g. within astrocyte data, segments corresponding to C_0 of 300 and 500 μM correspond to segments covering C_S ranges of $\sim$110-240 μM and $\sim$175-350 μM, respectively). Shaded bands surrounding the open symbols indicate standard deviation of the mean value of U_R (n = 3). Overall, the U_R–C_S relationships are observed to be non-linear. The solid lines passing through the experimental data points (open symbols) in Figs. 4.6 and 4.7 are best fits to Eq. (4.7), which describes the dependence of U_R on C_S using established kinetic mechanisms, namely linear (first term) and Michaelis-Menten (MM) [141, 142] (second term),

$$U_R(C_S) = k_F(C_S) \cdot C_S = \left[k_1 + \frac{J_0}{k_2 + C_S} \right] \cdot C_S \tag{4.7}$$

where k_1 is the rate constant of the linear mechanism, J_0 is the saturation uptake rate of the MM mechanism and k_2 is the MM constant (i.e., concentration at $J_0/2$). Note that the term in the brackets in Eq. (4.7) is the definition of the uptake rate factor $k_F(C_S)$, which clearly demonstrates the deviation from first-order kinetics. Eq. (4.7) was fit to the data in Fig. 4.6 using k_1, k_2 and J_0 as fitting parameters. The data fitting procedure included the overlapping data points (points from multiple C_0 overlapping over portions of their corresponding C_S ranges), along with the standard deviation of U_R (shaded bands in Fig. 4.6). The inclusion of the standard deviation of U_R in the data fitting places stronger weighting on data points having the least uncertainty. R^2 for astrocytes and GBM43 cells are 0.997 and 0.985, respectively.

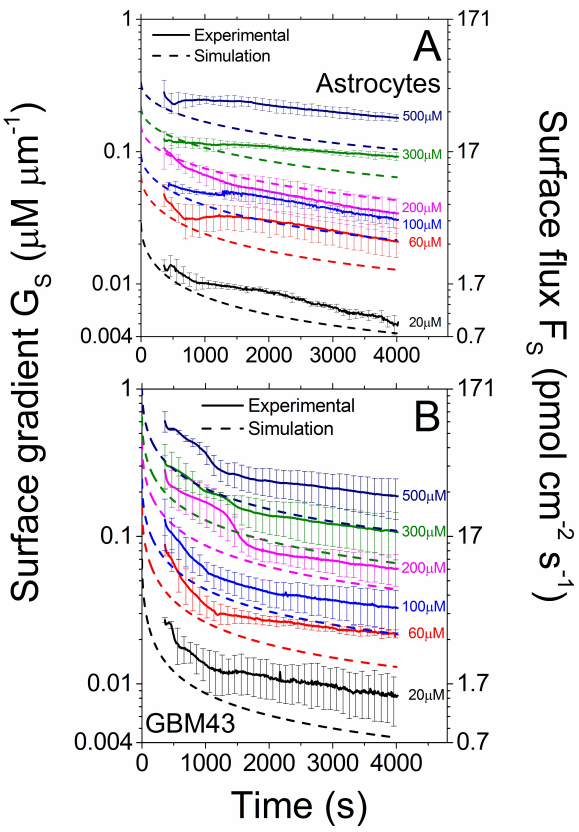

Fig. 4.5. **Transient surface gradients, G_S, for experiments with the indicated C_0 for astrocytes (A) and GBM43 (B), as extrapolated from the concentration profiles fitted from experimental data (solid lines) and as obtained from simulations (dashed lines).** The corresponding surface flux, F_S, (right axis) is computed as the product of G_S and diffusion coefficient of H_2O_2. Data points in solid lines are spaced by 10 s. Error bars indicate standard deviation of the mean value from triplicate experiments. For clarity, error bars are plotted every 100 s. The kinetic parameters (see Table 4.2) were kept fixed and only the initial concentrations were changed from simulation to simulation. Other simulation details are described in the text.

The extracted values of k_1, k_2 and J_0 are presented in Table 4.2 for astrocytes and GBM43 cells.

Fig. 4.7 magnifies the low C_S range (0-100 μM) of Fig. 4.6 to illustrate more clearly the non-linearity of U_R vs. C_S and the transition from a regime in which

Table 4.2.
Kinetic parameters extracted from experimental data.

	k_1 (10^{-12} L s^{-1} $cell^{-1}$)	k_2 (μM)	J_0 (fmol s^{-1} $cell^{-1}$)
Astrocytes	0.87 ± 0.007	46 ± 0.8	0.09 ± 0.002
GBM43	2.3 ± 0.03	13 ± 1.3	0.06 ± 0.003

both terms contribute strongly to a regime in which the linear term dominates. In Fig. 4.7 , solid lines labeled as 'Kinetic Model Fit' are the same curves shown in Fig. 4.6 , and solid lines labeled as 'linear' and 'MM' represent the linear and MM terms from Eq. (4.7) using the corresponding values from Table 4.2. These linear and MM curves quantify the contribution of each mechanism to the measured U_R at any given C_S. The cross-over point between linear and MM curves indicates the concentration at which both mechanisms contribute equally. The cross-over points occur at 13 and 55 μM for GBM43 and astrocytes, respectively, mainly due to the fact that the linear term (k_1) is 2.5 times larger in GBM43 than in astrocytes (see Table 4.2). In the low concentration range (0–20 μM), which corresponds to the extracellular H_2O_2 concentration associated to the homeostatic level, [82,94] GBM43 and astrocytes exhibit contribution ratios of approximately 1:1 and 2:1 (MM:linear), respectively. As the concentration increases the MM mechanism reaches saturation and the linear mechanism takes over the MM mechanism. The MM saturation value (J_0) in GBM43 is 66.6% of that in astrocytes.

To illustrate how U_R–C_S deviates from first order as C_S increases, dashed lines in Fig. 4.7 show linear extrapolations of the initial slopes in the data curves, obtained from linear regressions of the experimental data of U_R–C_S in the range of 0–20 μM H_2O_2. These linear regressions yielded k_F of (2.63 ± 0.005) × 10^{-12} L s^{-1} $cell^{-1}$ for human astrocytes and (4.2 ± 0.02) × 10^{-12} L s^{-1} $cell^{-1}$ for GBM43, which are comparable to results from typical volumetric measurements, [112] as discussed in Section 4.5.

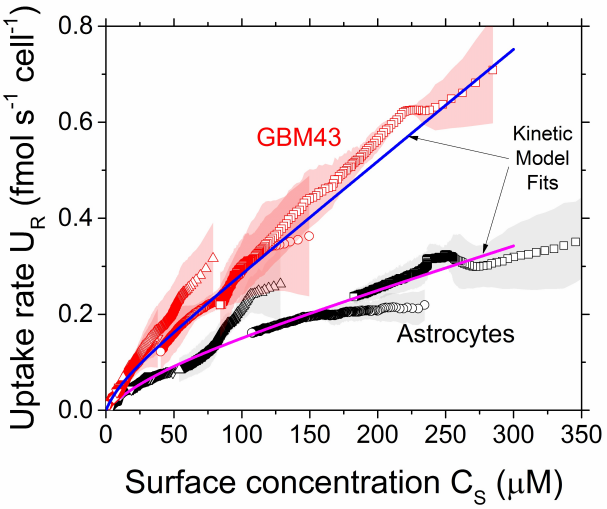

Fig. 4.6. **The uptake rate of H_2O_2, U_R, as a function of surface concentration, C_S**, for astrocytes and GBM43 as measured experimentally (symbols) and as obtained from the best fits to a kinetic model (solid lines) that considers linear and Michaelis-Menten components. U_R is computed as the experimental surface flux, F_S, divided by the cell density. Shaded bands indicate standard deviation of the mean of U_R from triplicate experiments. For each cell type, results are presented for C_0 of 500 (squares), 300 (circles), 200 (up-triangles), 100 (down-triangles), 60 (rhombuses) and 20 μM (pentagons); within each experiment at a given C_0, C_S evolves from high concentration (short time) to low concentration (long time).

4.4.5 Simulation of the 2D cell cultures based on the determined parameters

The kinetic parameters k_1, k_2 and J_0 in Table 4.2 are included in the numerical solution of a diffusion–reaction system representing the same geometry of the 2D cell culture. For a given cell type, simulations are performed at various C_0 while keeping the values of k_1, k_2 and J_0 fixed. Simulated curves of C_S and G_S versus time are indicated by dashed lines in Figs. 4.4 and 4.5, respectively. The simulation captures the qualitative features of the experimental curves, including decreasing slopes with increasing time, relative changes in C_S and G_S at long times for various values of C_0 and the relative differences between behavior of astrocytes and GBM43. The simulation did not include effects such as natural convection [98] and potential mixing effects due to the MEA chip motion at 300 s, which would result in a better fit to the data but would require assumptions regarding the magnitudes of these effects. Compared to simulations with the constant k_F extracted at low H_2O_2 concentrations (0–20 μM), the simulated curves using the kinetic parameters in Table 4.2 better capture the main features of the uptake mechanisms of astrocytes and GBM43 cells over the investigated range of C_S and over a larger time window (see Fig. S-9†).

4.5 Discussion

In this study we have demonstrated the analytical capabilities of the MEA approach to measure cellular uptake kinetics in real time. It is informative to compare the results from the current study with those from prior experiments. In typical volumetric experiments, [62, 103, 110, 143–146] a first-order rate coefficient k_{obs} (in units of s^{-1}) is obtained from

$$\frac{dC_{vol}}{dt} = -k_{obs}C_{vol} \tag{4.8}$$

where C_{vol} is the volumetric concentration. As discussed by Wagner et. al., [62] the value of k_{obs} is dependent on both the solution volume (V) and number of cells (N),

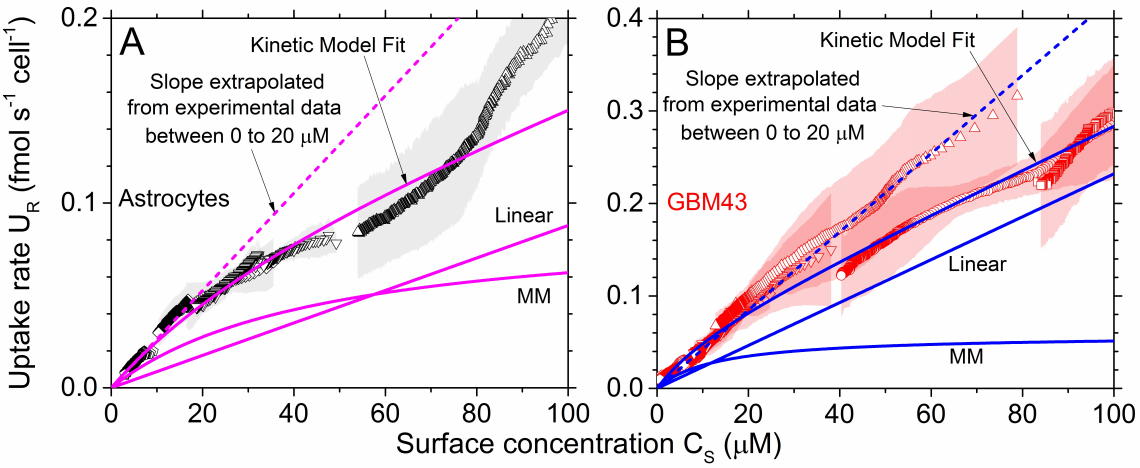

Fig. 4.7. **The uptake rate, U_R, as a function of the surface concentration, C_S, over the low concentration range for astrocytes (A) and GBM43 (B).** Experimental data points (symbols) and solid lines labeled as "Kinetic Model Fit" are the same as in Fig. 4.6, and the same symbols are used to indicate initial concentrations. Shaded bands indicate standard deviation of the mean of U_R from triplicate experiments. Linear and Michaelis-Menten (MM) kinetic components are indicated by solid lines which are labeled accordingly, illustrating the relative magnitudes and the cross-over point of the two terms. Dashed lines extrapolate the slope from experimental data within 0–20 μM in order to predict uptake rates at higher concentration range based on the conventional first-order kinetics approach.

but normalization by N and V yields a rate constant k_{cell}, in units of L s^{-1} $cell^{-1}$, which can be directly compared for various experiments.

$$k_{cell} = \frac{V}{N} k_{obs} \tag{4.9}$$

The uptake rate factor k_F, defined earlier as the ratio U_R/C_S, allows quantitative comparison of MEA results to k_{cell} or k_{obs} from volumetric measurements, independent of diffusion geometry and mass transport. Based on Figs. 4.6 and 4.7, it is clear that k_F varies with C_S; the units for U_R and C_S in these figures have been chosen in order to provide k_F in the same units as k_{cell} (L s^{-1} $cell^{-1}$). In addition to this concentration-dependence, differences between k_F values from MEA measurements and k_{cell} values from volumetric measurements are expected due to differences in cell geometry (i.e., adherent versus suspended) and different relationships between C_S and C_{vol} associated with the hydrodynamics (i.e., static versus stirred solution). In experiments involving adherent cells in stirred solutions or suspended cells, $C_S \approx C_{vol}$ and Eq. (4.8) is the governing equation, so volumetric measurements yield k_{cell} values corresponding to C_0, if sampled within a short period after exposing the cells to C_0. By considering a number of C_0 values, such techniques have been used to study the concentration-dependence of k_{cell}. [113–117] In contrast, experiments involving adherent 2D cultures exposed to analyte in unstirred solution for specific intervals, followed by stirring just prior to volumetric sampling, will have $C(z,t)$ (during the uptake period) comparable to that in the current study. In this class of experiments, the C_{vol} observed after an uptake period T_0 can be related to C_0, C_S and k_F via

$$C_{vol}(T_0) = C_0 - \frac{N}{V} \int_0^{T_0} k_F C_S(t) dt \tag{4.10}$$

For small T_0, which is typical in this class of experiments, a semilogarithmic plot of C_{vol} vs. T_0 is approximately linear and k_{cell} is extracted from the slope of this curve. Since C_S is less than the concentration averaged throughout the volume, such experiments will yield k_{cell} values lower than k_F (obtained in this work) or lower than the k_{cell} values inferred from experiments governed by Eq. (4.8). These observations

indicate that there are qualitative and quantitative differences between experiments, dictated by cell geometry (adherent or suspended) and hydrodynamics (stirred or unstirred).

In our experiments, values for k_F at low C_S were determined from the average slope of the U_R–C_S relationships in the range of $0 < C_S < 20$ μM (dashed curves in Fig. 4.7), yielding $k_F = (2.63 \pm 0.005) \times 10^{-12}$ L s^{-1} $cell^{-1}$ for human astrocytes and $(4.2 \pm 0.02) \times 10^{-12}$ L s^{-1} $cell^{-1}$ for GBM43. Using volumetric approaches with initial concentration of 20 μM, Doskey et. al. measured k_{cell} values (all in units of L s^{-1} $cell^{-1}$) between 4.4×10^{-12} and 7.3×10^{-12} for human astrocytes, 4.8×10^{-12} for GBM U87, and 4.6×10^{-12} for GBM U118. [112] Compared to Doskey et. al., our values of k_F are in the same range, although the smaller value for astrocytes relative to that for GBM43 is in opposition to the general trend of tumor cells having lower k_{cell} than normal cells. [112] Since this trend may invert itself at higher concentrations, as indicated by Makino et. al., [117] characterization over a wider range of surface concentrations is warranted if H_2O_2 is going to be used as a therapeutic agent against cancer.

The concentration dependence of U_R can also be compared to prior volumetric studies. The biphasic behavior in U_R–C_S is comparable to that reported by Makino et. al. in studies on rat astrocytes and C6 glioma using 2D cell cultures in stirred media. [113–117] These studies attributed the linear behavior to catalase (CAT) and the Michaelis-Menten behavior to glutathione peroxidase (GPx1). [117,147–149] Two observations are evident between our results for human cells and those of Makino et. al. for rat cells. First, Makino et. al. observed that C6 glioma cells exhibit a higher U_R compared to astrocytes for concentrations above 20 μM, but a lower rate between 0-20 μM. [117] In contrast, our results show higher U_R in GBM43 than in astrocytes over the entire investigated concentration range (0–350 μM). Second, the ratio of J_0 for cancer to normal cells in Makino et. al. is 1.76 whereas that ratio in our results is 0.67. [117] Based on various issues which have been raised regarding the use of rat C6 glioma as a model for human glioblastoma and comparisons regarding growth,

invasion, metastasis and drug response, [150–152] differences are expected between human and rat cells. For human cells, biochemical analyses indicate that glioblastoma contains more CAT but less GPx1 than astrocytes; [153] assuming the correlation by Makino et. al. [113] wherein the linear and MM mechanisms correspond to CAT and GPx1, respectively, our results are in qualitative agreement with that report.

The U_R–C_S relationships shown in Figs. 4.6 and 4.7 consist of sets of overlapping time trajectories, obtained using various C_0 values. For each cell type, these trajectories can provide insights into the relative effects of cumulative exposure to the analyte, e.g. by comparing the behavior at long exposure times for a large C_0 with that at short time for a smaller C_0. Such time-dependence could be used to quantify the onset of toxicity in prior studies. [103, 154] In the current experiment, the trajectories for GBM43 show a tail-off in U_R after long exposure, i.e., the U_R values fall below those extrapolated from the intermediate-time regime. Such a roll-off could be indicative of H_2O_2 toxicity or reduction in H_2O_2 scavenging ability. In the case of astrocytes, comparable roll-off is not observed. Although clear changes in morphology were observed for both cell types after exposure to 300 and 500 μM H_2O_2 (see Fig. S-4†), the roll-off in U_R was moderate even for the GBM43 cells. The continuous monitoring of C_S over the course of the experiment allows a more accurate determination of the cumulative exposure of the cells to the analyte, in comparison to experiments in unstirred solutions followed by volumetric sampling.

The MEA approach should be well-suited to assess the chemical impact of one cell type on others when multiple cell types are cultured together (i.e., co-cultured). Studies have shown that the chemical microenvironment differs significantly among 2D cultures containing one, two and three different cell types cultured together, [155] and these observations have been ascribed to paracrine signaling via cell secreted factors. [97–99, 156] Seeding of various cell types on a surface using cell patterning techniques [157] followed by co-culture could be used to measure kinetic parameters under the influence of paracrine signaling. The MEA approach allows measurements in unstirred solution, preserving the natural diffusion environment, and can in princi-

ple provide information on spatial heterogeneity, e.g., by localizing at the cell type of interest. Once the kinetic parameters are determined, they can be incorporated into 3D models to study the behavior of cells within tissue.

The MEA approach could be applied for other electroactive species without major adjustments and provides customizable spatial and temporal resolutions. Although the focus of the present study is on H_2O_2, the same MEA and methodology, except for minor adjustment of bias potential, can be used to measure uptake kinetics and C_S of other electroactive species of biological interest including dopamine and serotonin. The current experiment utilized platinum electrodes, which yielded relatively high sensitivity but also a relatively long time for stabilization of the H_2O_2 response. [26, 28–32] The latter dictated a waiting period of 300 s between addition of H_2O_2 and start of concentration measurements. Other materials, e.g., carbon electrodes, could reduce the electrode stabilization time, but trade-offs in sensitivity are expected. [28–32] As shown elsewhere, [133] parameters such as sampling period and spatial resolution can be customized to fit other requirements, e.g., sub-second transient concentrations and gradients have been measured with sampling period of 10 ms and inter-electrode distance of 35 μm.

4.6 Conclusions

In this work, we demonstrate the use of a MEA customized for typical 2D culture setups to measure dynamic H_2O_2 concentration profiles from normal (human astrocytes) versus astrocyte derived cancer (GBM43) cells. The MEA provides multi-point concentration data with a sampling period of 0.5 s. At each time point, the concentration data is fit using an analytical expression for a 1D diffusion/reaction system, allowing extrapolation of the surface concentration and surface gradient. Measurements at various initial concentrations allow determination of the uptake rate over a wide range of surface concentrations. Both cell types show surface concentration dependent uptake rates, i.e., non-linear kinetics. The results show that GBM43 cells

have increased H_2O_2 uptake rates as compared to astrocytes due primarily to an elevated linear scavenging mechanism, which has previously been attributed to catalase. The Michaelis-Menten components are comparable for the two cell types for H_2O_2 concentrations within the 0–100 μM range. A comparison of the diffusion–reaction models using the non-linear parameters and standard first-order relationships indicates that the overall behavior is better described by the non-linear relationships. As shown in Eq.(4.10) and associated discussion, our results can also be used to quantitatively understand the differences between volumetric measurements using stirred versus unstirred media during uptake.

The monitoring of U_R vs C_S can also be used to quantify cumulative exposure effects, e.g., by comparing the uptake rate observed at the same C_S for different initial concentrations and therefore different cumulative exposures to H_2O_2. In the current experiment, a tail-off in uptake rate after long exposure to high concentrations of H_2O_2 is observed for GBM43 cells. The capabilities to quantify cumulative exposure effects and uptake rates over a wide range of cell surface concentrations are relevant for both toxicity studies and evaluation of potential therapeutic approaches based on differential uptake by cancerous versus normal cells.

In addition to shedding light on mechanistic behavior, the resulting kinetic parameters should be well suited for developing reaction–diffusion models that more accurately describe more complex culture/tissue geometries. Key aspects include measurements in a more natural local environment and the ability to obtain U_R vs C_S relationship which are nominally independent of the specific diffusion geometry. The MEA technique can also be extended to mixed cultures and multi-analyte measurements, e.g., monitoring of both uptaken and released analytes. Collectively, these capabilities can provide parameters which, when coupled with a diffusion model representing a realistic geometry for influx/efflux of various analytes, can yield models which more accurately represent the behavior of 3D cultures and tissue microenvironments.

4.7 Conflicts of interest

There are no conflicts of interest to declare.

4.8 Acknowledgements

The authors thank Hannah Kriscovich and Sarah Libring for preliminary experiments, Clayton Bowes for help with culturing the cells, and the National Science Foundation (NSF Nano-biosensing Program Grant #1403582) and the Colombia-Purdue Institute for Advanced Scientific Research for supporting this work. The author acknowledges the insightful discussions, comments and guidance provided by Prof. David B. Janes, Prof. Jenna L. Rickus and Prof. Muhammad A. Alam, the collaboration with Siddarth Sridharan to share the design/fabrication of the MEAs and the execution of the experiments, and the collaboration with James K. Nolan and Stephen A. Miloro to culture and assay the astrocytes and glioblastoma cells.

5. MEASUREMENT OF GLUCOSE UPTAKE KINETICS OF HUMAN BRONCHIAL EPITHELIAL AND SMALL-CELL LUNG CANCER CELLS IN 2D CULTURE

The content in this chapter corresponds to a manuscript in preparation.

5.1 Introduction

Glucose metabolism is a physiological program comprising various processes from which animal and most non-photosynthetic cells obtain the energy to sustain life. Glucose metabolism begins with glucose uptake, a process in which proteins called membrane transport proteins (MTPs) move the glucose molecules across the cell membrane. The rate of glucose uptake (U_R), defined as the number of glucose molecules transported across the cell membrane per unit time per cell (or per unit mass of cell protein), is tightly and dynamically regulated in response to environment changes in order to maintain the cell homeostasis. Consequently, the characterization of U_R for different cell types and different conditions provides critical information to understand metabolism-related diseases. In fact, pathologies of high incidence including diabetes, myocardial ischemia, obesity and cancer have been associated to dysfunction of glucose transport and metabolism [158–161], thus motivating the development and improvement of methods and technologies to measure U_R and elucidate the underlying kinetics.

Many of the efforts to measure U_R in cell cultures have involved glucose analogs which are molecules structurally similar to glucose except for the addition of a label, which is typically a radioactive tracer or fluorophore. In these methods the glucose analog is first taken up by the cells and then detected and quantified intracellularly using scintillators or photospectrometers, respectively. Since the late 1970s,

radioactive-labeled glucose analogs such as 3H-2DG, 14C-2DG [118], 18F-2DG, and 3H-3-O-methylglucose [162] have dominated the measurement of U_R in cell cultures until recently when these techniques began to phase out due to the development of fluorescent-labeled (e.g., 2-NBDG and 6-NBDG) and unlabeled (2DG) glucose analogs. Although the performance in terms of signal-to-noise ratio and selectivity is inferior to that of radioactive-labeled glucose analogs, the fluorescent-labeled and unlabeled glucose analogs have gained popularity because they require less expensive equipment and avoid the inconveniences of handling and disposal of radioactive materials. Between the fluorescent-labeled and unlabeled glucose analogs, the latter are preferable because the fluorescent-labeled glucose analogs are molecules much larger than glucose and therefore there are concerns as to whether these analogs are transported with a different kinetics by the glucose MTPs. Detailed reviews about all these techniques can be found in [159, 163].

Other methods have emerged which are based on extracellular measurements of glucose, rather than glucose analogs, thus eliminating the doubts and questions that may arise from the cellular uptake of molecules that are not exactly natural, physiological substrates. Among the methods capable of measuring glucose directly, the electrochemical biosensors are considered as highly suitable for extracellular measurement of cellular metabolic activity in cell cultures [164, 165]. Since the studies on cellular metabolic activity have a wide range of applicability, e.g., in cancer, diabetes, mitochondrial disorder, cell and tissue differentiation, cell and tissue storage, cell life cycle, basic cellular processes, and developmental biology, etc., [164, 165] it is of great interest to develop technologies to enable a more mechanistic understanding of the glucose metabolism.

Currently there is one technique called Seahorse Extracellular Flux Analyzer which was specifically designed to simultaneously measure the rates of glycolysis and respiration. While glycolysis and respiration are the major components in the cell energy metabolism, the knowledge of the rates at which these two processes occur is not enough to draw the big picture of the glucose metabolism since the cells may uti-

lize the intracellular glucose for purposes other than energy production, e.g., the glucose can be diverted into processes such as lipogenesis, biosynthesis, and glycogenesis, among others. Therefore, a simple yet powerful model to understand glucose metabolism can be established by acknowledging that at any time point the rate of glucose uptake must be equal to the combination of the rates of all the processes utilizing the intracellular glucose as indicated by Eq. (5.1), where U_R is the glucose uptake rate, G_R is the glycolysis rate, R_R is the respiration rate, and O_R is the addition of the rates of all the other processes utilizing the intracellular glucose.

$$U_R = G_R + R_R + O_R \tag{5.1}$$

The objectives of the research presented here are to experimentally demonstrate that the MEA measures the U_R, and to illustrate how the obtained measurements of U_R combined with measurements of G_R and R_R enable the achievement of a more comprehensive understanding of the glucose metabolism of cultured cells.

5.2 Materials and methods

5.2.1 Reagents

Dulbecco′s phosphate buffered saline pH 7.4 (PBS; cat. no. 14190136) and glycine (cat. no. 405706) were purchased from Thermo Fisher Scientific. D-glucose (cat. no. G5767), glucose oxidase (GOx; cat. no. G2133), o-aminophenol (cat. no. A71301), and tris(hydroxymethyl)aminomethane (TRIS; cat. no. T6066) were purchased from Sigma-Aldrich. Unless stated otherwise, PBS refers to 0.01 M PBS solution.

5.2.2 Cell culture

The three cell lines were prepared and cultured as follows. H69AR (small cell lung cancer, SCLC) cells were obtained from the American Type Culture Collection (ATCC) and cultured as instructed. DDX5-knockdown SCLC (SCLC-KD) cells were

obtained by stably transfecting H69AR cells with an inducible short-hairpin (sh) RNA targeting DDX5 or the non-silencing control shRNA. shRNA expression was induced by adding 1 μg/ml doxycycline to the cells three days before the measurements of glucose uptake rate. The human bronchial epithelial cell line (HBEC) was a gift from Dr. Andrea Kasinski′s Lab at Purdue University and was cultured using the Keratinocyte-SFM media (Gibco, cat. no. 17005042). Cell counting was performed using the trypan blue exclusion method. For measurement of total protein content, the cells were trypsinized, counted, and collected by centrifugation. The cell pellet was then washed with PBS once, lysed using the lysis buffer (Cell Signaling, 9803), and the total protein concentration was measured using the Bradford method.

For experiments, cells were seeded in 12-well plates (Costar 3513) at cell densities of 0.3–1.8$\times10^5$ cells cm^{-2} (HBEC), 1.3–3.5$\times10^5$ cells cm^{-2} (SCLC) and 2.1–2.6$\times10^5$ cells cm^{-2} (SCLC-KD), and incubated in their respective culture media for 24 hours in humidified atmosphere at 37 °C and 5% CO_2 before the measurements of glucose uptake rate. Prior to the measurements of glucose uptake rate, the cells were washed twice with PBS (pH 7.4) at room temperature; next, the culture wells were filled with 1 ml of PBS without glucose and then placed in the measurement apparatus.

5.2.3 Design, fabrication and characterization of microelectrode array

The 1D MEA comprises three electrodes (10 μm × 10 μm) with 280 μm pitch, measured from center to center, meaning that the spatial range for gradient measurements is 560 μm. Electrodes are linearly arranged in the direction perpendicular to the chip edge and designated E1, E2 and E3, where E1 is the closest electrode to the chip edge (distance is typically less than 50 μm). Fabrication process started by depositing an insulating layer (300 nm) of silicon nitride on a silicon substrate using low pressure chemical vapor deposition; followed by evaporation of Ti (10 nm) and Pt (100 nm) using electron beam physical vapor deposition; continued by definition of the electrodes and lead traces using typical photolithography and lift-off

procedures; followed by SU-8 (2 μm thick) coating and definition by photolithography of the exposed Pt surfaces that act as electrodes and contact pads; and finished by dicing the silicon substrate, fixing the dies to printed circuit board (PCB), and wire bonding. Treatment of the electrodes for glucose-selective measurements was accomplished as described in the following four steps. First, platinum black was electrodeposited on the electrodes using reported protocols [81, 166], in order to increase the sensitivity to H_2O_2. Second, the MEA was immersed for 48 hours in a primary amine solution containing 12 mg/ml TRIS and 1 mg/ml glycine in PBS, in order to prevent the binding of GOx on SU-8 during the GOx functionalization step [53, 167]. Third, GOx functionalization was performed by embedding GOx in a poly-o-aminophenol (PoAP) matrix via electropolymerization of the o-aminophenol monomer on the electrode surface, using cyclic voltammetry (0–0.9 V, 2 cycles) in a 0.05 mM acetate buffered (pH 5.0) solution containing 5 mM o-aminophenol and 8 mg/ml GOx. Fourth, the loosely bound GOx was stripped off the PoAP matrix by immersing the MEA for 1–2 hours in a solution of 10 mM glucose in PBS. Electrodes were characterized for glucose response by performing amperometry measurements at 0.5 V in unstirred, air-saturated solutions of PBS at different glucose concentrations. Unless stated otherwise, all the procedures were performed at room temperature, all the electrochemical steps employed three-electrode setups, and all the potentials are referred to the Ag/AgCl (saturated 3 M NaCl) reference electrode.

5.2.4 Apparatus and method to measure glucose uptake rate

Fig. 5.1 illustrates the working principle of the MEA device. The cells in the 2D culture and the glucose-containing liquid medium around the cells constitute an uptake-diffusion system (also called reaction-diffusion system). The uptake of glucose by the cells induces a gradient in the glucose concentration near the cell surface, and this gradient is measured in real time by the MEA which consists of three electrodes positioned within, and aligned with the direction of, the glucose gradient. The

electrodes measure the local glucose concentrations at the electrode positions thus resulting in three concentration–time data sets, each data set having an associated electrode position. Since the positions of the electrodes relative to the cell surface are known, the data of concentration, time and position are used to extract the instantaneous glucose concentration profile, $C(z_i, t)$, where z_i is the position of the i-th electrode and t is the time. The glucose concentration profile is then extrapolated to the cell plane (located at $z = 0$) in order to determine the instantaneous values of glucose gradient, G_S, and glucose concentration, C_S, at the cell surface. According to Fick′s law, the product between G_S and the diffusion coefficient of glucose provides the glucose uptake flux, F_S, which is then normalized to cell density or cell protein content in order to obtain the glucose uptake rate per cell or per unit protein (U_R), respectively.

Glucose concentration was measured by the conventional method based on measurement of the H_2O_2 produced during the oxidation of glucose in presence of GOx and oxygen, wherein the production of H_2O_2 is proportional to the local glucose concentration, provided sufficient GOx and oxygen. Measurement of H_2O_2 was performed amperometrically by the electrooxidation of H_2O_2 at the electrode surface, which was kept at 0.5 V vs. reference electrode, resulting in an electrical current proportional to the local concentration of H_2O_2. Electrodes in the MEA were operated individually using dedicated potentiostats (Reference 600, Gamry Instruments Inc., Warminster, PA) in a three-electrode setup consisting of a shared counter electrode (Pt wire, 0.5 mm diameter) and a shared reference electrode (Ag/AgCl, saturated 3 M NaCl), both purchased from BASI Inc., West Lafayette, IN. Unless stated otherwise, all the experiments were conducted at room temperature and the sampling period of each electrode was 0.5 s.

The measurements of glucose uptake rate were performed in the following sequence of steps. Initially, the culture well containing 1 ml of PBS without glucose was placed in the measurement apparatus which consisted of an inverted microscope and a XYZ motion control system (Applicable Electronics, New Haven, CT) on top of an anti-

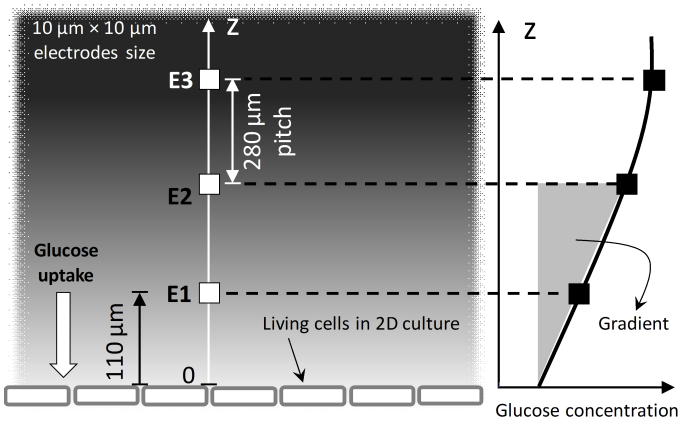

Fig. 5.1. Schematic (not drawn to scale) of uptake-diffusion system and measurement setup illustrating the working principle of the MEA device. The uptake-diffusion system consists of the 2D culture of cells and the glucose-containing medium around the cells. Glucose uptake by the cells induces a gradient in the glucose concentration near the cell surface. The measurement setup consists of a 1D array of electrodes, E1, E2 and E3, aligned in parallel to the z axis and perpendicularly to the cell plane. The electrodes are functionalized with polymer-entrapped glucose oxidase to selectively measure the glucose concentration at the electrode positions over time. The acquired time-dependent data of concentration–position enable the determination of the instantaneous glucose gradient, as illustrated by the gray triangle on the right-hand side.

vibration table. The edge of the MEA chip was positioned at 30 μm from the cell surface using the XYZ motion control system. The electrodes were biased and the amperometric response to just PBS was recorded for 300 s. At 300 seconds, 2 ml of PBS solution containing glucose were added to the culture well to obtain initial glucose concentrations (C_0) of 1, 8 or 15 mM (3 ml total volume), and the chip edge was moved to 5000 μm from the cell surface. The cells began the uptake of glucose and this process induced a dynamic gradient in the glucose concentration near the cell surface. The MEA was kept at 5000 μm until 480 s, time during which the glucose concentration at this position remained equal to the initial value of 1, 8 or 15 mM. At 480 seconds, the chip edge was moved back to 30 μm from the cell surface, and

the electrodes in the MEA started acquiring the relevant concentration data from 484 seconds onwards, since the motion of the MEA chip takes 4 s in either direction. The MEA chip was kept at 30 μm from the cell surface until the end of the experiment. The amperometric signals measured at 300 and 480 seconds and the initial glucose concentrations are used to obtain the blank response and compute the calibration factors for each electrode, as reported elsewhere [18, 133].

5.3 Results and discussion

5.3.1 Reconstruction of concentration profile and extraction of surface concentration and uptake rate

The three steps to determine the glucose uptake rate are illustrated in Fig. 5.2. In the first step, the local glucose concentrations adjacent to the cell surface were quantified via amperometric detection of the H_2O_2 generated by the reaction of glucose with the GOx immobilized at the surface of the MEA electrodes, Fig. 5.2(a). In this sensing scheme the local generation of H_2O_2 is proportional to the local glucose concentration, and the amperometric signal is proportional to the local concentration of H_2O_2. In the second step, the concentrations measured by the three electrodes at any time were plotted against the distance from the cell surface in order to obtain snapshots of the concentration profile at the corresponding time points, Fig. 5.2(b). This is possible because the electrode positions are known. In the third step, the concentration profile was extrapolated to the cell plane in order to extract the surface gradient and the surface concentration. The surface gradient was multiplied by the glucose diffusion coefficient to obtain the glucose uptake flux, and this flux was normalized to the cell density or cell protein content to obtain the glucose uptake rate, Fig. 5.2(c). The measurements of glucose uptake rate were conducted for cultures of HBEC, SCLC and SCLC-KD cells at C_0 = 1, 8 and 15 mM, wherein each C_0 was performed at least by triplicate.

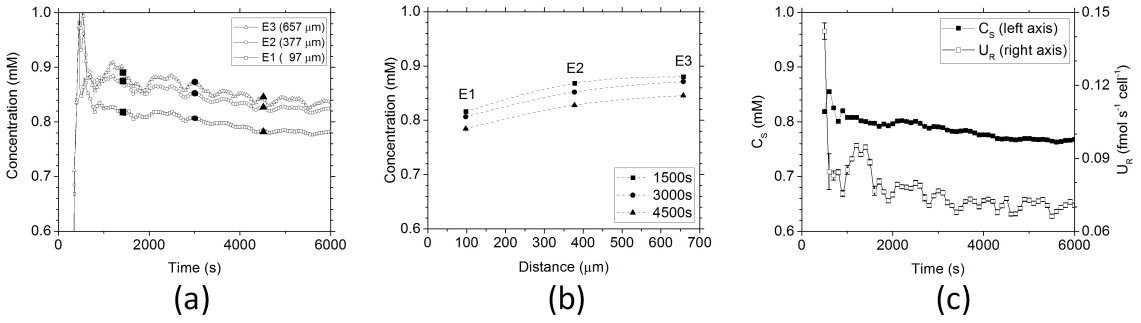

Fig. 5.2. Representative measurements obtained with the MEA electrodes (E1, E2 and E3) for HBEC cells exposed to $C_0 = 1$ mM. (a) Glucose concentrations at the electrode positions as functions of time. Electrode positions with respect to the cell surface ($z = 0$) are indicated in the legend. For clarity, the data symbols are plotted every 50 s but the sampling period during the measurements was 0.5 s. The interval from 0 to 480 s was used to acquire the responses to 0 and 1 mM glucose in order to calibrate the electrodes in situ, and the measurements of local glucose concentrations are performed from 484 s onwards. (b) Reconstruction of the time-dependent glucose concentration profile. For clarity, the concentration profile is plotted only for the three indicated time points. Dashed lines are guide to the eye. (c) C_S and U_R as functions of time. C_S and U_R are extracted via linear extrapolation of the concentration profile, as described in the text. Error bars represent standard error of the linear extrapolation. For clarity, the data symbols are plotted every 100 s. As described in the text, the same measurements were conducted with HBEC, SCLC and SCLC-KD cells exposed to $C_0 = 1$, 8 and 15 mM. No smoothing has been applied to any of the curves.

The data in Fig. 5.2(a) were recorded during exposure of HBEC cells to $C_0 = 1$ mM and have not been smoothed. The sampling period was 0.5 s but, for clarity, the data symbols are plotted every 50 s. At the beginning of the amperometric measurement the MEA is at 30 μm from cell surface. The interval between 0 and 480 s in Fig. 5.2(a) is the time during which the signals are conditioned (0–300 s); the responses to just PBS are acquired (at 300 s); the glucose solution is added to the culture well (301–310 s); the MEA is moved to 5000 μm from the cell surface

(310–314 s); and the in-situ calibration factors are acquired (at 480 s). The initial abrupt increase in the signals corresponds to the rapid homogenization of the glucose concentration throughout the well volume, reaching the intended concentration of 1 mM in approximately 1 min after the addition of the glucose solution. Immediately after the acquisition of the calibration factors at 480 seconds, the MEA is moved back to 30 μm from the cell surface and remains in this position until the end of the experiment. Since the chip motion takes 4 s, the relevant concentration data is acquired from 484 s onwards. It is important to note that at 480 seconds the three signals indicate the same concentration of 1 mM because at that time the chip edge is at 5000 μm from the cell surface and therefore the glucose depletion field, calculated as $6\sqrt{Dt} = 1972$ μm where D $\sim 6{\times}10^{-10}$ m^2 s^{-1} for glucose, has not penetrated that far into the bulk solution. In contrast, when the chip edge is moved from 5000 to 30 μm (between 480 and 484 s) the three signals separate from each other indicating that the three electrodes are measuring different glucose concentrations, as expected. Since E1 and E3 are the closest and furthest electrodes from the cell surface, respectively, the relative magnitudes among the three signals (i.e., E1 $<$ E2 $<$ E3) indicate that the local glucose concentration increases with the distance from the cell surface; this observation is consistent with the presence of a glucose concentration gradient.

The three data sets marked with solid symbols in Fig. 5.2(a) are plotted in Fig. 5.2(b) against the distance from the cell surface in order to visualize snapshots of the concentration profile at the corresponding time points, namely 1500, 3000 and 4500 s. The dashed lines in Fig. 5.2(b) are guides to the eye. It is worth noting that the construction of this plot is possible because the electrode positions relative to the cell surface are known and customizable, and the snapshots of the concentration profile can be reproduced with the same sampling period as the data acquisition (0.5 seconds). Fig. 5.2(b) shows that the concentration profile as a whole decreases with time since at 1500, 3000 and 4500 s the profile ranges between 0.81–0.88 mM, 0.8–0.87 mM, and 0.78–0.85 mM, respectively. Despite this downward shift of the concentration profile, the relative decrease in concentration at each sensor position is

approximately constant over time because the span of those ranges is about the same (∼0.07 mM or ∼1.17 mg/dl), meaning that the induced gradient (or equivalently the uptake rate U_R) is relatively constant over time.

Furthermore, Fig. 5.2(b) shows that the snapshots of the concentration profile are sufficiently close to the cell surface as to determine the glucose concentration and gradient at the cell surface via extrapolation to the cell plane ($z = 0$). Prior work has shown that the concentration profile near a planar active surface (e.g., a planar electrode or a 2D cell culture) is linear at least within 400 μm from the active surface [18, 133]; therefore, the concentration data from electrodes E1 and E2 were used to calculate the surface glucose gradient, G_S, and the linear extrapolation of this gradient to the cell plane was used to determine the concentration at the cell surface, C_S. By virtue of the Fick′s Law, the product of G_S and glucose diffusion coefficient equals the diffusive flux of glucose, F_S, which is a measure of the number of moles of glucose diffusing toward the cells per unit time and per unit area. This flux is normalized to the cell density to obtain the glucose uptake rate per cell, U_R. Fig. 5.2(c) shows C_S and U_R as functions of time using solid and open symbols, respectively. The data in Fig. 5.2(c) have been plotted every 100 s, for clarity, and have not been smoothed. Fig. 5.2(c) shows that the sustained glucose uptake by HBEC cells correlates with a decrease in C_S over the time interval 484–6000 s, which is an expected result according to the physics of irreversible reaction-diffusion systems [18, 133]. Since C_S is equal to C_0 at the onset of glucose exposure, the observed decrease of ∼24% in C_S (i.e., from 1 mM at $t = 480$ s to 0.76 mM at $t = 6000$ s) indicates that the HBEC cells did not exhaust the available glucose.

5.3.2 The U_R transients of HBEC cells exhibit different characteristics depending on glucose concentration

Fig. 5.3 shows U_R as a function of time for various cultures of HBEC cells exposed to $C_0 = 1$, 8 and 15 mM. The temporal resolution of these measurements enables the

observation of the transient behavior of U_R in response to different values of C_0. There are evident characteristics in the U_R transients that seem to be linked to the glucose concentration the cells are exposed to. The first characteristic is the relative steadiness of the U_R at 1 mM which clearly contrasts with the decreasing behaviors of the U_R transients at 8 and 15 mM. The second and more evident characteristic is the increase in the magnitudes of the U_R transients correlated to the increase in glucose concentration. These observations suggest that the cells are able to sense the glucose concentration and then modulate the U_R accordingly, thus leading to the question of whether the glucose uptake is a function of the glucose concentration at the cell surface. This question will be addressed in Section 5.3.5. It is worth noting that the measurements of U_R are consistent among replicates despite the cell densities not being exactly the same from culture to culture (the cell densities in these experiments range between 0.5×10^5 and 0.8×10^5 cells cm^{-2}). The consistency in the measurements of U_R highlights the reliability of the MEA device and indicates that U_R is a physical quantity that conveys information specific to a given cell line at specific conditions, e.g., at specific glucose concentrations.

5.3.3 The glucose uptake of HBEC cells decreases with cell number

One common quantity reported in literature is the glucose uptake, which indicates the number of moles of glucose taken up per cell (or per cell protein mass) over a time period, typically within 5–10 minutes or 1–72 hours depending on whether the glucose is radioactively labeled or non-labeled, respectively. In this study, the glucose uptake is easily calculated by integrating U_R transient with respect to time. Fig. 5.4 shows the glucose uptake by HBEC cells at 6000 s as a function of cell number and for different C_0 values. To facilitate comparison with the literature, the total protein content per cell was determined and the glucose uptake is also indicated in units of μmol (mg protein)$^{-1}$ in the right vertical axis. Fig. 5.4 indicates that glucose uptake increases with glucose concentration, which is predictable since the

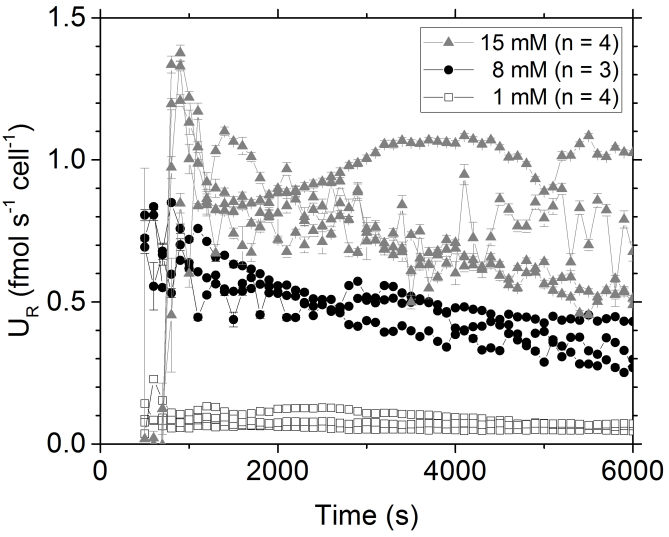

Fig. 5.3. The uptake rate per cell, U_R, as a function of time for experiments where HBEC cells are exposed to C_0 = 1, 8 and 15 mM. Number of replicates is indicated in parentheses, and error bars represent standard error obtained from the linear extrapolation of the data of concentration vs. position for each experiment. For clarity, data points are plotted every 100 s. No smoothing has been applied to the data. Cell densities in these experiments range between 0.5×10^5 and 0.8×10^5 cells cm^{-2}. There are characteristics in the U_R transients that seemingly depend on the glucose concentration since at 1 mM the U_R is relatively constant whereas at 8 and 15 mM the U_R transients decrease with time. Also, the magnitudes of the U_R transients increase with the glucose concentration within the investigated time window. U_R transients were also obtained for SCLC and SCLC-KD cells, as discussed in the text.

magnitude of the U_R transient also increases with glucose concentration, as shown in Fig. 5.3. Moreover, Fig. 5.4 indicates that the glucose uptake per cell decreases with cell number and reaches a plateau for cell numbers greater than (2–3)$\times10^5$ cells per well, for the three investigated glucose concentrations (1, 8 and 15 mM). In general, a relative increase of 94% in cell number (from 1.69×10^5 to 3.28×10^5 cells per well) leads to a relative decrease of 77 $\pm$ 6 % in the glucose uptake, as evaluated after 6000 s of exposure to the stated glucose concentrations. Consistent with the literature, a similar decrease in the glucose uptake per cell correlated to an increase in cell number

has also been observed in HBEC cells previously [168]. It is worth noting that Fig. 5.4 can also be interpreted in terms of cell density by simply normalizing the cell numbers to the culture area (3.8 cm^2). In this regard, (2–3)$\times 10^5$ cells per well corresponds to (0.5–0.8)$\times 10^5$ cells cm^{-2}. Assuming that the described behavior of HBEC cells extrapolates to SCLC and SCLC-KD cells, the experiments with SCLC and SCLC-KD cells were conducted at comparable confluency; however, to accomplish this the cell numbers of SCLC and SCLC-KD had to be increased by 3$\times$ since the SCLC and SCLC-KD cells are three times smaller than the HBEC cells. From now on the analysis focuses only on the high cell density regime.

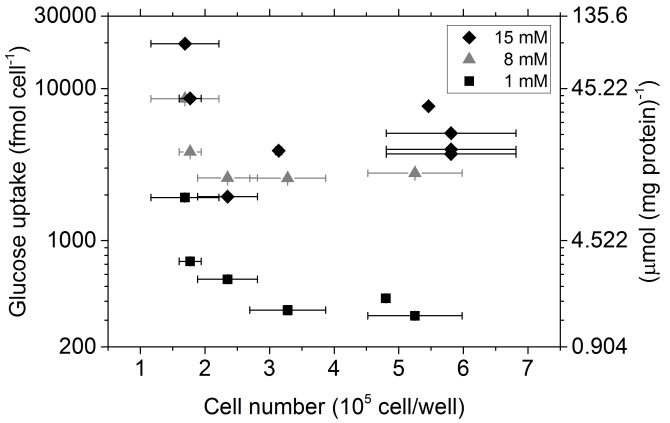

Fig. 5.4. The glucose uptake per cell at 6000 s as a function of cell number. Glucose uptake is obtained by integrating U_R with respect to the time up to 6000 s, for experiments with HBEC cells at various cell densities and exposed to $C_0 = 1$, 8 and 15 mM. The right vertical axis indicates the glucose uptake in units of μmol (mg protein)$^{-1}$ to facilitate comparison with the literature. The culture area for all the experiments is 3.8 cm^2. For the three glucose concentrations, the glucose uptake per cell decreases with cell number and reaches a plateau for cell numbers greater than (2–3)$\times 10^5$ cells per well.

5.3.4 The U_R transients of HBEC, SCLC and SCLC-KD cells

Fig. 5.5 shows the U_R transients of HBEC, SCLC and SCLC-KD cells for various C_0 values. There are five key points to note from Fig. 5.5. First, Fig. 5.5 indicates that the magnitudes of the U_R transients for the three cell lines are within the same order of magnitude at a given C_0 value, which implies that the magnitudes of the U_R transients of SCLC and SCLC-KD also increase with glucose concentration, similarly to the behavior of HBEC cells (Fig. 5.3). Second, Fig. 5.5(a) shows that the U_R transients of HBEC and SCLC-KD cells at 1 mM glucose slightly decrease within the initial 2000 seconds but become relatively stable afterwards. In contrast, the U_R transient of SCLC increases with time over the investigated time window. In quantitative terms, the U_R of the three cell lines are similar (within 0.06–0.12 fmol s^{-1} $cell^{-1}$) at initial stages of the experiment but evolve until the U_R of SCLC is about 3 times that of HBEC or SCLC-KD, at the end of the experiment. Third, Fig. 5.5(b) shows that over the investigated time window the U_R transients of HBEC and SCLC-KD at 8 mM glucose decrease with time while that of SCLC increases with time. Quantitatively, the U_R of HBEC and SCLC-KD cells is about 3 times that of SCLC at initial stages of the experiment but evolve until the U_R of the three cell lines converge to within 0.2-0.5 fmol s^{-1} $cell^{-1}$ at the end of the experiment. Fourth, Fig. 5.5(c) shows that within error bars there is a slight overall increase in the magnitudes of the U_R transients at 15 mM glucose for the three cell lines as compared to the respective magnitudes in Fig. 5.5(b). The error bars in Fig. 5.5(c) were not minimized, even after conducting more replicates at $C_0 = 15$ mM, and therefore the results are shown anyway since no reason was found to discard these data. Separate experiments were performed to confirm that the sensors are stable at 15 mM glucose over the investigated time window. Other separate experiments using human brain cells (data not shown) also show the data at 15 mM glucose exhibit larger error bars than the data at lower concentrations, thus suggesting that the large error bars at 15 mM glucose arise from variations in the cell behavior; however, determining the

underlying reason for those variations in cell behavior is out of the scope of this study. Fifth, and most importantly, Fig. 5.5(a) and Fig. 5.5(b) show that the U_R transients of HBEC and SCLC-KD cells resemble each other qualitative and quantitatively, but sharply contrast with the U_R transients of SCLC cells.

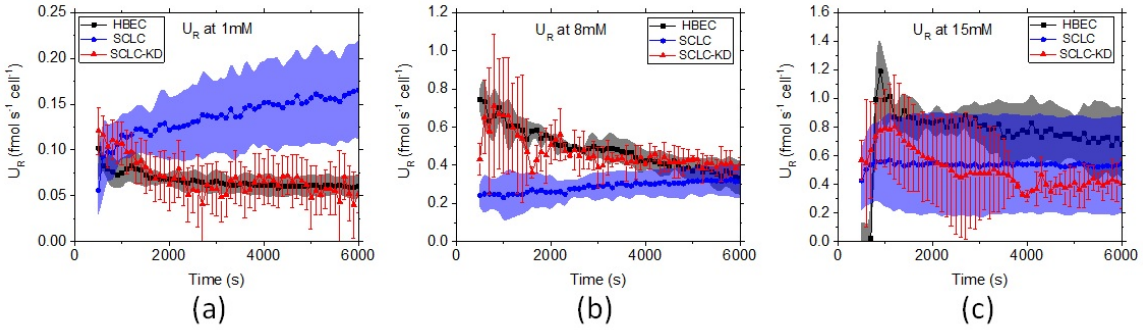

Fig. 5.5. The U_R transients of HBEC, SCLC and SCLC-KD cells for various C_0 values: (a) $C_0 = 1$ mM; (b) $C_0 = 8$ mM; (c) $C_0 = 15$ mM. For clarity, data points are shown every 100 s and a mixture of shaded bands and error bars are used to indicate the standard deviation of the mean value of U_R from replicates (at least $n = 3$ for each curve). It is clear that at 1 and 8 mM the U_R transients of HBEC and SCLC-KD cells practically agree to each other while clearly differ from the U_R transients of SCLC cells.

The resemblance between HBEC and SCLC-KD cells and the dissimilarity of these two cell lines with respect to SCLC cells is an important observation that can be discussed in terms of the relative content of DDX5 protein among the three cell lines and the role of DDX5 in the cellular glucose metabolism [169]. HBEC cells are non-cancerous human bronchial epithelial cells, in which DDX5 protein levels are below detection [170]. H69AR (i.e., SCLC) cells are chemoresistant small-cell lung cancer cells that overexpress DDX5 [170]. H69AR cells were stably transfected with an inducible shRNA targeting DDX5 (shDDX5) or a control shRNA (shCtr) in order to generate two genetically modified cell lines. The cells expressing shDDX5 (i.e., the SCLC-KD cells) exhibited successful depletion of the DDX5 protein [170]. H69AR

is the chemoresistant variant of H69, which is a cell line derived from one small cell lung cancer patient. Small cell lung cancers are thought to have neuroendocrine origin, whereas HBEC are just bronchial epithelial cells with no neuroendocrine origin; HBEC is just a commonly used control cell line for lung cancer studies. DDX5 is a DEAD-box RNA helicase that functions as Ribonucleoprotein (RNP) chaperones in vivo. DDX5 is required for the anchorage-independent growth of SCLC cells, which is a hallmark of cancer [170]. Therefore, DDX5-depleted H69AR (i.e. SCLC-KD) cells may phenotypically resemble the non-cancerous HBEC cells, which is consistent with the resemblance between the U_R transients of HBEC and SCLC-KD, as shown in Fig. 5.5(a-b).

5.3.5 The U_R as a function of C_S and extraction of kinetic mechanisms

Fig. 5.6 shows the U_R as a function of C_S, as observed at the initial and final stages of the experiments and for the three investigated cell lines. The initial and final stages are defined as the 500-second intervals from 1000 to 1500 s and from 5500 to 6000 s, as indicated in the legends, and U_R and C_S are averaged over these intervals to reduce the effects of noise in the data. To describe the mechanisms of glucose uptake kinetics, linear expressions (Eq. (5.2)) were fitted to the data of HBEC and SCLC cells due to their visible degree of linearity, whereas a Michaelis-Menten expression (Eq. (5.3)) was fitted to the data of SCLC-KD cells due to their visible signs of saturation. In Eq. (5.2) and (5.3), k_F is the slope of the linear fit, U_0 is the vertical-axis intercept, U_{SAT} is the saturation uptake rate and K_M is the Michaelis-Menten constant. The values of these kinetic parameters as obtained from the data in Fig. 5.6 are summarized in Table 5.1.

$$U_R = k_F C_S + U_0 \tag{5.2}$$

$$U_R = \frac{U_{SAT} C_S}{K_M + C_S} \tag{5.3}$$

Table 5.1.
Kinetic parameters extracted from experimental data.

	k_F (10^{-15} L s^{-1} cell^{-1})	U_0 (amol s^{-1} cell^{-1})
HBEC	72 ± 9	16 ± 20
SCLC	25 ± 16	104 ± 29
	U_{SAT} (amol s^{-1} cell^{-1})	K_M (mM)
SCLC-KD	1314 ± 214	9.3 ± 2.9

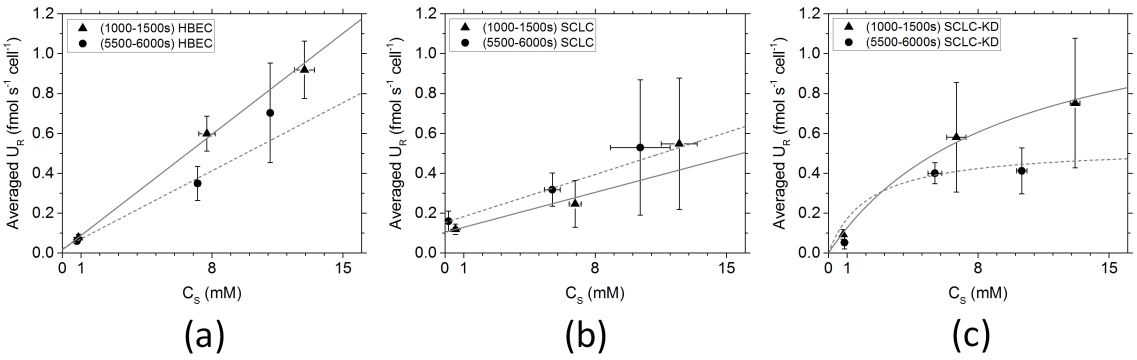

Fig. 5.6. The U_R as a function of C_S at initial and final stages of the experiments for (a) HBEC cells, (b) SCLC cells, and (c) SCLC-KD cells. The U_R is averaged over the 500-second intervals indicated in the legends and plotted versus the C_S averaged over the same intervals. Error bars indicate the standard deviation of the mean value of U_R and C_S as obtained from the averaging over the 500-second intervals. Solid and dashed lines are fitted curves for the data at the initial (1000-1500 s) and final (5500-6000 s) stages of the experiments, respectively.

5.3.6 A more comprehensive picture of glucose metabolism over time based on U_R, G_R and R_R

As indicated by Eq. (5.1), a more comprehensive account of glucose metabolism can be obtained when the measurements of glucose uptake rate (U_R) are complemented with measurements of glycolysis rate (G_R) and respiration rate (R_R). Cur-

rently there is one method, called Seahorse Extracellular Flux Analyzer, capable of measuring simultaneously both variables (G_R and R_R) as functions of time and in high-throughput configurations, including 24 and 96 well plates. The Seahorse method uses two optical sensors per well, one sensor is sensitive to oxygen and the other is sensitive to protons (i.e., pH), and these sensors are lowered or raised relative to the well bottom by a built-in motion control system. When the sensors are lowered, the sensors embodiment gets into contact with the walls of the culture well thus creating a transient microchamber with a volume of just 7 μL and the sensors being located at 200 μm from the well bottom. The volume inside the microchamber is so small that any decrease in oxygen and increase in H^+ concentrations is captured by the corresponding optical sensor. The changes in O_2 and H^+ concentrations are monitored over an user-specified time window in order to compute the oxygen consumption rate (OCR_{TOT}, in units of pmol min^{-1}) and the extracellular acidification rate ($ECAR_{TOT}$, in units of mpH min^{-1}), and these values of OCR_{TOT} and $ECAR_{TOT}$ are reported to the user as functions of time in a log file.

The oxygen inside the cell is consumed by respiration in the mitochondria and other processes in the cytoplasm, and therefore the OCR_{TOT} must be split into mitochondrial and non-mitochondrial components; the mitochondrial component corresponds to R_R. To accomplish these, the OCR_{TOT} must be measured with and without the presence of rotenone and myxothiazol, which are two drugs that act to suppress the respiration in the mitochondria. Therefore, R_R can be computed from experimental data obtained by the Seahorse using Eq. (5.4), where OCR_{TOT} and $OCR_{non-mito}$ are the OCR measured in the absence and presence of rotenone and myxothiazol, respectively.

$$R_R = OCR_{TOT} - OCR_{non-mito} \tag{5.4}$$

The acidification rate, also called proton production rate, has at least two major components, one is due to lactic acid production and the other is due to CO_2 production during respiration in the mitochondria, as indicated by the Eq. (5.5) for

ionization of lactic acid into lactate ion and Eq. (5.6) for ionization of CO_2 into bicarbonate ion. The proton production rate due to the ionization of lactic acid into lactate corresponds to G_R. Therefore, to compute the G_R from experimental data obtained from the Seahorse, the component due to bicarbonate ions must be subtracted from the total ECAR, $ECAR_{TOT}$, as indicated in Eq. (5.7) [171], where BC is the buffering capacity of the medium, max H^+/O_2 is the maximum ratio of proton production for full respiration of glucose, pH is the pH of the medium, and pK_1 is the pK_a of carbonic acid. In the experiments performed in this work, $BC = 3.85$ mM pH^{-1}, $pH = 7.4$, $pK_1 = 6.2$, and $max H^+/O_2$ is 1 for full respiration of glucose.

$$C_3H_6O_3 \xrightarrow{\text{aqueous solution}} CH_3CH(OH)CO_2{}^- + H^+ \tag{5.5}$$

$$CO_2 + H_2O \longrightarrow H_2CO_3 \longrightarrow HCO_3{}^- + H^+ \tag{5.6}$$

$$G_R = ECAR_{TOT} \cdot BC \cdot 7\mu L - (OCR_{TOT} - OCR_{non-mito}) \left(max \frac{H^+}{O_2} \right) \left(\frac{10^{pH-pK_1}}{1 + 10^{pH-pK_1}} \right) \tag{5.7}$$

Fig. 5.7 show the addition of the transients of G_R and R_R for the three cell lines at $C_0 = 1$, 8 and 15 mM, as measured by the Seahorse XF24 flux analyzer. These results indicate that $G_R + R_R$ is roughly constant at 0.2 ± 0.1 fmol s^{-1} $cell^{-1}$ over the investigated time window (6000 s) and regardless of the glucose concentration. Comparison of the results in Figures 5.5 with 5.7 suggests that the cells are utilizing a constant, conservative amount of glucose to sustain the energy metabolism while the majority of the glucose is diverted to other processes. While additional measurements will be required to elucidate the identities and contributions of those processes, it is clear that the complementary quality of the measurements of U_R, G_R and R_R paves the way toward a more comprehensive picture of glucose metabolism over time.

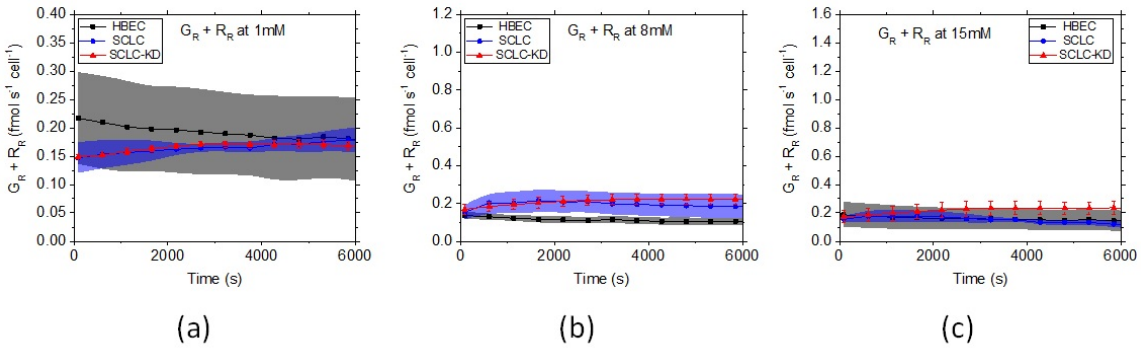

Fig. 5.7. The combined transients of the glycolysis and respiration rates, $G_R + R_R$, for the three cell lines at $C_0 = 1$, 8 and 15 mM, as measured by the Seahorse XF24 flux analyzer.

5.4 Conclusions

This work presented the design and development of a microelectrode array to measure transient gradients and concentrations of glucose at the surface of cells in 2D culture in order to gain a more mechanistic understanding of the glucose uptake kinetics. The measurements of glucose uptake rate were complemented with measurements of glycolysis and respiration rates to offer a more comprehensive picture of the glucose metabolism of the investigated cell lines.

5.5 Acknowledgements

The author acknowledges the collaboration received from Prof. Elizabeth J. Tran (Department of Biochemistry, Purdue University) and her Postdoctoral Researcher Dr. Zheng (Cindy) Xing (Department of Biochemistry, Purdue University) regarding the gift and growth of the three cell lines, the biochemical assays, the measurements of glycolytic and respiration rates using Seahorse flux analyzer, and their insightful comments and discussions. The author also acknowledges the collaboration with

Siddarth Sridharan to share the design/fabrication of the MEAs, and the insightful comments, discussions and guidance provided by Prof. David B. Janes.

6. SUMMARY OF CONTRIBUTION

6.1 Contribution of the thesis

To date it is well-known that living organisms like the human being are extremely complex reaction-transport systems. In the average human body, each of the $\sim 3.72 \times 10^{13}$ cells [172] exchanges molecules with the immediate microenvironment through processes that are governed by chemical, geometrical and physical factors such as the nature and kinetics of the chemical reactions, the size and shape of the compartments where the reactions occur, the transport mechanisms by which the reacting species come across each other, and the spatiotemporal distribution of the reacting species. Accordingly, the experimental models employed in biological studies should be analyzed in terms of reaction-transport systems, particularly 2D/3D cultures of adherent cells should be treated as reaction-diffusion systems since the transport of species to and from these cells is dominated by diffusion, both in the actual living organism and in the in-vitro model.

While the theoretical fundamentals of reaction-diffusion systems [173–175] were established more than four decades ago, the reaction-diffusion paradigm is not widely utilized by the biological community, partly because the analytical platforms to collect the relevant data are not fully developed and validated, and partly because this new paradigm is itself more complex and laborious [97]. Despite the vast technological development seen in the last two decades, each technology still has challenges preventing the direct application in the reaction-diffusion paradigm, and most importantly, the paradigm shift is more likely to occur only if the benefits outweigh the extra effort. Therefore, the contribution of this dissertation is briefly described by the following two points. First, the challenges of electrochemical sensors have been identified and those challenges that will enable the development of technological platforms

have been addressed, thus facilitating the embrace of the reaction-diffusion paradigm in biological studies. Second, a technological platform has been developed, validated and demonstrated in actual physiological settings by acquiring biological data with aggregated value, as compared to the conventional methods, thereby justifying the extra effort.

The following sections elaborate on each point.

6.1.1 Brief perspective of the state of the art

On the one hand, only a few reports on 1D MEAs existed [34, 176–179] wherein the functionality in physiological and non-physiological settings was demonstrated but without using amperometry. On the other hand, the literature has contained numerous reports on 2D MEAs demonstrating a variety of electrochemical techniques, including amperometry, in both physiological and non-physiological settings but without addressing the main theme of this thesis, i.e., the acquisition of reliable measurements of fast transient concentration gradients using amperometry in the typical concentration scales of physiological studies. Amperometry offers unmatched temporal resolution, routinely in the sub-millisecond time scale [19] and limited just by the circuitry, but at the expense of high instability and irreproducibility of the signals (in particular for H_2O_2 at platinum [27]) thus preventing the acquisition of accurate concentration values. More reproducible, stable signals for H_2O_2 can be obtained with carbon electrodes but at the expense of reduced sensitivity [28] and less compatibility with microfabrication technology. Although stable, reproducible signals are highly desirable, the low sensitivity of carbon electrodes makes it difficult to resolve the tiny changes in concentration that occur between adjacent sensors, thereby preventing the measurement of the gradient.

The best available methods to measure fast transient concentration gradients are the scanning electrochemical spectroscopy (SECM) and the self-referencing vibration probe (SRT), both based on a movable probe tip acting as an amperometric sensor. In

particular, SRT was pushed to the limit by demonstrating measurements of biological fluxes (i.e., biologically originated gradients) with a vibration frequency of 0.2–0.5 Hz [13], meaning that the maximum temporal resolution of the gradient measurement was 2 seconds. Therefore, the main theme of this thesis (i.e., sub-second measurements) had not been addressed yet.

In summary, while the technological and theoretical components to accomplish the objectives of this thesis existed already, they had not been integrated into a suitable platform, the reliability of such platform had not been benchmarked against well-defined transient gradients (non-physiological and physiological), and the platform had not been validated by acquiring biological data with aggregated value, as compared to the available methods. Therefore, these are the gaps in the literature being filled by the realization of this thesis.

6.1.2 Challenges, development and benchmarking of the MEA

The work presented in this thesis is the logical progression of preceding ideas, namely SRT technique and 1D MEAs. While combining these two ideas was conceptually straightforward, there were a number of problems that had to be addressed before the 1D MEA platform technology could deliver on its promise.

Theoretical and simulation analyses have suggested that the amperometric signal of an electrode with a radius smaller than 25 μm reaches quickly ($<$ 1 s) a steady value when exposed to a constant uniform concentration of the analyte of interest. It turned out to be just an ideality. This ideal behavior has been observed only in experiments using well-defined redox couples. The problem here is that the analyte of interest, H_2O_2, does not constitute a well-defined redox couple with O_2, in other words, the electrooxidation of H_2O_2 is irreversible [26,27]. Compounding the problem is the fact that the interface between the chemical phases of platinum and H_2O_2/PBS exhibits multiple physicochemical processes occurring simultaneously, thus rendering this interface extremely complicated [28–32]. Therefore, the very electrochemistry at

the interface between platinum and H_2O_2/PBS is a challenge itself for the development of sensors suitable for gradient measurements.

While it is true that sensitivity variability is inherent to the electrochemical sensors, this issue is exacerbated in the case of electrooxidation of H_2O_2 at platinum electrodes. The reason for this is again the very complicated properties of the interface between platinum and H_2O_2/PBS. In fact, after attempting experiments in more complex media in comparison to PBS (e.g., DMEM, RPMI, etc.), the signals were even worst since the aminoacids and other components of those typical cell culture media easily adsorb on the platinum surface thus competing for the reaction sites along with the H_2O_2. Therefore, the decision was to perform all the experiments in just PBS because solving this problem of biofouling is altogether another PhD research project. The literature indicates that the biofouling can be partially eliminated by depositing membranes on top of the platinum surface; however, this strategy is detrimental to the response time of the sensor since the analyte molecules must diffuse throughout the membranes. Therefore, membrane deposition was kept at the minimum necessary.

The sensitivity variability manifested itself in four types: variations during an experiment (also known as signal drift), variations from experiment to experiment, variations from electrode to electrode in an MEA, and variations from MEA to MEA. All these sensitivity variations act to deteriorate the analytical power of the signals and therefore an incredible effort was made here to elaborate a comprehensive set of strategies, including the development of the in-situ transient calibration, to minimize the effect of those variations. The success of the developed strategies was demonstrated experimentally by using the large sink electrode to generate well-defined, controllable gradients. Those gradients are described with a high degree of certainty using the well-known physics of reaction-diffusion systems. As a result, the demonstration of the measurement of various transient concentration gradients, including sub-second gradients, was successfully accomplished. In fact, the four-cycle potential pattern that was applied to the large sink electrode was intended to be a analytical

challenge to the MEA device, due to the small changes in concentration that were expected from cycle to cycle; however, the MEA device proved to be robust and powerful enough to distinguish those small changes, as obtained from a dimensionless analysis.

Overall, in the work described so far the interest and the effort was focused on making sure that the MEA provides reliable concentration data during the measurement of gradients having a variety of spatial and temporal scales.

6.1.3 Validation in actual physiological setting

Once the acquisition of reliable concentration data was demonstrated, even in challenging scenarios, the next goal was to demonstrate that the technology provides information of greater analytical value as compared to the preceding paradigms. To accomplish this, human astrocytes and human glioblastoma multiforme cells were used. These two cell lines served as the physiological benchmark since it was previously known, at least by a few scientists, that the kinetics of H_2O_2 uptake rate in rat astrocytes and rat C6 glioma cells was non-linear [117] and therefore it was reasonable to expect a similar kinetic mechanism in the human counterparts. The data collected with the developed MEA platform is emphatic at exposing the non-linearity between the H_2O_2 uptake rate and the concentration of H_2O_2 at the cell surface, thereby fulfilling the promise of providing biological data with aggregated value.

However, the capability of elucidating kinetic mechanisms is just one, possibly the most important, feature that aggregates value to the acquired data. Other features that are highly desired by the bio-community and therefore aggregate value as well include the capability to acquire functional data (i.e., the capability to measure a variable continuously over time), the access facilitation to important metabolic variables, and the capability for high-throughput assaying (i.e., the capability to read multiple culture wells simultaneously). Remarkably, the developed MEA platform provide all of the above features, and although the high-throughput feature was not demon-

strated here, it is not unfeasible. In particular, the capabilities to acquire functional data and to facilitate the access to important metabolic variables were demonstrated by the experiments with astrocytes and glioblastoma cells, wherein the functional data correspond to the variables of H_2O_2 uptake rate and surface concentration both as functions of time, and the metabolic variable corresponds to the H_2O_2 uptake rate.

6.1.4 MEA measurements of glucose uptake rate contribute to the achievement of a more comprehensive picture of glucose metabolism of cultured cells

There are few available methods to continuously measure rates of metabolic processes. The Seahorse flux analyzer is the only one available that has the capability to continuously measure the rates of glycolysis and respiration of cultured cells. While glycolysis and respiration are two major processes in glucose metabolism, they are not the only ones utilizing the intracellular glucose at any given time and under any given condition. Therefore, the relevance of glycolysis and respiration relative to the global glucose metabolism can only be known if the global rate of glucose uptake is known.

Once validated against well-characterized non-physiological and physiological reaction-diffusion systems, the MEA technology platform was used to measure the glucose uptake rate of cells from the human pulmonary tract, including cancerous, non-cancerous and genetically modified cancerous cells, aiming at acquiring a more comprehensive picture of the glucose metabolism in these cell lines. These measurements were complemented with measurements of glycolysis and respiration rates using the Seahorse flux analyzer, finding that glycolysis and respiration account for the totality of the uptaken glucose at low glucose concentration (i.e., at ~ 1 mM) but become less relevant at higher glucose concentrations (i.e., at ~ 8 and ~ 15 mM), accounting just for less than 40% of the uptaken glucose. This result is remarkable since, as a rule of

thumb, glycolysis and respiration are typically assumed to be the dominant processes in glucose metabolism.

Finally, since the cancerous cells employed in the study (i.e., the small-cell lung cancer cells) are poorly characterized in the literature despite being highly aggressive and metastatic, it is likely that results directly comparable to those obtained here are not reported in the literature yet, meaning that the MEA platform has being used here to acquire brand new biological data with aggregated value.

6.2 List of publications and conferences

6.2.1 Journal articles

1. Sridharan SV, Rivera JF, Nolan JK, Alam MA, Rickus JL, Janes DB, *"On-chip microelectrode array and in situ transient calibration for measurement of transient concentration gradients near surfaces of 2D cell cultures"*, Sensors and Actuators B: Chemical, 2018 May 1, 260:519–528.

2. Rivera JF, Sridharan SV, Nolan JK, Miloro SA, Alam MA, Rickus JL, Janes DB, *"Real-time characterization of uptake kinetics of glioblastoma vs. astrocytes in 2D cell culture using microelectrode array"*, Analyst, 2018; 143(20):4954–4966.

6.2.2 Conference participation

1. Rivera, J. F., Sridharan S. V., Janes, D. B., Rickus J. L., "Electrochemical Sensor Electrode Arrays for Flux or Gradient Measurements of Glucose," 57th Electronic Materials Conference, 2015.

2. James Nolan, Jose F. Rivera, Siddarth V. Sridharan, Leyla Kahyaoglu, Rajtarun Madangopal, Bruce Hope, David Janes, Jenna Rickus, "Bio-functionalization

and modeling of microsensors for on chip single cell extracellular flux and intracellular biocatalysis", Biosensors 2016, 25–27 May 2016, Gothenburg, Sweden.

3. Siddarth V. Sridharan, Jose F. Rivera, Xin Jin, David B. Janes, Jenna L. Rickus and Muhammad A. Alam, "Electrochemical Micro-Electrode Arrays for Measurement of Transient Concentration Gradients of Hydrogen Peroxide", Device Research Conference 2016.

4. Siddarth V. Sridharan, Jose F. Rivera, James Nolan, David B. Janes and Jenna L. Rickus, "Surface Functionalization Approaches for Quantitative Sensing of Bioanalytes using Amperometric Micro-Electrode Arrays," 59th Electronic Materials Conference, 2017.

5. Jose F. Rivera, Siddarth V. Sridharan, James Nolan, David B. Janes and Jenna L. Rickus, "Implications of using high reaction rate amperometric microelectrode array for measurement of local concentration variations of bioanalytes," 59th Electronic Materials Conference, 2017.

6. Kriscovich, H.R., Libring, S.M., Sridharan, S.V., Nolan, J.K., Rivera, J.F., Rickus, J.L. and Janes, D.B., "Measurement of Hydrogen Peroxide Influx into Cells: Preparation For Measurement Using On-Chip Microelectrode Array," The Summer Undergraduate Research Fellowship (SURF) Symposium. Paper 65, August 4, 2016, West Lafayette, Indiana, USA.

7. Libring, S.M., Kriscovich, H.R., Nolan, J.K., Sridharan, S.V., Rivera, J.F., Janes, D.B. and Rickus, J.L., "Cellular Model of Hydrogen Peroxide Release: In Preparation for On-Chip Sensor Measurements," The Summer Undergraduate Research Fellowship (SURF) Symposium. Paper 71, August 4, 2016, West Lafayette, Indiana, USA.

REFERENCES

REFERENCES

[1] C. C. Winterbourn, "Reconciling the chemistry and biology of reactive oxygen species," *Nature chemical biology*, vol. 4, no. 5, p. 278, 2008.

[2] N. Baltes, L. Thouin, C. Amatore, and J. Heinze, "Imaging concentration profiles of redox-active species with nanometric amperometric probes: Effect of natural convection on transport at microdisk electrodes," *Angewandte Chemie International Edition*, vol. 43, no. 11, pp. 1431–1435, 2004.

[3] P. Sun, F. O. Laforge, and M. V. Mirkin, "Scanning electrochemical microscopy in the 21st century," *Physical Chemistry Chemical Physics*, vol. 9, no. 7, pp. 802–823, 2007.

[4] S. Amemiya, A. J. Bard, F.-R. F. Fan, M. V. Mirkin, and P. R. Unwin, "Scanning electrochemical microscopy," *Annu. Rev. Anal. Chem.*, vol. 1, pp. 95–131, 2008.

[5] T. Sun, Y. Yu, B. J. Zacher, and M. V. Mirkin, "Scanning electrochemical microscopy of individual catalytic nanoparticles," *Angewandte Chemie International Edition*, vol. 53, no. 51, pp. 14 120–14 123, 2014.

[6] R. Chen, K. Hu, Y. Yu, M. V. Mirkin, and S. Amemiya, "Focused-ion-beam-milled carbon nanoelectrodes for scanning electrochemical microscopy," *Journal of The Electrochemical Society*, vol. 163, no. 4, pp. H3032–H3037, 2016.

[7] L. F. Jaffe and R. Nuccitelli, "An Ultrasensitive Vibrating Probe for Measuring Steady Extracellular Currents," *J Cell Biol*, vol. 63, no. 2, pp. 614–628, nov 1974. [Online]. Available: http://jcb.rupress.org/content/63/2/614

[8] W. M. Kühtreiber and L. F. Jaffe, "Detection of extracellular calcium gradients with a calcium-specific vibrating electrode." *The Journal of cell biology*, vol. 110, no. 5, pp. 1565–1573, 1990.

[9] S.-K. Jung, J. R. Trimarchi, R. H. Sanger, and P. J. Smith, "Development and application of a self-referencing glucose microsensor for the measurement of glucose consumption by pancreatic β-cells," *Analytical chemistry*, vol. 73, no. 15, pp. 3759–3767, 2001.

[10] D. M. Porterfield, "Measuring metabolism and biophysical flux in the tissue, cellular and sub-cellular domains: {Recent} developments in self-referencing amperometry for physiological sensing," *Biosensors and Bioelectronics*, vol. 22, no. 7, pp. 1186–1196, feb 2007. [Online]. Available: http://www.sciencedirect.com/science/article/pii/S0956566306002740

[11] J. Shi, E. S. McLamore, D. Jaroch, J. C. Claussen, R. G. Mirmira, J. L. Rickus, and D. M. Porterfield, "Oscillatory glucose flux in ins 1 pancreatic β cells: A self-referencing microbiosensor study," *Analytical biochemistry*, vol. 411, no. 2, pp. 185–193, 2011.

[12] E. McLamore, J. Shi, D. Jaroch, J. Claussen, A. Uchida, Y. Jiang, W. Zhang, S. Donkin, M. Banks, K. Buhman, D. Teegarden, J. Rickus, and D. Porterfield, "A self referencing platinum nanoparticle decorated enzyme-based microbiosensor for real time measurement of physiological glucose transport," *Biosensors and Bioelectronics*, vol. 26, no. 5, pp. 2237 – 2245, 2011. [Online]. Available: http://www.sciencedirect.com/science/article/pii/S095656631000655X

[13] E. S. McLamore, S. Mohanty, J. Shi, J. Claussen, S. S. Jedlicka, J. L. Rickus, and D. M. Porterfield, "A self-referencing glutamate biosensor for measuring real time neuronal glutamate flux," *Journal of Neuroscience Methods*, vol. 189, no. 1, pp. 14–22, may 2010. [Online]. Available: http://www.sciencedirect.com/science/article/pii/S0165027010001196

[14] X. Liu, M. M. Ramsey, X. Chen, D. Koley, M. Whiteley, and A. J. Bard, "Real-time mapping of a hydrogen peroxide concentration profile across a polymicrobial bacterial biofilm using scanning electrochemical microscopy," *PNAS*, vol. 108, no. 7, pp. 2668–2673, feb 2011. [Online]. Available: http://www.pnas.org/content/108/7/2668

[15] E. Polo and S. Kruss, "Nanosensors for neurotransmitters," *Analytical and bioanalytical chemistry*, vol. 408, no. 11, pp. 2727–2741, 2016.

[16] S. Kruss, D. P. Salem, L. Vuković, B. Lima, E. Vander Ende, E. S. Boyden, and M. S. Strano, "High-resolution imaging of cellular dopamine efflux using a fluorescent nanosensor array," *Proceedings of the National Academy of Sciences*, p. 201613541, 2017.

[17] S. M. Oja, Y. Fan, C. M. Armstrong, P. Defnet, and B. Zhang, "Nanoscale electrochemistry revisited," *Analytical Chemistry*, vol. 88, no. 1, pp. 414–430, 2016, pMID: 26630546. [Online]. Available: http://dx.doi.org/10.1021/acs.analchem.5b04542

[18] J. F. Rivera, S. V. Sridharan, J. K. Nolan, S. A. Miloro, M. A. Alam, J. L. Rickus, and D. B. Janes, "Real-time characterization of uptake kinetics of glioblastoma vs. astrocytes in 2d cell culture using microelectrode array," *Analyst*, vol. 143, no. 20, pp. 4954–4966, 2018.

[19] E. R. Travis and R. M. Wightman, "Spatio-temporal resolution of exocytosis from individual cells," *Annual review of biophysics and biomolecular structure*, vol. 27, no. 1, pp. 77–103, 1998.

[20] A. J. Berger, I. Itzkan, and M. S. Feld, "Feasibility of measuring blood glucose concentration by near-infrared raman spectroscopy," *Spectrochimica Acta Part A: Molecular and Biomolecular Spectroscopy*, vol. 53, no. 2, pp. 287–292, 1997.

[21] G. Perea and A. Araque, "Astrocytes potentiate transmitter release at single hippocampal synapses," *Science*, vol. 317, no. 5841, pp. 1083–1086, 2007.

[22] D. J. Michael and R. M. Wightman, "Electrochemical monitoring of biogenic amine neurotransmission in real time," *Journal of pharmaceutical and biomedical analysis*, vol. 19, no. 1, pp. 33–46, 1999.

[23] S. Moussa and J. Mauzeroll, "Microelectrodes: An overview of probe development and bioelectrochemistry applications from 2013 to 2018," *Journal of The Electrochemical Society*, vol. 166, no. 6, pp. G25–G38, 2019.

[24] A. J. Bard and L. R. Faulkner, *Electrochemical Methods: Fundamentals and Applications*. Wiley, 2000. [Online]. Available: https://books.google.com/books?id=kv56QgAACAAJ

[25] C. G. Zoski, *Handbook of electrochemistry*. Elsevier, 2006.

[26] Y. Zhang and G. S. Wilson, "Electrochemical oxidation of h2o2 on pt and pt+ ir electrodes in physiological buffer and its applicability to h2o2-based biosensors," *Journal of Electroanalytical Chemistry*, vol. 345, no. 1-2, pp. 253–271, 1993.

[27] S. A. Evans, J. M. Elliott, L. M. Andrews, P. N. Bartlett, P. J. Doyle, and G. Denuault, "Detection of hydrogen peroxide at mesoporous platinum microelectrodes," *Analytical Chemistry*, vol. 74, no. 6, pp. 1322–1326, 2002.

[28] S. B. Hall, E. A. Khudaish, and A. L. Hart, "Electrochemical oxidation of hydrogen peroxide at platinum electrodes. part i. an adsorption-controlled mechanism," *Electrochimica Acta*, vol. 43, no. 5-6, pp. 579–588, 1998.

[29] ——, "Electrochemical oxidation of hydrogen peroxide at platinum electrodes. part ii: effect of potential," *Electrochimica Acta*, vol. 43, no. 14-15, pp. 2015–2024, 1998.

[30] ——, "Electrochemical oxidation of hydrogen peroxide at platinum electrodes. part iii: Effect of temperature," *Electrochimica Acta*, vol. 44, no. 14, pp. 2455–2462, 1999.

[31] ——, "Electrochemical oxidation of hydrogen peroxide at platinum electrodes. part iv: phosphate buffer dependence," *Electrochimica Acta*, vol. 44, no. 25, pp. 4573–4582, 1999.

[32] ——, "Electrochemical oxidation of hydrogen peroxide at platinum electrodes. part v: inhibition by chloride," *Electrochimica Acta*, vol. 45, no. 21, pp. 3573–3579, 2000.

[33] H. Meyer, H. Drewer, B. Gruendig, K. Cammann, R. Kakerow, Y. Manoli, W. Mokwa, and M. Rospert, "Two-dimensional imaging of o2, h2o2, and glucose distributions by an array of 400 individually addressable microelectrodes," *Analytical Chemistry*, vol. 67, no. 7, pp. 1164–1170, 1995.

[34] S.-Y. Liu, Y.-P. Chen, F. Fang, J. Xu, G.-P. Sheng, H.-Q. Yu, G. Liu, and Y.-C. Tian, "Measurement of dissolved oxygen and its diffusivity in aerobic granules using a lithographically-fabricated microelectrode array," *Environmental Science & Technology*, vol. 43, no. 4, pp. 1160–1165, 2009. [Online]. Available: https://doi.org/10.1021/es802662e

[35] K. Y. Inoue, M. Matsudaira, R. Kubo, M. Nakano, S. Yoshida, S. Matsuzaki, A. Suda, R. Kunikata, T. Kimura, R. Tsurumi *et al.*, "Lsi-based amperometric sensor for bio-imaging and multi-point biosensing," *Lab on a Chip*, vol. 12, no. 18, pp. 3481–3490, 2012.

[36] J. B. Wydallis, R. M. Feeny, W. Wilson, T. Kern, T. Chen, S. Tobet, M. M. Reynolds, and C. S. Henry, "Spatiotemporal norepinephrine mapping using a high-density cmos microelectrode array," *Lab on a Chip*, vol. 15, no. 20, pp. 4075–4082, 2015.

[37] B. N. Kim, A. D. Herbst, S. J. Kim, B. A. Minch, and M. Lindau, "Parallel recording of neurotransmitters release from chromaffin cells using a 10× 10 cmos ic potentiostat array with on-chip working electrodes," *Biosensors and Bioelectronics*, vol. 41, pp. 736–744, 2013.

[38] J. Rothe, M. Lewandowska, F. Heer, O. Frey, and A. Hierlemann, "Multi-target electrochemical biosensing enabled by integrated cmos electronics," *Journal of Micromechanics and Microengineering*, vol. 21, no. 5, p. 054010, 2011.

[39] J. Rothe, O. Frey, A. Stettler, Y. Chen, and A. Hierlemann, "Fully integrated cmos microsystem for electrochemical measurements on 32× 32 working electrodes at 90 frames per second," *Analytical chemistry*, vol. 86, no. 13, pp. 6425–6432, 2014.

[40] J. Wang, R. Trouillon, J. Dunevall, and A. G. Ewing, "Spatial resolution of single-cell exocytosis by microwell-based individually addressable thin film ultramicroelectrode arrays," *Analytical chemistry*, vol. 86, no. 9, pp. 4515–4520, 2014.

[41] J. Wigström, J. Dunevall, N. Najafinobar, J. Lovrić, J. Wang, A. G. Ewing, and A.-S. Cans, "Lithographic microfabrication of a 16-electrode array on a probe tip for high spatial resolution electrochemical localization of exocytosis," *Analytical chemistry*, vol. 88, no. 4, pp. 2080–2087, 2016.

[42] J. Yan, V. A. Pedrosa, J. Enomoto, A. L. Simonian, and A. Revzin, "Electrochemical biosensors for on-chip detection of oxidative stress from immune cells," *Biomicrofluidics*, vol. 5, no. 3, p. 032008, 2011.

[43] M. Şen, K. Ino, K. Y. Inoue, T. Arai, T. Nishijo, A. Suda, R. Kunikata, H. Shiku, and T. Matsue, "Lsi-based amperometric sensor for real-time monitoring of embryoid bodies," *Biosensors and Bioelectronics*, vol. 48, pp. 12–18, 2013.

[44] J. Wang, R. Trouillon, Y. Lin, M. I. Svensson, and A. G. Ewing, "Individually addressable thin-film ultramicroelectrode array for spatial measurements of single vesicle release," *Analytical chemistry*, vol. 85, no. 11, pp. 5600–5608, 2013.

[45] H. Abe, K. Ino, C.-Z. Li, Y. Kanno, K. Y. Inoue, A. Suda, R. Kunikata, M. Matsudaira, Y. Takahashi, H. Shiku *et al.*, "Electrochemical imaging of dopamine release from three-dimensional-cultured pc12 cells using large-scale integration-based amperometric sensors," *Analytical chemistry*, vol. 87, no. 12, pp. 6364–6370, 2015.

[46] C. Amatore, J. Delacotte, M. Guille-Collignon, and F. Lemaître, "Vesicular exocytosis and microdevices–microelectrode arrays," *Analyst*, vol. 140, no. 11, pp. 3687–3695, 2015.

[47] C. F. Lourenço, A. Ledo, J. Laranjinha, G. A. Gerhardt, and R. M. Barbosa, "Microelectrode array biosensor for high-resolution measurements of extracellular glucose in the brain," *Sensors and Actuators B: Chemical*, vol. 237, pp. 298–307, 2016.

[48] F. Picollo, A. Battiato, E. Bernardi, A. Marcantoni, A. Pasquarelli, E. Carbone, P. Olivero, and V. Carabelli, "Microelectrode arrays of diamond-insulated graphitic channels for real-time detection of exocytotic events from cultured chromaffin cells and slices of adrenal glands," *Analytical chemistry*, vol. 88, no. 15, pp. 7493–7499, 2016.

[49] W. Tedjo, J. Nejad, R. Feeny, L. Yang, C. Henry, T. Stuart, and T. Chen, "Electrochemical biosensor system using a cmos microelectrode array provides high spatially and temporally resolved images," *Biosensors and Bioelectronics*, vol. 114, pp. 78–88, 2018.

[50] S. R. Belding, E. I. Rogers, and R. G. Compton, "Potential step chronoamperometry at microdisc electrodes: effect of finite electrode kinetics," *The Journal of Physical Chemistry C*, vol. 113, no. 10, pp. 4202–4207, 2009.

[51] N. G. Poulos, J. R. Hall, and M. C. Leopold, "Functional layer-by-layer design of xerogel-based first-generation amperometric glucose biosensors," *Langmuir*, vol. 31, no. 4, pp. 1547–1555, 2015.

[52] C. F. Lourenço, A. Ledo, J. Laranjinha, G. A. Gerhardt, and R. M. Barbosa, "Microelectrode array biosensor for high-resolution measurements of extracellular glucose in the brain," *Sensors and Actuators B: Chemical*, vol. 237, pp. 298–307, 2016.

[53] N. Thomas, I. Lähdesmäki, and B. Parviz, "Direct immobilization of enzymes on common photoresists," in *2011 IEEE 24th International Conference on Micro Electro Mechanical Systems*. IEEE, 2011, pp. 233–236.

[54] J. Galceran, J. Monné, J. Puy, and H. P. van Leeuwen, "The impact of the transient uptake flux on bioaccumulation: Linear adsorption and first-order internalisation coupled with spherical semi-infinite mass transport," *Marine chemistry*, vol. 85, no. 1, pp. 89–102, 2004.

[55] D. Ellison, A. Mugler, M. D. Brennan, S. H. Lee, R. J. Huebner, E. R. Shamir, L. A. Woo, J. Kim, P. Amar, I. Nemenman, A. J. Ewald, and A. Levchenko, "Cell-cell communication enhances the capacity of cell ensembles to sense shallow gradients during morphogenesis," *Proc Natl Acad Sci U S A*, vol. 113, no. 6, pp. E679–E688, feb 2016. [Online]. Available: http://www.ncbi.nlm.nih.gov/pmc/articles/PMC4760786/

[56] S. Alberghini, E. Polone, V. Corich, M. Carlot, F. Seno, A. Trovato, and A. Squartini, "Consequences of relative cellular positioning on quorum sensing and bacterial cell-to-cell communication," *FEMS Microbiology Letters*, vol. 292, no. 2, pp. 149–161, mar 2009. [Online]. Available: http://onlinelibrary.wiley.com/doi/10.1111/j.1574-6968.2008.01478.x/abstract

[57] B. J. Kim and M. Wu, "Microfluidics for mammalian cell chemotaxis," *Annals of Biomedical Engineering*, vol. 40, no. 6, pp. 1316–1327, 2012.

[58] T. M. Keenan and A. Folch, "Biomolecular gradients in cell culture systems," *Lab Chip*, vol. 8, no. 1, pp. 34–57, dec 2007. [Online]. Available: http://pubs.rsc.org/en/content/articlelanding/2008/lc/b711887b

[59] A. G. G. Toh, Z. P. Wang, C. Yang, and N.-T. Nguyen, "Engineering microfluidic concentration gradient generators for biological applications," *Microfluidics and Nanofluidics*, vol. 16, no. 1, pp. 1–18, Jan 2014. [Online]. Available: https://doi.org/10.1007/s10404-013-1236-3

[60] S. Kim, H. J. Kim, and N. L. Jeon, "Biological applications of microfluidic gradient devices," *Integrative Biology*, vol. 2, no. 11-12, pp. 584–603, 2010.

[61] S. Desagher, J. Glowinski, and J. Premont, "Astrocytes protect neurons from hydrogen peroxide toxicity," *Journal of Neuroscience*, vol. 16, no. 8, pp. 2553–2562, 1996.

[62] B. A. Wagner, J. R. Witmer, T. J. van't Erve, and G. R. Buettner, "An assay for the rate of removal of extracellular hydrogen peroxide by cells," *Redox Biology*, vol. 1, no. 1, pp. 210–217, 2013. [Online]. Available: http://www.sciencedirect.com/science/article/pii/S2213231713000323

[63] A. Bagulho, F. Vilas-Boas, A. Pena, C. Peneda, F. C. Santos, A. Jerónimo, R. F. M. de Almeida, and C. Real, "The extracellular matrix modulates H_2O_2 degradation and redox signaling in endothelial cells," *Redox Biology*, vol. 6, pp. 454–460, dec 2015. [Online]. Available: http://www.sciencedirect.com/science/article/pii/S2213231715001172

[64] H. S. Marinho, L. Cyrne, E. Cadenas, and F. Antunes, "H_2O_2 Delivery to Cells," *Methods in Enzymology*, vol. 526, pp. 159 – 173, 2013, hydrogen Peroxide and Cell Signaling, Part A. [Online]. Available: http://www.sciencedirect.com/science/article/pii/B9780124058835000107

[65] L. M. Kauri, S.-K. Jung, and R. T. Kennedy, "Direct measurement of glucose gradients and mass transport within islets of langerhans," *Biochemical and biophysical research communications*, vol. 304, no. 2, pp. 371–377, 2003.

[66] Q. Wu, M. E. Reith, R. M. Wightman, K. T. Kawagoe, and P. A. Garris, "Determination of release and uptake parameters from electrically evoked dopamine dynamics measured by real-time voltammetry," *Journal of neuroscience methods*, vol. 112, no. 2, pp. 119–133, 2001.

[67] C. F. Ng, F. Q. Schafer, G. R. Buettner, and V. Rodgers, "The rate of cellular hydrogen peroxide removal shows dependency on gsh: mathematical insight into in vivo h2o2 and gpx concentrations," *Free radical research*, vol. 41, no. 11, pp. 1201–1211, 2007.

[68] S. H. Walters, I. M. Taylor, Z. Shu, and A. C. Michael, "A novel restricted diffusion model of evoked dopamine," *ACS chemical neuroscience*, vol. 5, no. 9, pp. 776–783, 2014.

[69] A. I. Oleinick, C. Amatore, M. Guille, S. Arbault, O. V. Klymenko, and I. Svir, "Modelling release of nitric oxide in a slice of rat's brain: describing stimulated functional hyperemia with diffusion-reaction equations," *Mathematical Medicine and Biology*, vol. 23, no. 1, pp. 27–44, 2006.

[70] C. Amatore, A. Chovin, P. Garrigue, L. Servant, N. Sojic, S. Szunerits, and L. Thouin, "Remote {Fluorescence} {Imaging} of {Dynamic} {Concentration} {Profiles} with {Micrometer} {Resolution} {Using} a {Coherent} {Optical} {Fiber} {Bundle}," *Analytical Chemistry*, vol. 76, no. 24, pp. 7202–7210, dec 2004. [Online]. Available: http://pubs.acs.org/doi/abs/10.1021/ac049017g

[71] S. G. Rhee, T.-S. Chang, W. Jeong, and D. Kang, "Methods for detection and measurement of hydrogen peroxide inside and outside of cells," *Molecules and cells*, vol. 29, no. 6, pp. 539–549, 2010.

[72] D. M. H. Kern, "The Polarography and Standard Potential of the Oxygen-Hydrogen Peroxide Couple," *J. Am. Chem. Soc.*, vol. 76, no. 16, pp. 4208–4214, aug 1954. [Online]. Available: http://dx.doi.org/10.1021/ja01645a059

[73] C. Amatore, S. Arbault, D. Bruce, P. de Oliveira, M. Erard, and M. Vuillaume, "Analysis of individual biochemical events based on artificial synapses using ultramicroelectrodes: cellular oxidative burst," *Faraday Discuss.*, vol. 116, no. 0, pp. 319–333, jan 2000. [Online]. Available: http://pubs.rsc.org/en/content/articlelanding/2000/fd/b001448f

[74] C. Amatore, S. Arbault, D. Bruce, P. De Oliveira, M. Erard, N. Sojic, and M. Vuillaume, "Nitrogen monoxide and oxidative stress: composition and intensity of cellular oxidative bursts cocktail. a study through artificial electrochemical synapses on single human fibroblasts," *Analusis*, vol. 28, no. 6, pp. 506–517, 2000.

[75] C. Amatore, S. Arbault, C. Bouton, K. Coffi, J.-C. Drapier, H. Ghandour, and Y. Tong, "Monitoring in real time with a microelectrode the release of reactive oxygen and nitrogen species by a single macrophage stimulated by its membrane mechanical depolarization," *ChemBioChem*, vol. 7, no. 4, pp. 653–661, 2006.

[76] V. Folmer, N. Pedroso, A. C. Matias, S. C. Lopes, F. Antunes, L. Cyrne, and H. S. Marinho, "H 2 o 2 induces rapid biophysical and permeability changes in the plasma membrane of saccharomyces cerevisiae," *Biochimica et Biophysica Acta (BBA)-Biomembranes*, vol. 1778, no. 4, pp. 1141–1147, 2008.

[77] D. Erudaitius, A. Huang, S. Kazmi, G. R. Buettner, and V. G. Rodgers, "Peroxiporin expression is an important factor for cancer cell susceptibility to therapeutic h2o2: Implications for pharmacological ascorbate therapy," *PloS one*, vol. 12, no. 1, p. e0170442, 2017.

[78] D. Suazo-Dávila, J. Rivera-Meléndez, J. Koehne, M. Meyyappan, and C. R. Cabrera, "Surface analysis and electrochemistry of a robust carbon-nanofiber-based electrode platform h2o2 sensor," *Applied Surface Science*, vol. 384, no. Supplement C, pp. 251 – 257, 2016. [Online]. Available: http://www.sciencedirect.com/science/article/pii/S0169433216310339

[79] B. I. Rosario-Castro, E. J. Contés-de Jesús, M. Lebrón-Colón, M. A. Meador, M. A. Scibioh, and C. R. Cabrera, "Single-wall carbon nanotube chemical attachment at platinum electrodes," *Applied Surface Science*, vol. 257, no. 2, pp. 340–353, 2010.

[80] B. Day, F. Pomerleau, J. Burmeister, P. Huettl, and G. Gerhardt, "Microelectrode array studies of basal and potassium-evoked release of l-glutamate in the anesthetized rat brain," *Journal of neurochemistry*, vol. 96, no. 6, pp. 1626–1635, 2006.

[81] R. Madangopal, M. Stensberg, M. Porterfield, J. Rickus, and N. Pulliam, "Directed enzyme deposition via electroactive polymer-based nanomaterials for multi-analyte amperometric biosensors," in *2012 IEEE Sensors*, Oct 2012, pp. 1–4.

[82] H. Sies, "Hydrogen peroxide as a central redox signaling molecule in physiological oxidative stress: oxidative eustress," *Redox biology*, 2017.

[83] S. S. Jedlicka, M. Dadarlat, T. Hassell, Y. Lin, A. Young, M. Zhang, P. Irazoqui, and J. L. Rickus, "Calibration of neurotransmitter release from neural cells for therapeutic implants," *International journal of neural systems*, vol. 19, no. 03, pp. 197–212, 2009.

[84] P. Nair and M. Alam, "Performance limits of nanobiosensors," *Applied physics letters*, vol. 88, no. 23, p. 233120, 2006.

[85] A. J. Bard, L. R. Faulkner *et al.*, *Fundamentals and applications*. Wiley New York, 2001, vol. 2.

[86] L. Rajendran, "Modelling of reaction–diffusion processes: the theory of catalytic electrode processes at hemispheroidal ultramicroelectrodes," *Electrochemistry communications*, vol. 2, no. 10, pp. 679–684, 2000.

[87] S. Loghambal and L. Rajendran, "Mathematical modeling of diffusion and kinetics in amperometric immobilized enzyme electrodes," *Electrochimica Acta*, vol. 55, no. 18, pp. 5230–5238, 2010.

[88] P. R. Nair and M. A. Alam, "A compact analytical formalism for current transients in electrochemical systems," *Analyst*, vol. 138, pp. 525–538, 2013. [Online]. Available: http://dx.doi.org/10.1039/C2AN35346F

[89] R. C. Engstrom, M. Weber, D. J. Wunder, R. Burgess, and S. Winquist, "Measurements within the diffusion layer using a microelectrode probe," *Anal. Chem.*, vol. 58, no. 4, pp. 844–848, apr 1986. [Online]. Available: http://pubs.acs.org/doi/abs/10.1021/ac00295a044

[90] A. C. von Eschenbach, "A vision for the national cancer program in the united states," *Nature Reviews Cancer*, vol. 4, no. 10, p. 820, 2004.

[91] H. J. Forman, "Use and abuse of exogenous h2o2 in studies of signal transduction," *Free Radical Biology and Medicine*, vol. 42, no. 7, pp. 926–932, 2007.

[92] B. C. Dickinson and C. J. Chang, "Chemistry and biology of reactive oxygen species in signaling or stress responses," *Nature chemical biology*, vol. 7, no. 8, p. 504, 2011.

[93] H. S. Marinho, C. Real, L. Cyrne, H. Soares, and F. Antunes, ""Hydrogen peroxide sensing, signaling and regulation of transcription factors"," *Redox Biology*, vol. 2, pp. 535 – 562, 2014. [Online]. Available: http://www.sciencedirect.com/science/article/pii/S2213231714000457

[94] F. Antunes and P. M. Brito, "Quantitative biology of hydrogen peroxide signaling," *Redox biology*, vol. 13, pp. 1–7, 2017.

[95] H. Link, D. Christodoulou, and U. Sauer, "Advancing metabolic models with kinetic information," *Current opinion in biotechnology*, vol. 29, pp. 8–14, 2014.

[96] R. Benfeitas, M. Uhlen, J. Nielsen, and A. Mardinoglu, "New challenges to study heterogeneity in cancer redox metabolism," *Frontiers in cell and developmental biology*, vol. 5, p. 65, 2017.

[97] A. L. Paguirigan and D. J. Beebe, "Microfluidics meet cell biology: bridging the gap by validation and application of microscale techniques for cell biological assays," *BioEssays*, vol. 30, no. 9, pp. 811–821, 2008.

[98] H. Yu, I. Meyvantsson, I. A. Shkel, and D. J. Beebe, "Diffusion dependent cell behavior in microenvironments," *Lab on a Chip*, vol. 5, no. 10, pp. 1089–1095, 2005.

[99] F. Guo, J. B. French, P. Li, H. Zhao, C. Y. Chan, J. R. Fick, S. J. Benkovic, and T. J. Huang, "Probing cell–cell communication with microfluidic devices," *Lab on a Chip*, vol. 13, no. 16, pp. 3152–3162, 2013.

[100] B. P. Dranka, G. A. Benavides, A. R. Diers, S. Giordano, B. R. Zelickson, C. Reily, L. Zou, J. C. Chatham, B. G. Hill, J. Zhang *et al.*, "Assessing bioenergetic function in response to oxidative stress by metabolic profiling," *Free Radical Biology and Medicine*, vol. 51, no. 9, pp. 1621–1635, 2011.

[101] B. Chance, H. Sies, and A. Boveris, "Hydroperoxide metabolism in mammalian organs." *Physiological reviews*, vol. 59, no. 3, pp. 527–605, 1979.

[102] J. R. Stone and S. Yang, "Hydrogen peroxide: a signaling messenger," *Antioxidants & redox signaling*, vol. 8, no. 3-4, pp. 243–270, 2006.

[103] M. Gülden, A. Jess, J. Kammann, E. Maser, and H. Seibert, "Cytotoxic potency of h2o2 in cell cultures: impact of cell concentration and exposure time," *Free Radical Biology and Medicine*, vol. 49, no. 8, pp. 1298–1305, 2010.

[104] C. Röhl, E. Armbrust, E. Herbst, A. Jess, M. Gülden, E. Maser, G. Rimbach, and C. Bösch-Saadatmandi, "Mechanisms involved in the modulation of astroglial resistance to oxidative stress induced by activated microglia: antioxidative systems, peroxide elimination, radical generation, lipid peroxidation," *Neurotoxicity research*, vol. 17, no. 4, pp. 317–331, 2010.

[105] K. J. Barnham, C. L. Masters, and A. I. Bush, "Neurodegenerative diseases and oxidative stress," *Nature reviews Drug discovery*, vol. 3, no. 3, p. 205, 2004.

[106] L. C. Seaver and J. A. Imlay, "Hydrogen {Peroxide} {Fluxes} and {Compartmentalization} inside {Growing} {Escherichia} coli," *J. Bacteriol.*, vol. 183, no. 24, pp. 7182–7189, dec 2001. [Online]. Available: http://jb.asm.org/content/183/24/7182

[107] L. E. Tomalin, A. M. Day, Z. E. Underwood, G. R. Smith, P. Dalle Pezze, C. Rallis, W. Patel, B. C. Dickinson, J. Bähler, T. F. Brewer *et al.*, "Increasing extracellular h2o2 produces a bi-phasic response in intracellular h2o2, with peroxiredoxin hyperoxidation only triggered once the cellular h2o2-buffering capacity is overwhelmed," *Free Radical Biology and Medicine*, vol. 95, pp. 333–348, 2016.

[108] S. Desagher, J. Glowinski, and J. Prémont, "Pyruvate protects neurons against hydrogen peroxide-induced toxicity," *Journal of Neuroscience*, vol. 17, no. 23, pp. 9060–9067, 1997.

[109] F. Antunes and E. Cadenas, "Estimation of {H}2O2 gradients across biomembranes," *FEBS Letters*, vol. 475, no. 2, pp. 121–126, jun 2000. [Online]. Available: http://www.sciencedirect.com/science/article/pii/S0014579300016380

[110] R. Dringen, P. G. Pawlowski, and J. Hirrlinger, "Peroxide detoxification by brain cells," *Journal of neuroscience research*, vol. 79, no. 1-2, pp. 157–165, 2005.

[111] B. K. Huang and H. D. Sikes, "Quantifying intracellular hydrogen peroxide perturbations in terms of concentration," *Redox biology*, vol. 2, pp. 955–962, 2014.

[112] C. M. Doskey, V. Buranasudja, B. A. Wagner, J. G. Wilkes, J. Du, J. J. Cullen, and G. R. Buettner, "Tumor cells have decreased ability to metabolize h2o2: Implications for pharmacological ascorbate in cancer therapy," *Redox biology*, vol. 10, pp. 274–284, 2016.

[113] N. Makino, Y. Mochizuki, S. Bannai, and Y. Sugita, "Kinetic studies on the removal of extracellular hydrogen peroxide by cultured fibroblasts." *Journal of Biological Chemistry*, vol. 269, no. 2, pp. 1020–1025, 1994.

[114] K. Sasaki, S. Bannai, and N. Makino, "Kinetics of hydrogen peroxide elimination by human umbilical vein endothelial cells in culture," *Biochimica et Biophysica Acta (BBA)-General Subjects*, vol. 1380, no. 2, pp. 275–288, 1998.

[115] K. Hashida, Y. Sakakura, and N. Makino, "Kinetic studies on the hydrogen peroxide elimination by cultured pc12 cells: rate limitation by glucose-6-phosphate dehydrogenase," *Biochimica et Biophysica Acta (BBA)-General Subjects*, vol. 1572, no. 1, pp. 85–90, 2002.

[116] N. Makino, K. Sasaki, K. Hashida, and Y. Sakakura, "A metabolic model describing the h2o2 elimination by mammalian cells including h2o2 permeation through cytoplasmic and peroxisomal membranes: comparison with experimental data," *Biochimica et Biophysica Acta (BBA)-General Subjects*, vol. 1673, no. 3, pp. 149–159, 2004.

[117] N. Makino, T. Mise, and J.-i. Sagara, "Kinetics of hydrogen peroxide elimination by astrocytes and c6 glioma cells: analysis based on a mathematical model," *Biochimica et Biophysica Acta (BBA)-General Subjects*, vol. 1780, no. 6, pp. 927–936, 2008.

[118] L. Sokoloff, M. Reivich, C. Kennedy, M. D. Rosiers, C. Patlak, K. e. a. Pettigrew, O. Sakurada, and M. Shinohara, "The [14c] deoxyglucose method for

the measurement of local cerebral glucose utilization: theory, procedure, and normal values in the conscious and anesthetized albino rat 1," *Journal of neurochemistry*, vol. 28, no. 5, pp. 897–916, 1977.

[119] Y. Chen, N. E. Vartiainen, W. Ying, P. H. Chan, J. Koistinaho, and R. A. Swanson, "Astrocytes protect neurons from nitric oxide toxicity by a glutathione-dependent mechanism," *Journal of neurochemistry*, vol. 77, no. 6, pp. 1601–1610, 2001.

[120] A. Y. Shih, D. A. Johnson, G. Wong, A. D. Kraft, L. Jiang, H. Erb, J. A. Johnson, and T. H. Murphy, "Coordinate regulation of glutathione biosynthesis and release by nrf2-expressing glia potently protects neurons from oxidative stress," *Journal of Neuroscience*, vol. 23, no. 8, pp. 3394–3406, 2003.

[121] Y. Jiang and L. Uhrbom, "On the origin of glioma," *Upsala journal of medical sciences*, vol. 117, no. 2, pp. 113–121, 2012.

[122] M. C. Papadopoulos and A. S. Verkman, "Aquaporin water channels in the nervous system," *Nature Reviews Neuroscience*, vol. 14, no. 4, p. 265, 2013.

[123] A. Salazar-Ramiro, D. Ramírez-Ortega, V. Pérez de la Cruz, N. Y. Hérnandez-Pedro, D. F. González-Esquivel, J. Sotelo, and B. Pineda, "Role of redox status in development of glioblastoma," *Frontiers in immunology*, vol. 7, p. 156, 2016.

[124] M. Rinaldi, M. Caffo, L. Minutoli, H. Marini, R. V. Abbritti, F. Squadrito, V. Trichilo, A. Valenti, V. Barresi, D. Altavilla, M. Passalacqua, and G. Caruso, "Ros and brain gliomas: An overview of potential and innovative therapeutic strategies," *International Journal of Molecular Sciences*, vol. 17, no. 6, p. 984, 2016. [Online]. Available: http://www.mdpi.com/1422-0067/17/6/984

[125] D. Trachootham, J. Alexandre, and P. Huang, "Targeting cancer cells by ros-mediated mechanisms: a radical therapeutic approach?" *Nature Reviews Drug Discovery*, vol. 8, pp. 579–591, 2009.

[126] C. M. Cabello, G. Wondrak *et al.*, "Experimental therapeutics: targeting the redox achilles heel of cancer." *Current opinion in investigational drugs (London, England: 2000)*, vol. 8, no. 12, pp. 1022–1037, 2007.

[127] S. Rodic and M. D. Vincent, "Reactive oxygen species (ros) are a key determinant of cancer's metabolic phenotype," *International Journal of Cancer*, vol. 142, no. 3, pp. 440–448, 2018. [Online]. Available: https://onlinelibrary.wiley.com/doi/abs/10.1002/ijc.31069

[128] M. B. Grisham, "Methods to detect hydrogen peroxide in living cells: Possibilities and pitfalls," *Comparative Biochemistry and Physiology Part A: Molecular & Integrative Physiology*, vol. 165, no. 4, pp. 429 – 438, 2013, first International Conference on Oxidative Stress in Aquatic Ecosystems. [Online]. Available: http://www.sciencedirect.com/science/article/pii/S1095643313000330

[129] H. Guo, H. Aleyasin, B. C. Dickinson, R. E. Haskew-Layton, and R. R. Ratan, "Recent advances in hydrogen peroxide imaging for biological applications," *Cell & Bioscience*, vol. 4, no. 1, p. 64, Oct 2014. [Online]. Available: https://doi.org/10.1186/2045-3701-4-64

[130] C. C. Winterbourn, "The challenges of using fluorescent probes to detect and quantify specific reactive oxygen species in living cells," *Biochimica et Biophysica Acta (BBA) - General Subjects*, vol. 1840, no. 2, pp. 730 – 738, 2014, current methods to study reactive oxygen species - pros and cons. [Online]. Available: http://www.sciencedirect.com/science/article/pii/S0304416513002006

[131] D. Dębski, R. Smulik, J. Zielonka, B. Michałowski, M. Jakubowska, K. Dębowska, J. Adamus, A. Marcinek, B. Kalyanaraman, and A. Sikora, "Mechanism of oxidative conversion of amplexÂő red to resorufin: Pulse radiolysis and enzymatic studies," *Free Radical Biology and Medicine*, vol. 95, pp. 323 – 332, 2016. [Online]. Available: http://www.sciencedirect.com/science/article/pii/S0891584916300065

[132] P. Lefrancois, V. S. R. Vajrala, I. B. Arredondo, B. Goudeau, T. Doneux, L. Bouffier, and S. Arbault, "Direct oxidative pathway from amplex red to resorufin revealed by in situ confocal imaging," *Phys. Chem. Chem. Phys.*, vol. 18, pp. 25 817–25 822, 2016. [Online]. Available: http://dx.doi.org/10.1039/C6CP04438G

[133] S. V. Sridharan, J. F. Rivera, J. K. Nolan, M. A. Alam, J. L. Rickus, and D. B. Janes, "On-chip microelectrode array and in situ transient calibration for measurement of transient concentration gradients near surfaces of 2d cell cultures," *Sensors and Actuators B: Chemical*, vol. 260, pp. 519 – 528, 2018. [Online]. Available: http://www.sciencedirect.com/science/article/pii/S0925400517325303

[134] M. G. Sullivan, H. Utomo, P. J. Fagan, and M. D. Ward, "Automated electrochemical analysis with combinatorial electrode arrays," *Analytical Chemistry*, vol. 71, no. 19, pp. 4369–4375, 1999, pMID: 21662862. [Online]. Available: https://doi.org/10.1021/ac990331y

[135] X. Xu, S. Zhang, H. Chen, and J. Kong, "Integration of electrochemistry in micro-total analysis systems for biochemical assays: Recent developments," *Talanta*, vol. 80, no. 1, pp. 8 – 18, 2009. [Online]. Available: http://www.sciencedirect.com/science/article/pii/S0039914009004615

[136] J. R. Liddell, C. Zwingmann, M. M. Schmidt, A. Thiessen, D. Leibfritz, S. R. Robinson, and R. Dringen, "Sustained hydrogen peroxide stress decreases lactate production by cultured astrocytes," *Journal of neuroscience research*, vol. 87, no. 12, pp. 2696–2708, 2009.

[137] T. P. Szatrowski and C. F. Nathan, "Production of large amounts of hydrogen peroxide by human tumor cells," *Cancer Research*, vol. 51, no. 3, pp. 794–798, 1991. [Online]. Available: http://cancerres.aacrjournals.org/content/51/3/794

[138] U. E. Martinez-Outschoorn, Z. Lin, C. Trimmer, N. Flomenberg, C. Wang, S. Pavlides, R. G. Pestell, A. Howell, F. Sotgia, and M. P. Lisanti, "Cancer cells metabolically" fertilize" the tumor microenvironment with hydrogen peroxide, driving the warburg effect: implications for pet imaging of human tumors," *Cell cycle*, vol. 10, no. 15, pp. 2504–2520, 2011.

[139] D. Yan, H. Cui, W. Zhu, A. Talbot, L. G. Zhang, J. H. Sherman, and M. Keidar, "The strong cell-based hydrogen peroxide generation triggered by cold atmospheric plasma," *Scientific reports*, vol. 7, no. 1, p. 10831, 2017.

[140] B. L. Carlson, J. L. Pokorny, M. A. Schroeder, and J. N. Sarkaria, "Establishment, maintenance, and in vitro and in vivo applications of primary human glioblastoma multiforme (gbm) xenograft models for translational biology studies and drug discovery," *Current protocols in pharmacology*, pp. 14–16, 2011.

[141] L. Michaelis and M. L. Menten, "The kinetics of the inversion effect," *Biochem. Z*, vol. 49, pp. 333–369, 1913.

[142] K. A. Johnson and R. S. Goody, "The original michaelis constant: translation of the 1913 michaelis–menten paper," *Biochemistry*, vol. 50, no. 39, pp. 8264–8269, 2011.

[143] R. Dringen and B. Hamprecht, "Involvement of glutathione peroxidase and catalase in the disposal of exogenous hydrogen peroxide by cultured astroglial cells," *Brain research*, vol. 759, no. 1, pp. 67–75, 1997.

[144] R. Dringen, L. Kussmaul, and B. Hamprecht, "Detoxification of exogenous hydrogen peroxide and organic hydroperoxides by cultured astroglial cells assessed by microtiter plate assay," *Brain Research Protocols*, vol. 2, no. 3, pp. 223–228, 1998.

[145] R. Dringen, L. Kussmaul, J. M. Gutterer, J. Hirrlinger, and B. Hamprecht, "The glutathione system of peroxide detoxification is less efficient in neurons than in astroglial cells," *Journal of neurochemistry*, vol. 72, no. 6, pp. 2523–2530, 1999.

[146] J. R. Liddell, S. R. Robinson, and R. Dringen, "Endogenous glutathione and catalase protect cultured rat astrocytes from the iron-mediated toxicity of hydrogen peroxide," *Neuroscience letters*, vol. 364, no. 3, pp. 164–167, 2004.

[147] R. Dringen, "Metabolism and functions of glutathione in brain," *Progress in neurobiology*, vol. 62, no. 6, pp. 649–671, 2000.

[148] R. Dringen, J. M. Gutterer, and J. Hirrlinger, "Glutathione metabolism in brain," *The FEBS Journal*, vol. 267, no. 16, pp. 4912–4916, 2000.

[149] R. Dringen, M. Brandmann, M. C. Hohnholt, and E.-M. Blumrich, "Glutathione-dependent detoxification processes in astrocytes," *Neurochemical research*, vol. 40, no. 12, pp. 2570–2582, 2015.

[150] B. Grobben, P. De Deyn, and H. Slegers, "Rat c6 glioma as experimental model system for the study of glioblastoma growth and invasion," *Cell and Tissue Research*, vol. 310, no. 3, pp. 257–270, Dec 2002. [Online]. Available: https://doi.org/10.1007/s00441-002-0651-7

[151] S. Doblas, T. He, D. Saunders, J. Pearson, J. Hoyle, N. Smith, M. Lerner, and R. A. Towner, "Glioma morphology and tumor-induced vascular alterations revealed in seven rodent glioma models by in vivo magnetic resonance imaging and angiography," *Journal of Magnetic Resonance Imaging*, vol. 32, no. 2, pp. 267–275, 2010. [Online]. Available: https://onlinelibrary.wiley.com/doi/abs/10.1002/jmri.22263

[152] A. Gieryng, D. Pszczolkowska, K. Bocian, M. Dabrowski, W. D. Rajan, M. Kloss, J. Mieczkowski, and B. Kaminska, "Immune microenvironment of experimental rat c6 gliomas resembles human glioblastomas," *Scientific reports*, vol. 7, no. 1, p. 17556, 2017.

[153] I. Dokic, C. Hartmann, C. Herold-Mende, and A. Régnier-Vigouroux, "Glutathione peroxidase 1 activity dictates the sensitivity of glioblastoma cells to oxidative stress," *Glia*, vol. 60, no. 11, pp. 1785–1800, 2012. [Online]. Available: https://onlinelibrary.wiley.com/doi/abs/10.1002/glia.22397

[154] M. C. Sobotta, A. G. Barata, U. Schmidt, S. Mueller, G. Millonig, and T. P. Dick, "Exposing cells to h2o2: a quantitative comparison between continuous low-dose and one-time high-dose treatments," *Free Radical Biology and Medicine*, vol. 60, pp. 325–335, 2013.

[155] M. C. Regier, E. T. Alarid, and D. J. Beebe, "Progress towards understanding heterotypic interactions in multi-culture models of breast cancer," *Integrative Biology*, vol. 8, no. 6, pp. 684–692, 2016.

[156] L. Kim, Y.-C. Toh, J. Voldman, and H. Yu, "A practical guide to microfluidic perfusion culture of adherent mammalian cells," *Lab on a Chip*, vol. 7, no. 6, pp. 681–694, 2007.

[157] F. Meiners, I. Plettenberg, J. Witt, B. Vaske, A. Lesch, I. Brand, and G. Wittstock, "Local control of protein binding and cell adhesion by patterned organic thin films," *Analytical and bioanalytical chemistry*, vol. 405, no. 11, pp. 3673–3691, 2013.

[158] R. A. Gatenby and R. J. Gillies, "Why do cancers have high aerobic glycolysis?" *Nature reviews cancer*, vol. 4, no. 11, p. 891, 2004.

[159] N. Yamamoto, M. Ueda-Wakagi, T. Sato, K. Kawasaki, K. Sawada, K. Kawabata, M. Akagawa, and H. Ashida, "Measurement of glucose uptake in cultured cells," *Current protocols in pharmacology*, vol. 71, no. 1, pp. 12–14, 2015.

[160] R. J. DeBerardinis and N. S. Chandel, "Fundamentals of cancer metabolism," *Science advances*, vol. 2, no. 5, p. e1600200, 2016.

[161] A. M. Navale and A. N. Paranjape, "Glucose transporters: physiological and pathological roles," *Biophysical reviews*, vol. 8, no. 1, pp. 5–9, 2016.

[162] J. E. Foley, S. W. Cushman, and L. B. Salans, "Glucose transport in isolated rat adipocytes with measurements of l-arabinose uptake." *American Journal of Physiology-Endocrinology And Metabolism*, vol. 234, no. 2, p. E112, 1978.

[163] T. TeSlaa and M. A. Teitell, "Techniques to monitor glycolysis," in *Methods in enzymology*. Elsevier, 2014, vol. 542, pp. 91–114.

[164] R. A. Yotter and D. M. Wilson, "Sensor technologies for monitoring metabolic activity in single cells-part ii: nonoptical methods and applications," *IEEE Sensors Journal*, vol. 4, no. 4, pp. 412–429, 2004.

[165] J. Kieninger, A. Weltin, H. Flamm, and G. A. Urban, "Microsensor systems for cell metabolism–from 2d culture to organ-on-chip," *Lab on a Chip*, vol. 18, no. 9, pp. 1274–1291, 2018.

[166] J. Rothe, O. Frey, R. Madangopal, J. Rickus, and A. Hierlemann, "Robust functionalization of large microelectrode arrays by using pulsed potentiostatic deposition," *Sensors*, vol. 17, no. 1, p. 22, 2017.

[167] S. Talaei, P. D. van der Wal, S. Ahmed, M. Liley, and N. F. de Rooij, "Enzyme su-8 microreactors: simple tools for cell-culture monitoring," *Microfluidics and Nanofluidics*, vol. 19, no. 2, pp. 351–361, 2015.

[168] S. Telang, A. N. Lane, K. K. Nelson, S. Arumugam, and J. Chesney, "The oncoprotein h-ras v12 increases mitochondrial metabolism," *Molecular cancer*, vol. 6, no. 1, p. 77, 2007.

[169] Z. Xing, S. Wang, and E. J. Tran, "Characterization of the mammalian dead-box protein ddx5 reveals functional conservation with s. cerevisiae ortholog dbp2 in transcriptional control and glucose metabolism," *RNA*, vol. 23, no. 7, pp. 1125–1138, 2017.

[170] Z. Xing, S. Utturkar, M. Russon, and E. J. Tran, "The rna helicase ddx5 supports mitochondrial function in small cell lung cancer," *Manuscript under preparation.*

[171] S. A. Mookerjee, R. L. Goncalves, A. A. Gerencser, D. G. Nicholls, and M. D. Brand, "The contributions of respiration and glycolysis to extracellular acid production," *Biochimica Et Biophysica Acta (BBA)-Bioenergetics*, vol. 1847, no. 2, pp. 171–181, 2015.

[172] E. Bianconi, A. Piovesan, F. Facchin, A. Beraudi, R. Casadei, F. Frabetti, L. Vitale, M. C. Pelleri, S. Tassani, F. Piva *et al.*, "An estimation of the number of cells in the human body," *Annals of human biology*, vol. 40, no. 6, pp. 463–471, 2013.

[173] H. S. Carslaw and J. C. Jaeger, "Conduction of heat in solids," *Oxford: Clarendon Press, 1959, 2nd ed.*, 1959.

[174] J. Crank *et al.*, *The mathematics of diffusion.* Oxford university press, 1979.

[175] H. C. Berg, *Random walks in biology.* Princeton University Press, 1993.

[176] J. Pei, M.-L. Tercier-Waeber, J. Buffle, G. C. Fiaccabrino, and M. Koudelka-Hep, "Individually addressable gel-integrated voltammetric microelectrode array for high-resolution measurement of concentration profiles at interfaces," *Analytical chemistry*, vol. 73, no. 10, pp. 2273–2281, 2001.

[177] O. T. Guenat, S. Generelli, N. F. de Rooij, M. Koudelka-Hep, F. Berthiaume, and M. L. Yarmush, "Development of an array of ion-selective microelectrodes aimed for the monitoring of extracellular ionic activities," *Analytical Chemistry*, vol. 78, no. 21, pp. 7453–7460, 2006, pMID: 17073412.

[178] D. B. Sheth, "Multielectrode platform for measuring oxygenation status in multicellular tumor spheroids," Ph.D. dissertation, Case Western Reserve University, 2011.

[179] D. B. Sheth and M. Gratzl, "Electrochemical mapping of oxygenation in the three-dimensional multicellular tumour hemi-spheroid," *Proceedings of the Royal Society A: Mathematical, Physical and Engineering Sciences*, vol. 475, no. 2225, p. 20180647, 2019. [Online]. Available: https://royalsocietypublishing.org/doi/abs/10.1098/rspa.2018.0647

VITA

VITA

Received B.Sc. and M.Sc. degrees both in Electronics Engineering from Universidad del Valle, Cali, Colombia, and Ph.D. degree in Electrical and Computer Engineering from Purdue University, West Lafayette, IN, USA. His expertise includes the physics, design, fabrication, characterization, testing, optimization, and physiological application of electrochemical biosensors and devices to measure analyte concentration and mass transport.